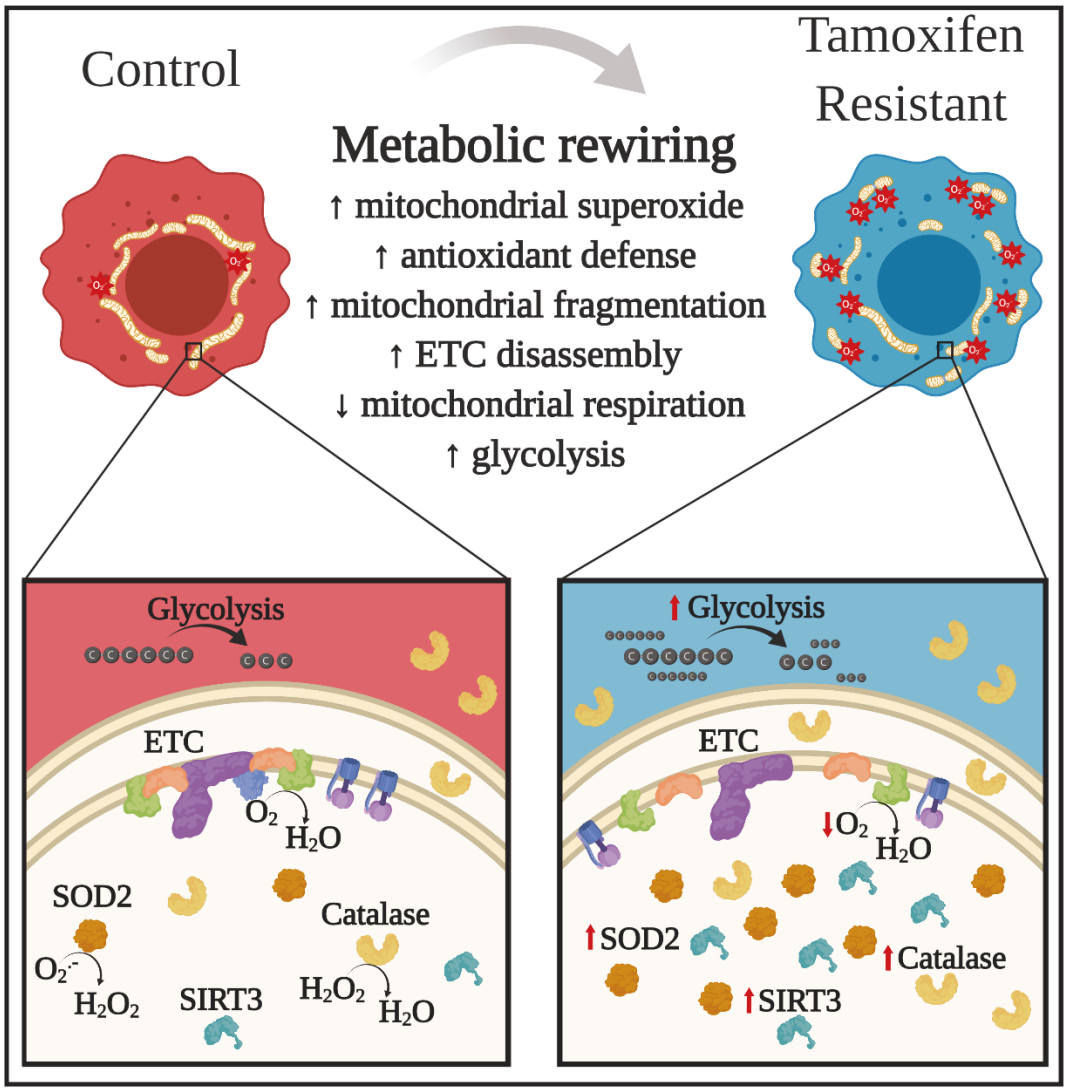
Control
Tamoxifen Resistant
Metabolic rewiring
↑ mitochondrial superoxide
↑ antioxidant defense
↑ mitochondrial fragmentation
↑ ETC disassembly
↓ mitochondrial respiration
↑ glycolysis
Glycolysis
ETC
O2
H2O
SOD2
Catalase
O2·-
H2O2
SIRT3
H2O2
H2O
↑ Glycolysis
ETC
↓O2
H2O
↑SOD2
↑Catalase
↑SIRT3

Free Radical Biology and Medicine 143 (2019) 510–521

Contents lists available at ScienceDirect

Free Radical Biology and Medicine

journal homepage: www.elsevier.com/locate/freeradbiomed

Original article

Mitochondrial fragmentation, elevated mitochondrial superoxide and respiratory supercomplexes disassembly is connected with the tamoxifen-resistant phenotype of breast cancer cells

Veronika Tomková, Cristian Sandoval-Acuña, Natalia Torrealba, Jaroslav Truksa*

Institute of Biotechnology, Czech Academy of Sciences, BIOCEV, Vestec, Czech Republic

ARTICLE INFO

Keywords:
Breast cancer
Tamoxifen resistance
Mitochondria
Mitochondrial fragmentation
Reactive oxygen species

ABSTRACT

Tamoxifen resistance remains a clinical obstacle in the treatment of hormone sensitive breast cancer. It has been reported that tamoxifen is able to target respiratory complex I within mitochondria. Therefore, we established two tamoxifen-resistant cell lines, MCF7 Tam5R and T47D Tam5R resistant to 5 μM tamoxifen and investigated whether tamoxifen-resistant cells exhibit mitochondrial changes which could help them survive the treatment. The function of mitochondria in this experimental model was evaluated in detail by studying i) the composition and activity of mitochondrial respiratory complexes; ii) respiration and glycolytic status; iii) mitochondrial distribution, dynamics and reactive oxygen species production. We show that Tam5R cells exhibit a significant decrease in mitochondrial respiration, low abundance of assembled mitochondrial respiratory supercomplexes, a more fragmented mitochondrial network connected with DRP1 Ser637 phosphorylation, higher glycolysis and sensitivity to 2-deoxyglucose. Tam5R cells also produce significantly higher levels of mitochondrial superoxide but at the same time increase their antioxidant defense (CAT, SOD2) through upregulation of SIRT3 and show phosphorylation of AMPK at Ser 485/491. Importantly, MCF7 ρ0 cells lacking functional mitochondria exhibit a markedly higher resistance to tamoxifen, supporting the role of mitochondria in tamoxifen resistance. We propose that reduced mitochondrial function and higher level of reactive oxygen species within mitochondria in concert with metabolic adaptations contribute to the phenotype of tamoxifen resistance.

1. Introduction

Breast cancer is the most frequent cancer in women worldwide. Estrogen receptor (ER) plays a pivotal role in the development and progression of this malignity. Approximately 60% of all breast cancer patients are diagnosed with ER^+ tumors, which have a better prognosis compared to triple negative breast cancer or human epidermal growth factor receptor 2^+ ($HER2^+$) tumors [1]. The canonical genomic estrogen receptor signaling pathway consists of the ER and its ligand, estradiol. Upon binding of the ligand, the receptor undergoes a conformational change and is translocated into the nucleus, where it acts as a transcription factor turning on specific estrogen response genes. Yet, estrogen receptor also mediates non-genomic signaling through its interaction with a variety of signaling proteins such as G-proteins, Src kinases, EGFR, HER2, Ras or PI3K. Such interactions result in the activation of protein-kinase cascades and phosphorylation of transcription factors, thus regulating gene expression [2].

Tamoxifen represents the most common drug used in the adjuvant treatment of hormone-sensitive breast cancer, belonging to the class of drugs termed selective estrogen receptor modulators. It acts as an antagonist in breast tissue, where it competitively binds to the ER, thus preventing its physiological function [3]. Although tamoxifen is a very effective drug that has been proven to decrease mortality, improve overall survival and reduce recurrence rates, resistance to tamoxifen remains a major clinical issue in the treatment of breast cancer. In spite of continuous development of different treatment approaches, 30–50% patients develop resistance to tamoxifen within 5–10 years of therapy [4,5]. A variety of molecular mechanisms have been proposed to be responsible for tamoxifen resistance, usually involving the substitution of the pro-proliferative ER signaling by alternative signaling pathways such as EGFR/HER2 or IGFR [6–8]. Additional evidence suggests the involvement of a structurally different isoform of ER (ERα36) which is elevated in tamoxifen-resistant cells [9]. On the other hand, breast tumors expressing low protein levels of another ER isoform (ERβ) have

* Corresponding author. Laboratory of Tumour Resistance, Institute of Biotechnology, Academy of Sciences of the Czech Republic, BIOCEV, Prumyslova 595, 25250, Vestec, Czech Republic.
E-mail address: jaroslav.truksa@ibt.cas.cz (J. Truksa).

https://doi.org/10.1016/j.freeradbiomed.2019.09.004
Received 17 June 2019; Received in revised form 4 September 2019; Accepted 4 September 2019
Available online 05 September 2019

Abbreviations

Tam5R	Tamoxifen-resistant
Ctrl	Control
2-DG	2-deoxyglucose
ROS	Reactive oxygen species
ER	Estrogen receptor
HER2	Human epidermal growth factor receptor 2
mtDNA	Mitochondrial DNA
ETC	Electron transport chain
AV/PI	Annexin V/Propidium iodide
BNE	Blue native electrophoresis
hr-CNE	High resolution Clear Native Electrophoresis
RIPA	Radioimmunoprecipitation assay buffer
OCR	Oxygen consumption rate
DCF	2′,7′-Dichlorofluorescein diacetate
2-NBDG	2-(N-(7-Nitrobenz-2-oxa-1,3-diazol-4-yl)Amino)-2-Deoxyglucose
RFU	Relative fluorescence units
SCs	Supercomplexes
DRP1	Dynamin related protein 1
SOD2	Superoxide dismutase 2
GPX1	Glutathione peroxidase 1
GLUT1	Glucose transporter 1
ACO2	Aconitase 2
HKII	Hexokinase 2
PFK2	Phosphofructokinase 2
PDK1	Pyruvate dehydrogenase kinase 1
AMPK	AMP-activated protein kinase
LKB1	Liver kinase B1
IDH2	Isocitrate dehydrogenase 2
ACS2	Acetyl-CoA synthetase 2

been suggested to be resistant to tamoxifen treatment [10]. Furthermore, some studies suggest deregulation of miRNA expression profile in tamoxifen-resistant cells. Indeed, several miRNAs show direct modulation of the ER pathway (miR18a, miR-18b, miR-22, miR-193b, miR-206, miR-221/222, miR-301a, miR-302c), linking them with the acquisition of resistance to tamoxifen treatment [11–14]. Additionally, data proposing involvement of p130Cas/Src signaling as well as NFκB pathway in the resistance has been published [15–17]. The mechanisms of tamoxifen resistance are thus multiple and overlapping. However, the studies mostly focus on a single pathway or protein. Therefore, the synthesis of knowledge and the net effect of tamoxifen on cellular metabolism and behavior still warrants further research.

Several groups have reported that tamoxifen is able to directly alter mitochondrial function. It preferentially accumulates in cellular membranes and its accumulation within mitochondria influences crucial processes such as respiration [18–20], fatty acid oxidation [18], mitochondrial DNA (mtDNA) synthesis and replication [18], and expression of mitochondrially encoded subunits of electron transport chain (ETC) [18]. Some of the complexes of ETC are weak but direct targets of tamoxifen, as has been described in case of CI [19], CIII [20] and CIV [20]. However, these reports describe either immediate effects of tamoxifen mostly on isolated liver mitochondria [19,20], or the effect on mitochondria after administration of tamoxifen to mice for 28 days [18]. Indeed, such results do not explore the consequences of long-term treatment and development of resistance on the cellular level, which could help answer the question whether resistant tumors undergo mitochondrial changes and if this helps them survive the therapy.

To our knowledge, there are only a few studies describing bioenergetics in tamoxifen resistant cells, reporting altered mitochondrial function and metabolic profile [21,22]. Yet, these studies provide contradictory data about the differences in respiration between parental and tamoxifen-resistant cells. The knowledge of the actual metabolic rewiring and mitochondrial involvement in the phenotype of tamoxifen-resistant cells is still limited and we thus focused in this study on the role of mitochondria in the tamoxifen resistance in breast cancer cells.

2. Materials and methods

2.1. Cell lines and cell culture

Human breast cancer cell lines MCF7 (ATCC® HTB-22™) and T47D (ATCC® HTB-133™) were purchased from ATCC (Manassas, VA, USA). Both cell lines were used within 3 months of their initial thawing and cultured as instructed by ATCC. Cells resistant to 5 μM tamoxifen (Tam5R) were obtained by continuous cultivation of parental MCF7 and T47D cells in the presence of increasing concentrations of tamoxifen up to 5 μM (T5648, Sigma-Aldrich) for at least 6 months. MCF7 ρ0 cells were prepared following the protocol described by Tan et al. [23] and cultured as parental cells with the addition of 1 mM pyruvate (P5280, Sigma-Aldrich) and 50 μg/mL uridine (U3003, Sigma-Aldrich).

2.2. Cellular viability

The evaluation of the effect of tamoxifen on cellular viability in Control (Ctrl) and Tam5R cells was performed by crystal violet staining (C6158, Sigma-Aldrich). Briefly, 1×10^4 cells were seeded in 96 well plates and let to attach overnight. Tamoxifen was added in increasing concentrations (1–25 μM) and cells were incubated for additional 48 h. Afterwards, cells were fixed with 4% paraformaldehyde (76240, Fluka), washed with PBS and stained overnight with crystal violet (0.05% in water). Finally, cells were washed with PBS and crystals solubilized with 1% SDS. Absorbance was recorded at 595 nm by using Tecan Infinity M200 microplate reader. IC_{50} values for each condition were calculated by interpolating in a dose-response curve and are expressed as mean ± SD.

2.3. Annexin V/Propidium iodide staining

The cell death induced by tamoxifen was assessed by using Annexin V/Propidium iodide (AV/PI) double staining. 1×10^5 cells per well were seeded in 12 well plates and let to attach overnight. Tamoxifen was added in increasing concentrations (5–15 μM) and cells were incubated for 48 h. After trypsinization, cells were stained with annexin V-FITC (ANXV-B-FT, Apronex Biotechnologies) and propidium iodide (81845, Sigma-Aldrich), according to the manufacturer's instructions. Fluorescence was detected by flow cytometry (LSRFortessa, BD Biosciences) at $488nm_{Ex}/530nm_{Em}$ for AV and $561nm_{Ex}/610nm_{Em}$ for PI. Results are expressed as percentage of dead cells (sum of AV^+/PI^-, AV^-/PI^+ and AV^+/PI^+ cells).

2.4. Mice experiments

Athymic nude mice Crl:NU(NCr)-Foxn1^{nu}(Charles River) were implanted with a slow-release estradiol pellet (SE-121, 60-day release of 12 μg per day; Innovative Research of America). After three days, mice were divided in two groups and injected subcutaneously with 2×10^6 MCF7 Control or MCF7 Tam5R cells, respectively. When tumors reached the volume of 30–50 mm^3, each group was further divided into two subgroups and treated intraperitoneally with either tamoxifen (30 mg/kg weight), or vehicle (2.5% DMSO in corn oil, 100 μl per dose) twice per week. Tumor volume was monitored by the USI instrument Vevo770 (VisualSonics). All mice experiments were approved by the

Czech Academy of Sciences and performed according to the Czech Republic Council guidelines for the Care and Use of Animals in Research and Teaching.

2.5. Mitochondrial isolation and solubilization

Mitochondria were isolated from MCF7 and T47D Control and Tam5R cells by differential centrifugation, and solubilized with digitonin (D141, Sigma-Aldrich), as described in Ref. [24].

2.6. Blue native and Clear Native Electrophoresis

Blue Native Electropohresis (BNE) was used to determine the levels of mitochondrial respiratory complexes and high resolution Clear Native Electrophoresis (hr-CNE) was used to assess the activity of mitochondrial respiratory complexes, as described in Ref. [24].

2.7. SDS-PAGE and western blot

SDS-PAGE and western blot used a well-established method [25]. Whole cell lysates were prepared by resuspending the collected cell pellet in radioimmunoprecipitation assay buffer (RIPA). The list of primary antibodies is available as Supplementary Table S1.

2.8. Oxygen consumption

Oxygen consumption rate (OCR) was measured by the Seahorse Extracellular Flux (XFe96) analyzer (Agilent Technologies) according to the manufacturer's indications. 1×10^4 cells were seeded into XFe-96 well cell culture plates pre-coated with Poly-L-lysine (P4707, Sigma-Aldrich). After 24 h, cells were washed with XF assay media and incubated with XF assay media supplemented with 10 mM glucose (G7021, Sigma-Aldrich), 1 mM pyruvate (P5280, Sigma-Aldrich) and 2 mM L-glutamine (P04–80500P, PAN-Biotech) for 1 h in non-CO_2 incubator. XFe-96 sensor cartridge was loaded as follows: Port A: 1 μM oligomycin (04876, Sigma-Aldrich), port B: 0.5 μM CCCP (C2759, Sigma-Aldrich) and port C: 1 μM rotenone (R8875, Sigma-Aldrich) and 1.8 μM antimycin A (A8674, Sigma-Aldrich) (all final concentrations). Port D was loaded with Hoechst 33342 (B2261, Sigma-Aldrich) (2μg/ml) in PBS. Data are normalized to total cell number obtained after counting live cells by using ImageXpress Micro XLS analysis system (Molecular Devices).

2.9. Mitochondrial to nuclear DNA ratio measurement

Total DNA was isolated using DNAzol® (DN 127, Molecular Research Center) according to the manufacturer's instructions. For qPCR, we used 5x HOT FIREPol® EvaGreen® qPCR Supermix (08-36-00020, Solis BioDyne) and followed the procedure described in Ref. [14]. 5 ng of total DNA were used as a template per reaction. Primer sequences designed for the analysis were: for mtDNA *MTRT1 forward: CACCCAAGAACAGGGTTTGT; MTRT1 reverse: TGGCCATGGGTATGTT GTTA*; for nuclear DNA: human gDNA ValidPrime™ assay was purchased from TATAA Biocenter.

2.10. Mitochondrial mass measurement

Total mitochondrial mass was measured by staining with TOM20 antibody (sc-17764, Santa Cruz Biotechnolgy). Briefly, 1×10^5 cells were seeded in 12 well plates and let to attach overnight. Afterwards, cells were fixed with 4% paraformaldehyde and subsequently washed with PBS. Then, cells were permeabilized with saponin (47036, Sigma-Aldrich), washed and incubated with TOM20 primary antibody for 1h room temperature. After washing with PBS, cells were incubated with Alexa Fluor™ 488 (A-11001, ThermoFisher Scientific) secondary antibody. The fluorescence was measured by flow cytometry at $488nm_{Ex}$/$530nm_{Em}$.

2.11. Mitochondrial superoxide and cellular reactive oxygen species production

Mitochondrial superoxide and cellular reactive oxygen species (ROS) production were determined by the fluorescent probes MitoSOX™ (M36008, ThermoFisher Scientific) and 2′,7′-dichlorofluorescein diacetate (DCF; 35845, Sigma-Aldrich), respectively. Briefly, 1×10^5 cells per well were seeded in 12 well plates and let to attach overnight. Afterwards, cells were incubated for 20 min with 2.5 μM MitoSOX or 5 μM DCF. Fluorescence was measured by flow cytometry at $488nm_{Ex}$/$585nm_{Em}$ for MitoSOX and $488nm_{Ex}$/$530nm_{Em}$ for DCF.

2.12. Cell cycle measurement

Cell cycle was analyzed by using Vybrant™ DyeCycle™ Violet Stain (R37172, ThermoFisher Scientific). Briefly, 1×10^5 cells were seeded in 60 mm Petri dishes and incubated for 48 h. Cells were collected by trypsinization and resuspended in culture medium with the probe (5 μM). Finally, cell suspension was filtered and fluorencence measured by flow cytometry at $405nm_{Ex}$/$437nm_{Em.}$

2.13. Confocal microscopy

For confocal imaging, cells were seeded in 35 mm dishes with 20 mm glass bottom (D35-20-1-N; Cellvis) and let attach overnight. Afterwards, cells were incubated for 20 min with 20 nM MitoTracker™ Deep Red FM (M22426, ThermoFisher Scientific) and immediately before imaging with 2 μg/ml Hoechst 33342. Confocal microscopy images were aquired using a 63x water immersion lens in a Leica SP8 confocal microscopy (Leica Microsystems, Wetzlar, Germany) equipped with a heated humidified CO_2 incubator. Fluorescence was detected at $405nm_{Ex}$/$450nm_{Em}$ for Hoechst and $644nm_{Ex}$/$665nm_{Em}$ for MitoTracker. Radial analysis was performed using the ImageJ software (National Institute of Health) as previously described in Ref. [26].

2.14. ATP measurement

Total cellular ATP was measured using the CellTiter-Glo® Luminescent Cell Viability Assay kit (G7571, Promega) as instructed by the manufacturer. 1×10^4 cells were seeded the day before the experiment and the next day incubated in the absence or presence of 25 or 50 mM 2-deoxyglucose (2-DG, 14325, Cayman Chemicals) for 4 h prior to the measurement. ATP values were normalized to total protein content measured by BCA method (23252, ThermoFisher Scientific).

2.15. Lactate production

Extracellular lactate was measured using the Lactate Kit (735–10, Trinity Biotech). In brief, 1×10^4 cells per well were seeded in 96 well plate and allowed to attach. The next day, 1 μl of culture media together with Lactate Standard was pipetted in triplicate in a new 96 well plate and the Lactate Reagent was added (100 μl) and incubated for 10 min. Absorbance at 540 nm was measured in Tecan M200 infinity multiplate reader. Lactate values were normalized to total protein content, as measured by BCA method.

2.16. Glucose uptake

Glucose uptake was measured by using 2-NBDG (2-(N-(7-Nitrobenz-2-oxa-1,3-diazol-4-yl)Amino)-2-Deoxyglucose) (N13195, ThermoFisher Scientific). In brief, 1×10^5 cells per well were seeded in 12 well plates and let attach overnight. Afterwards, medium in wells was replaced by glucose-free medium and incubated for another 24 h. Then, 2-NBDG probe was added into each well (50 μM) and incubated for 20 min.

Fluorescence was measured by flow cytometry at $488nm_{Ex}/530nm_{Em}$.

2.17. Aconitase in gel activity

The activity of aconitase was assessed in gel as described in Ref. [27]. Proper loading was assessed by SDS-PAGE followed by Western Blot and immunodetection against β-actin.

2.18. Statistics

All results are expressed as mean ± SD of at least three independent experiments. The comparison between experimental groups and Control was performed by one- or two-way ANOVA with Bonferroni post-test, or by t-student test, using the GraphPad Prism 6.0 software. $p < 0.05$ was established as the minimum significance level.

3. Results and discussion

3.1. Establishing the MCF7 Tam5R and T47D Tam5R cell lines

We have set up a model of MCF7 and T47D tamoxifen-resistant cells by cultivating them in the presence of increasing concentrations of tamoxifen for over 6 months, resulting in their adaptation and ability to grow under 5 μM tamoxifen in the medium. Control MCF7 and T47D cells are not able to proliferate under such conditions, and eventually die. The 5 μM concentration was selected since at this concentration we can clearly see a differential response to tamoxifen between the Control and tamoxifen-resistant cells. Although the serum tamoxifen concentration from human patients is reported to lie around 80–200 ng/ml [28], the individual concentration can reach up to 527 ng/ml [29] which is within the low μM range. Some reports even suggest serum concentrations as high as 8 μM [30]. In addition, 5 μM concentration of tamoxifen or higher was also used in other published reports on tamoxifen resistance [31–33]. It is important to note that Tam5R cells express markers of cancer stem-like cells and epithelial to mesenchymal transition markers as documented in our previous work [25]. These

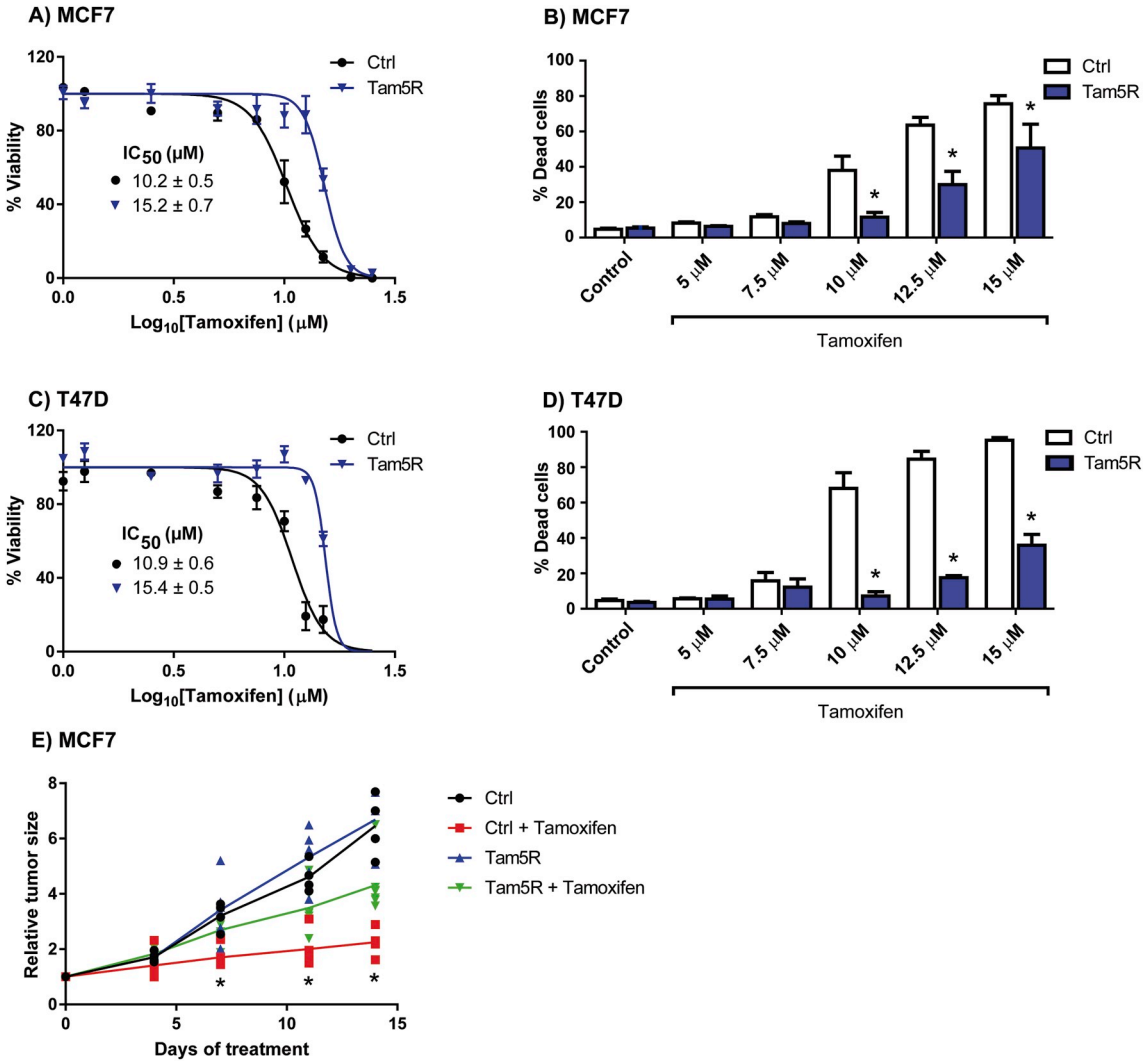

Fig. 1. Evaluation of the experimental model of Tam5R cells. Dose-response curves for the viability of **(A)** MCF7 and **(C)** T47D cells after incubation with increasing concentrations of tamoxifen for 48 h. IC_{50} values for each cell line are shown inside the graphs. Results are expressed as mean viability ± SD of at least 3 independent experiments. Cytotoxic effect of tamoxifen on **(B)** MCF7 and **(D)** T47D cells after 48 h incubation, measured by Annexin V/PI double staining. Results are expressed as mean % dead cells ± SD of at least 3 independent experiments. *$p \leq 0.05$ relative to Ctrl cells. **(E)** Tumor growth curves in mice injected with either MCF7 Ctrl or Tam5R cells. When tumors reached ~30 mm^3, mice were treated i.p. with tamoxifen (30 mg/kg weight) or vehicle 2 times per week for 14 days. The tumor sizes are expressed relative to day 0 (corresponding to the first day of treatment). Each group consisted of at least 5 animals. *$p \leq 0.05$ relative to Ctrl.

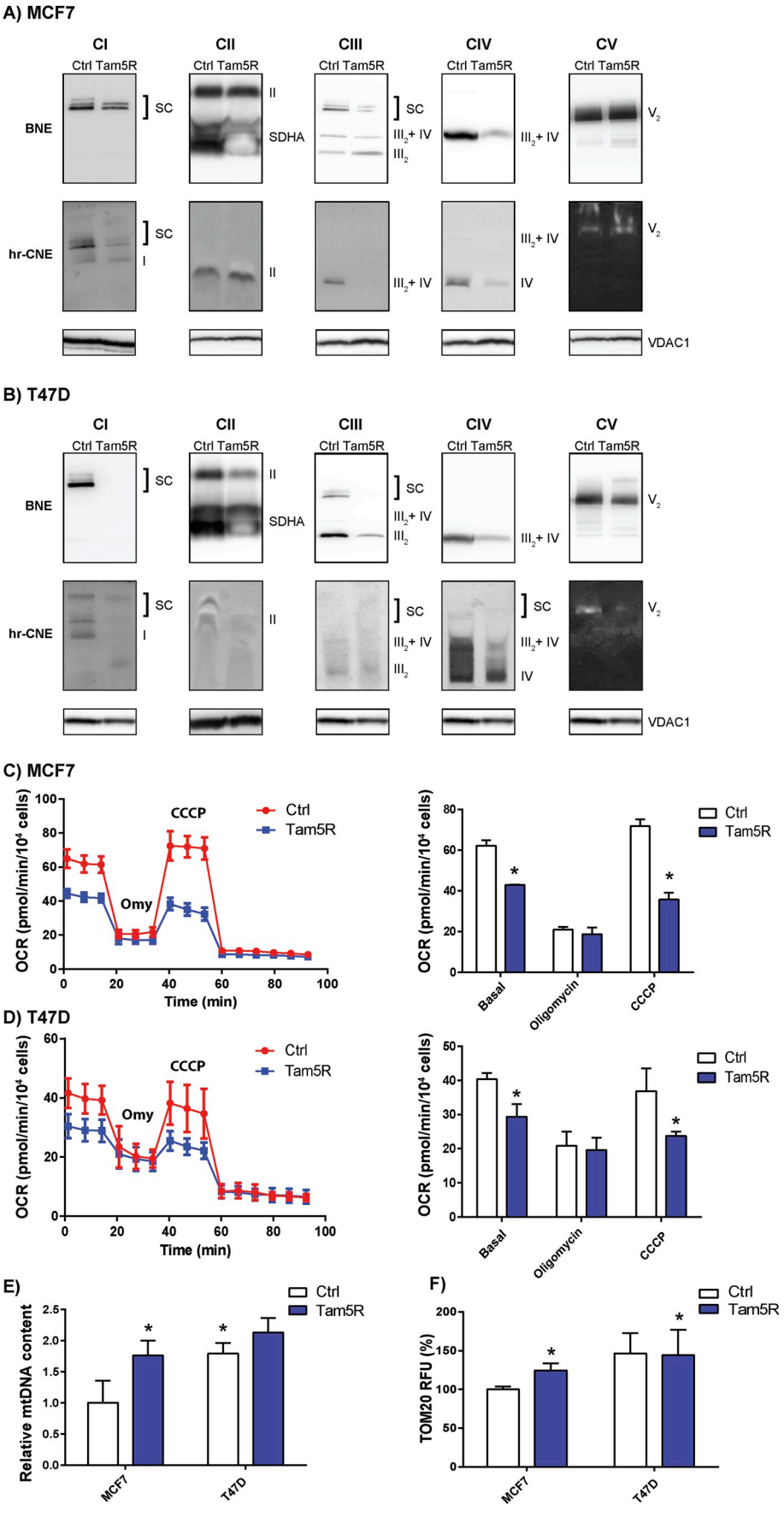

Fig. 2. Tam5R cells show mitochondrial dysfunction. BNE (upper) and hr-CNE (lower) of **(A)** MCF7 and **(B)** T47D cells showing the amount, assembly and activity of mitochondrial respiratory supercomplexes. Experiments were performed at least three times from independent samples. Oxygen consumption rate of **(C)** MCF7 and **(D)** T47D cells analyzed by Seahorse XFe96 flux analyzer (left). Average rates of basal, oligomycin inhibited and CCCP induced respiration are shown as mean ± SD of at least three independent experiments (right). *$p \leq 0.05$ relative to Ctrl cells. **(E)** Relative mitochondrial DNA content measured by qPCR. **(F)** Mitochondrial mass measured by TOM20 immunostaining by flow cytometry. **(E–F)** Data are shown relative to MCF7 Ctrl cells and correspond to the mean ± SD of at least three independent experiments. *$p \leq 0.05$ relative to MCF7 Ctrl cells.

finding suggest an enrichment of Tam5R cell line with cells exhibiting stem-like properties, higher resistance to apoptotic stimuli and pro-metastatic features.

3.2. Characterization of the resistant phenotype in MCF7 Tam5R and T47D Tam5R cell lines

In order to confirm the resistance of MCF7 and T47D derived Tam5R cell lines, we performed two independent assays. First, crystal violet staining was used to compare differences in cell viability between parental and Tam5R cell lines in the presence of increasing concentrations of tamoxifen (1–25 μM). The difference became evident at 10 μM concentration, and in 12.5 μM concentration MCF7 Control cells showed 26% viability, while Tam5R cells had around 88% viability (Fig. 1A). An even more pronounced difference was detected in T47D cells, with 20% viability for Control and 93% for Tam5R cells at 12.5 μM tamoxifen (Fig. 1C). This result is also documented by IC_{50} values listed inside the graphs in Fig. 1A and C, where values for both parental cell lines were very similar (around 10 μM) while in case of Tam5R cell lines IC_{50} values were increased to approximately 15 μM. The crystal violet staining measures both the cytostatic and the cytotoxic effect at once. Thus it is not able to distinguish whether a lower number of viable cells is due to inhibition of proliferation or cell death. To eliminate the possibility that the observed differences in viability could be due to different proliferation rates of Control and Tam5R cell lines, we measured the percentage of dead cells after tamoxifen treatment by AV/PI double staining using flow cytometry (Fig. 1B and D). We observed the same trend as in case of crystal violet staining, with a significant difference detected at 10 μM tamoxifen concentration in MCF7 cells, where the percentage of dead cells was 38% for Control MCF7 cells and 12% for Tam5R cells. Once again, the effect was even more profound in T47D cells where we detected 68% dead cells in Control vs. 7% in Tam5R cell line at 10 μM tamoxifen. A similar trend was observed in 12.5 μM and 15 μM tamoxifen in both cell lines. Finally, in order to confirm our experimental model of Tam5R cells *in vivo*, we injected MCF7 Control and Tam5R cells into athymic nude mice. As shown in Fig. 1E, both cell lines were able to form tumors *in vivo*. We did not detect any significant difference in tumor growth between non-treated animals. However, a significant difference was measured upon their treatment with tamoxifen. Indeed, tamoxifen-treated mice injected with the Control cell line show a significantly reduced tumor growth while animals injected with Tam5R cells exhibit only a slight decrease in the tumor growth after 14 days of treatment. These results confirmed our experimental model of tamoxifen-resistant cell lines cultivated in the long-term presence of tamoxifen *in vitro* as well as *in vivo*.

3.3. Analysis of mitochondrial supercomplexes revealed a profound decrease in their abundance, assembly and activity in Tam5R cells

Based on the known acute effects of tamoxifen on mitochondrial respiratory complexes [19,20], we decided to compare the abundance and composition of the respiratory supercomplexes (SCs) between parental and Tam5R cell lines. In case of both Tam5R cell lines we detected significant decrease in CI, CIII and CIV- containing SCs (Fig. 2A and B), which are known to form the respirasome, a supramolecular entity that has been proposed to enhance electron transfer and reduce reactive oxygen species (ROS) production [34]. The most dramatic effect was detected in CI in T47D Tam5R cells where we observed an almost total absence of SCs. The same effect as for CI, although with less intensity, was observed for CIII and CIV in both resistant cells lines. Moreover, in T47D Tam5R cell lines there was also a decrease in free CIII and CIII/CIV complex, as well as in CII. No significant difference of CII was detected in parental MCF7 cell line compared to MCF7 Tam5R. Similarly, no difference in CV abundance was found between MCF7 or T47D parental and resistant cells. In order to answer the question whether the observed dramatic decrease in the amount and assembly of SCs is also reflected in the activity of mitochondrial respiratory complexes, we assessed the enzymatic activity of the individual complexes. Similarly to BNE data, we detected lower activity of all complexes in case of T47D Tam5R cells (Fig. 2B). In the case of MCF7 Tam5R cells, activities of the complexes again corresponded to the BNE results where only CI, CIII and CIV were affected with apparently lower levels of enzymatically active free respiratory complexes as well as their disrupted assembly into SCs (Fig. 2A).

Although free CI was not detected in any of the cell lines and was found mostly associated in SCs using BNE, it is important to mention that the antibody used detects only a single subunit of CI (in our case NDUFA9). Therefore, lack of detection of free CI could be assigned to the fact that this particular subunit under these conditions may not be bound to the otherwise assembled CI and thus not label it. On the other hand, protein complexes migrate under different conditions in hr-CNE, without a Coomassie dye, thus the migration patterns in BNE and hr-CNE cannot be directly compared. Indeed, our results on in-gel activity do show a detectable band corresponding to free CI as well as CI SCs, both of which have a measurable enzymatic activity in control cells. Therefore, the loss of enzymatic activity of CI is very likely not just a matter of disassembly of CI-containing SCs, but also reflects a decrease in total CI. These results clearly show altered composition, and dramatic disassembly and dysfunction of mitochondrial SCs in Tam5R cells. Disassembly of respiratory SCs is usually linked to mitochondria that do not utilize respiration for energy production, are fragmented, and produce more ROS [35–37]. We thus analyzed the functional aspects of mitochondria, in order to gain further insight into the differences between Control and Tam5R cells.

3.4. Tam5R cells show decreased oxygen consumption

The main feature of the functional respiratory complexes is the ability to transfer electrons in a series of redox reactions to the final acceptor – oxygen, which is then reduced into water. This process is coupled with the pumping of protons into the intermembrane space, generating the gradient necessary for ATP production through complex V [38]. We therefore assessed the oxygen consumption rate (OCR) in MCF7 and T47D parental and Tam5R cells. We observed a significant reduction in the basal and maximal respiration of both Tam5R cell lines (Fig. 2C and D). Contradictory data have been published by Fiorillo et al. [22], where they show an increase in both basal and maximal respiration in tamoxifen-resistant cells. However, this result is supported only by Seahorse data and the study did not bring any further mechanistic insight except for an increased mitochondrial mass, which is strictly dependent on the presence of tamoxifen in the media. Another paper by Radde et al. [21] reports no changes in the basal respiration but a decreased maximal respiratory capacity in tamoxifen-resistant LCC2 cells, which is partially in agreement with our data. However, it is important to point that the experimental model of tamoxifen-resistant cells as well as the cultivation conditions described in these two publications are different from ours. Indeed, we used long-term cultivation in 10% fetal bovine serum (not charcoal stripped serum) in the presence of 5 μM tamoxifen in the media which, in our opinion, better reflects the situation in patients who carry estrogens in the systemic circulation and are treated with tamoxifen for years or even decades. Since our data clearly show that the activity, amount and assembly of mitochondrial SCs is dramatically lower in Tam5R cells, we expected a strong reduction in oxygen consumption in these cells. Yet, although we see a significant reduction, it is much less profound. This indicates that Tam5R cells are able to respire through individual complexes.

Together, our findings suggest that a decrease in the assembly and activity of mitochondrial SCs is coupled with decreased respiration in Tam5R cells. Therefore, we propose that mitochondria in Tam5R cells are, at least in terms of respiration, less effective in electron transfer and may show signs of functional damage.

3.5. Tam5R cells have increased mitochondrial mass

To elucidate if decreased respiration may be compensated by increased amount of mitochondria, we assessed the total mitochondrial mass of Control and resistant cells by analyzing the ratio between nuclear and mitochondrial DNA. As presented in Fig. 2E, MCF7 Tam5R cells show almost 1.8-fold higher mitochondrial/nuclear DNA ratio compared to their parental counterparts. On the other hand, T47D cells did not show any difference between Control and Tam5R cells (Fig. 2E). A similar result was obtained by staining cells with an antibody against the mitochondrial marker TOM20 (Fig. 2F). Yet, while MCF7 Tam5R cells showed almost 25% increase in fluorescence, T47D Tam5R were not different from parental ones. Of note, T47D parental cells exhibit higher amount of mtDNA as well as TOM20 levels compared to MCF7 parental cells. These data thus demonstrate that MCF7 cells do increase their amount of mitochondria and mtDNA. However, T47D cells do not increase their mass further, probably because they have already reached the achievable maximum.

3.6. Tam5R cells show increased mitochondrial fragmentation and superoxide levels

Besides the amount of mitochondrial mass, mitochondrial function is also substantially regulated by fusion and fission processes, which help shape the mitochondrial network, and thus influence cellular metabolism [39]. Therefore, we compared the structure of the mitochondrial network between parental and Tam5R cell lines by confocal microscopy. An initial analysis revealed that MCF7 Tam5R cells exhibit a significant increase in the radial distribution of mitochondria and a corresponding decrease in perinuclear and medial localization (Fig. 3A). Similarly, T47D Tam5R cells are characterized by a decrease in perinuclear localization accompanied by an increase in medial and a

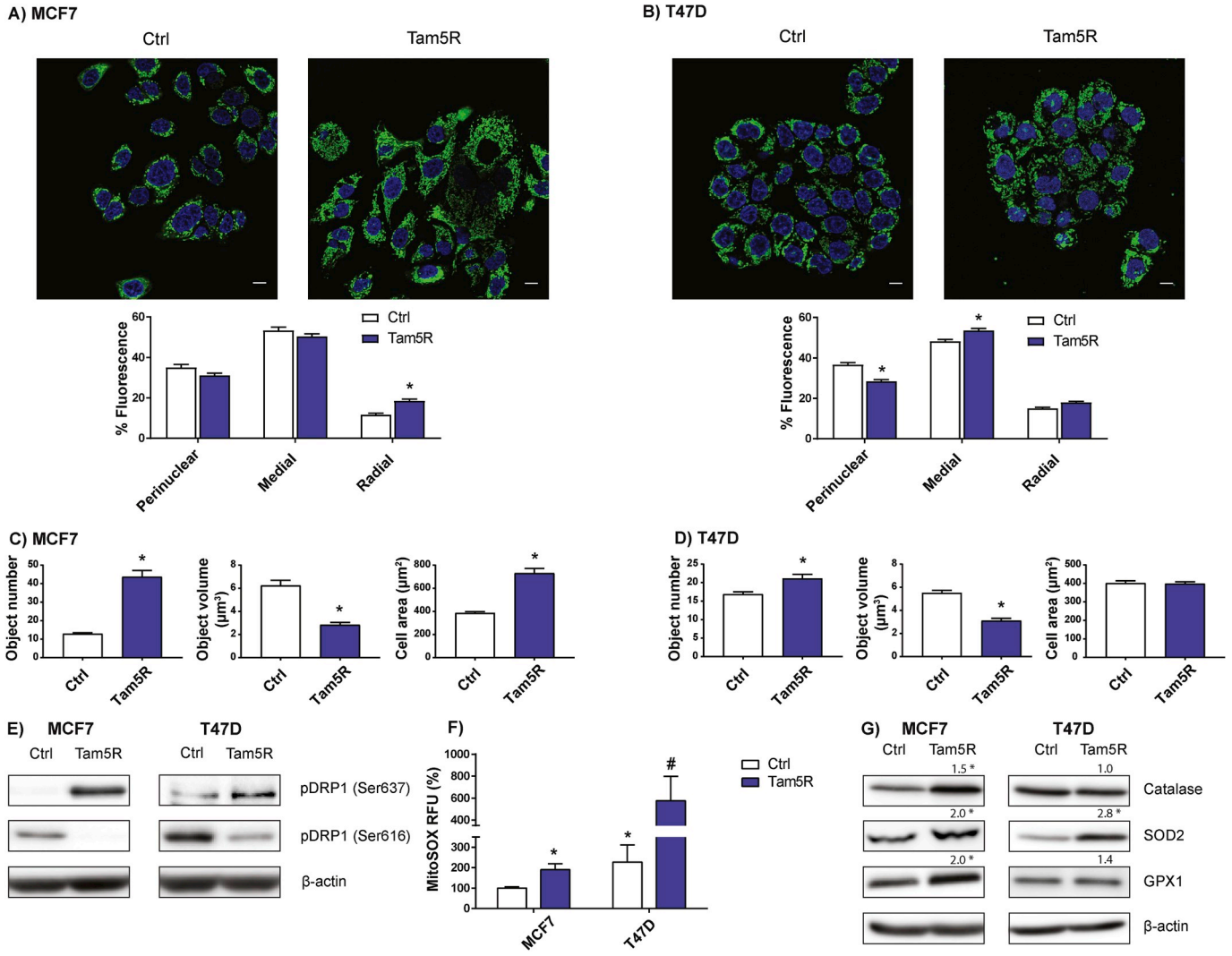

Fig. 3. Tam5R cells show fragmented mitochondria, increased mitochondrial superoxide and protein levels of antioxidant enzymes. Representative confocal images of **(A)** MCF7 and **(B)** T47D cells stained with MitoTracker Deep Red™ (green) and Hoechst (blue). Bar = 10 µm. The quantification of total fluorescence intensity in the perinuclear, medial and radial part of each cell is shown in graphs below. *$p \leq 0.05$ relative to Ctrl cells. Analysis of mitochondrial number and average size, and cell area, of **(C)** MCF7 and **(D)** T47D cells. *$p \leq 0.05$ relative to Ctrl cells. **(A–D)** Analysis was performed by the ImageJ software. Data are presented as mean values ± SD of at least three independent experiments, analyzing at least 50 cells from 5 images each. **(E)** Phosphorylation status of DRP1 in MCF7 and T47D cells evaluated by western blotting. The experiment was performed at least 3 times using independent samples. **(F)** Quantification of mitochondrial superoxide levels in MCF7 and T47D cells using the fluorescent probe MitoSOX™ by flow cytometry. Results are expressed as % of MitoSOX RFU normalized to MCF7 Ctrl cells and represent the mean ± SD of at least 3 independent experiments. *$p \leq 0.05$ relative to MCF7 Ctrl cells. #$p \leq 0.05$ relative to T47D Ctrl cells. **(G)** Protein levels of antioxidant enzymes Catalase, SOD2 and GPX1 in MCF7 and T47D cells evaluated by western blot. Band intensities were quantified using the ImageJ software from at least 3 independent samples, using β-actin for normalization. Numbers above each band represent the mean value relative to Ctrl cells. *$p \leq 0.05$ relative to Ctrl cells. (For interpretation of the references to colour in this figure legend, the reader is referred to the Web version of this article.)

slight increase in radial localization of mitochondria (Fig. 3B). Moreover, analysis of the images showed that MCF7 Tam5R cells have an increased number of individual mitochondria (3.4-fold over Control cells), yet a significantly decreased average organelle size (2.2-fold lower) (Fig. 3C). T47D Tam5R cells showed a similar, although less pronounced phenotype, with a 1.3-fold increase in mitochondrial number and a 1.8-fold decrease in mitochondrial size (Fig. 3D). This results show that Tam5R have a more fragmented mitochondrial

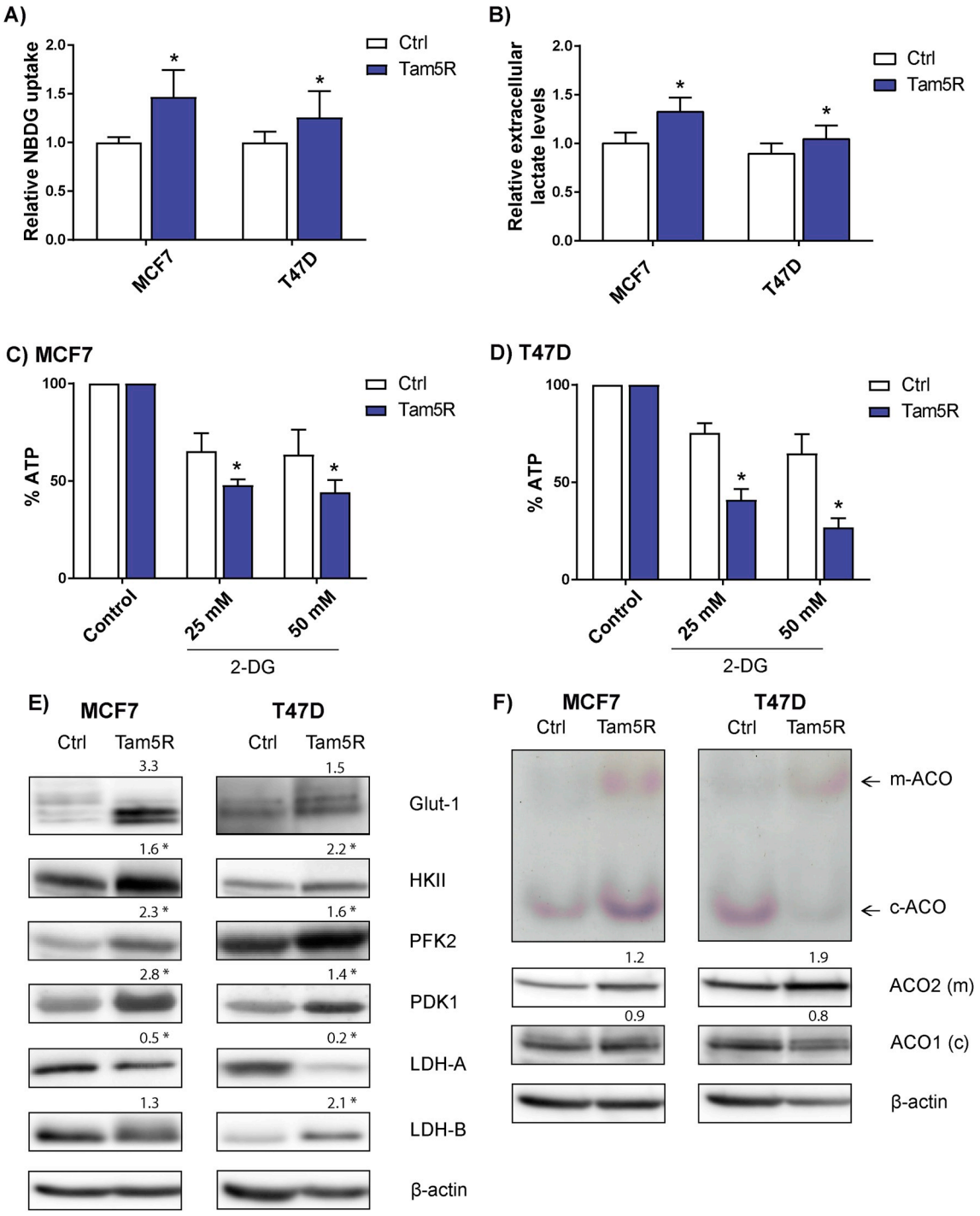

Fig. 4. Tam5R cells show increased glycolytic dependence. (A) Glucose uptake of MCF7 and T47D cells measured as the incorporation of the fluorescent probe NBDG by flow cytometry. **(B)** Extracellular lactate levels on MCF7 and T47D cells. **(A–B)** Data are shown as relative values compared to MCF7 Ctrl cells and represent the mean ± SD of at least 3 independent experiments. *$p \leq 0.05$ relative to corresponding Ctrl cells. Relative ATP values of **(C)** MCF7 and **(D)** T47D cells in the absence or presence of 2-DG (25 or 50 mM). Data are shown as % ATP level relative to each corresponding control condition and represent the mean ± SD of at least 3 independent experiments. *$p \leq 0.05$ relative to Ctrl cells with similar treatment. **(E)** Levels of the glucose transporter GLUT-1 and the glycolytic enzymes HKII, PFK2, PDK1, LDH-A and LDH-B in MCF7 and T47D cells evaluated by western blot. Band intensities were quantified using the ImageJ software on images from at least 3 independent samples, using β-actin for normalization. Numbers above each band represent the mean value relative to Ctrl cells. *$p \leq 0.05$ relative to Ctrl cells. **(F)** Activity of mitochondrial and cytosolic aconitase in MCF7 and T47D cells, assessed by in-gel activity assay (upper). Protein levels of mitochondrial and cytosolic aconitase in MCF7 and T47D cells evaluated by western blot (lower). Band intensities were quantified using the ImageJ software from at least 3 independent samples, using β-actin for normalization. Numbers above each band represent the mean value relative to Ctrl cells.

network and altered cellular distribution of these organelles.

One of the main regulators of mitochondrial fission is the dynamin related protein 1 (DRP1) whose activity is crucial for correct mitochondrial fragmentation. It has been shown that DRP1 is controlled by two main phosphorylation sites, an activating one at serine 637 and an inhibiting one at serine 616 [40,41]. When analyzing the phosphorylation status of DRP1 in Tam5R cells we found that the phosphorylation in Ser637 was significantly enhanced, and the one at Ser616 was almost completely absent, indicating an increase in the fission-inducing activity of DRP1 (Fig. 3E). Small fragmented mitochondria have been reported to be less functional and to produce higher levels of ROS [42], both of which have been connected with cancer stem-like cells and a more malignant phenotype [43–46]. These observations then fit well with our previous study suggesting that Tam5R cells show enrichment of the cancer stem-like cells [25]. Therefore, we next analyzed the mitochondrial superoxide levels and antioxidant response in Control and Tam5R cells. Consistent with our previous results, we observed a significant increase in the levels of mitochondrial superoxide in both MCF7 Tam5R (1.9-fold) and T47D Tam5R (2.5-fold) cells (Fig. 3F). In line with this evidence, both resistant cell lines show increased expression of mitochondrial antioxidant enzymes superoxide dismutase 2 (SOD2) and glutathione peroxidase 1 (GPX1). MCF7 Tam5R cells also exhibit increased expression of the ubiquitous antioxidant enzyme catalase (Fig. 3G). Although the increase in catalase protein level is not evident in T47D Tam5R cells, it might reflect their higher basal expression of the enzyme (Fig. 3G), which is also consistent with their much higher basal level of mitochondrial superoxide (Fig. 3F) and total cellular ROS (Fig. S1A). Of note, the mitochondrial superoxide production is not a direct effect of tamoxifen presence as Tam5R cells exhibit elevated levels even when cultivated without tamoxifen for several weeks (Fig. S1B). Importantly, high mitochondrial ROS have been shown to drive sustained mitogenic signaling, oncogenic transformation and genomic instability [47], supporting the important role of mitochondrial superoxide in the examined phenotype.

Together, our data show that mitochondrial network of Tam5R cells is fragmented and mitochondria are moving to the periphery of the cell. Furthermore, we detected a clear activatory phosphorylation pattern of the DRP1 protein, coherent with increased fragmentation of mitochondria. Similarly, in agreement with the prevailing view that fragmented mitochondria produce more ROS, we found a clear upregulation of mitochondrial superoxide production. This latter result might also explain the observed dramatic decrease in the amount of assembled SCs, as these supramolecular entities are extremely sensitive to ROS [34].

3.7. Tam5R cells show increased glycolysis, LDH-A_{low}/LDH-B_{high} phenotype and activation of mitochondrial aconitase

Besides oxidative phosphorylation, cells also use glycolysis for ATP production and as a source of metabolism intermediates. Indeed, metabolic switches often allow cells to rely mainly on glycolysis upon mitochondrial inhibition or dysfunction [48]. Based on our previous results that showed a significant decrease in mitochondrial respiratory SCs and oxygen consumption, we tested the activity and involvement of glycolysis in Control and Tam5R cells. Our results demonstrate that both Tam5R cell lines exhibit higher glucose uptake (47% in MCF7 and 26% in T47D Tam5R cells) (Fig. 4A) and extracellular lactate production (32% in MCF7 and 17% in T47D Tam5R) (Fig. 4B). In order to quantify the contribution of glycolysis to the total ATP level, Control and Tam5R cells were treated with the glycolysis inhibitor 2-deoxyglucose (2-DG; 25 or 50 mM), and the ATP level was measured. The results show that in case of MCF7 Control cells there is a drop in ATP production of about 35% while in MCF7 Tam5R ATP levels are decreased by 52% in the presence of 25 mM 2-DG (Fig. 4C). The same is observed in T47D cells where we detected a 25% drop in ATP production in Control cells compared to a 59% drop in Tam5R cells in 25 mM 2-DG (Fig. 4D). These findings demonstrate that both Tam5R cell lines are more sensitive to the short term effect of 2-DG than their parental counterparts, evidencing that these cells rely more on glycolysis for ATP production than on oxidative phosphorylation. Consistently, both resistant cell lines exhibit an increased expression of the

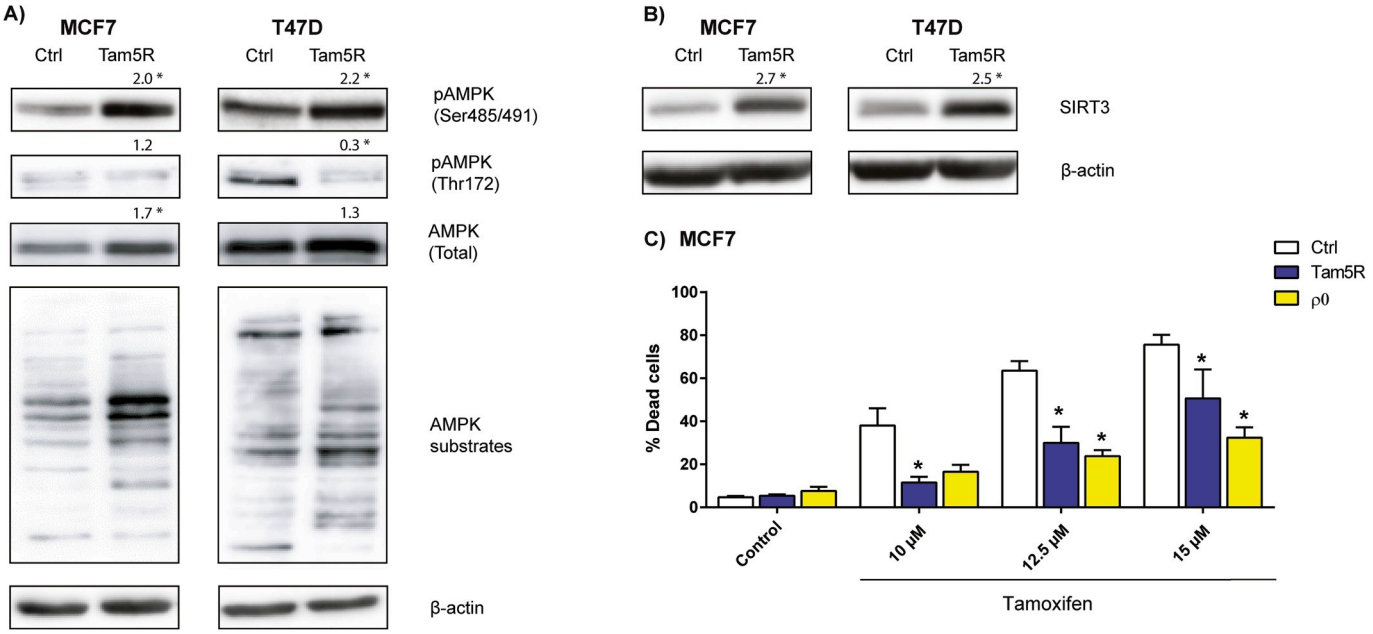

Fig. 5. Altered metabolic regulation in Tam5R cells. (A) The phosphorylation of AMPK at Ser 485/491 and Thr 172, total AMPK levels and pattern of AMPK substrates phosphorylation in MCF7 and T47D cells evaluated by western blot. **(B)** Protein level of the mitochondrial regulator SIRT3 in MCF7 and T47D cells evaluated by western blot. **(A–B)** Band intensities were quantified using the ImageJ software on images from at least 3 independent samples, using β-actin for normalization. Numbers above each band represent the mean value relative to Ctrl cells. *$p \leq 0.05$ relative to Ctrl cells. **(C)** Cytotoxic effect of tamoxifen on MCF7 Control, Tam5R and ρ0 cells after 48 h incubation, as measured by Annexin V/PI double staining. Results are expressed as mean % dead cells ± SD of at least 3 independent experiments. *$p \leq 0.05$ relative to Ctrl cells.

ubiquitous glucose transporter 1 (GLUT1), as well as some of the key glycolytic enzymes, such as hexokinase II (HKII), phosphofructokinase 2 (PFK2) and pyruvate dehydrogenase kinase 1 (PDK1) (Fig. 4E). Interestingly, the ratio of LDH-A/LDH-B, which is an indicator of the direction of the pyruvate/lactate reaction, was significantly lower in both Tam5R cell lines when compared to the parental cell lines (Fig. 4E). Given that LDH-B is the isoform which favors the reverse reaction (lactate to pyruvate), such result suggests a metabolic rewiring that allows pyruvate utilization for other metabolic processes. In fact, pyruvate can be converted to oxaloacetate, which has been shown to increase mitochondrial biogenesis and ameliorate ROS-induced damage [49]. Furthermore, since we detected higher activity of mitochondrial aconitase 2 (ACO2) (Fig. 4F), which converts citrate to isocitrate, we can speculate that Tam5R cells utilize a pyruvate/isocitrate cycle leading to production of NADPH and α-ketoglutarate [50–52]. NADPH could be then utilized for further anabolic reactions while α-ketoglutarate can be converted into glutamine and serve as an antioxidant that inhibits mitochondrial oxygen consumption [53,54]. Taken together, these findings suggest that MCF7 and T47D Tam5R cells compensate their reduced mitochondrial respiration by switching to a predominantly glycolytic metabolism. Importantly, Tam5R cells show a LDH-A_{low}/LDH-B_{high} phenotype, indicating that they use glycolysis to produce ATP, yet, they do not switch all pyruvate to lactate and use pyruvate for other anabolic reactions. Furthermore, the analysis of cell cycle showed a significant accumulation of Tam5R cells in G1 cell phase and a marked reduction in the S phase compared to Control cells, suggesting that the completing of the cell cycle is much slower in Tam5R cells, in agreement with their lower metabolic activity (Fig. S1C).

3.8. Tam5R cells show increased phosphorylation of AMPK at Ser485/491 as well as increased levels of SIRT3

In order to further understand the differences between Control and Tam5R cells, we looked into the molecular mechanisms that may underlie the observed metabolic changes. The AMP-activated protein kinase (AMPK) represents one of the main metabolic sensors, and its activation by many signaling pathways is critical for metabolic reprogramming in response to metabolic stress [55]. Our results show an increased AMPK phosphorylation at Ser485/491 in Tam5R cells (Fig. 5A). In addition, T47D Tam5R show a decreased phosphorylation in Thr172 (Fig. 5A). Although such changes in phosphorylation have been reported to inhibit the activity of AMPK [56,57], we detected differences in the phosphorylation pattern of the AMPK substrates, showing mostly an increase in phosphorylation of the most abundant target AMPK substrates and a decrease in a few of them in both cell lines (Fig. 5A). This suggests that the effect of various phosphorylation sites on AMPK activity is not general and is dependent on the cellular context and the particular target. Moreover, activation of AMPK has been reported to induce mitochondrial fission [58] and AMPK activation has been shown in the acute response to tamoxifen [59], which is in agreement with our results presented in Fig. 3 A-E. Sirtuins, NAD (+)-dependent deacetylases, represent other important fuel sensing and protective proteins linking antioxidant defense with metabolic adaptations. They regulate similar metabolic processes as AMPK and were reported to crosstalk with AMPK signaling through liver kinase B1 (LKB1 kinase) [60–62]. Sirtuins also participate in the normal functioning of mitochondria, controling the expression of mitochondrial biogenesis genes while reducing the expression of glycolytic genes [63]. Therefore, the logical extension of the study was to assess the mitochondrial sirtuins, in particular SIRT3. We have detected a clear upregulation of the mitochondrial SIRT3 in both Tam5R cell lines (Fig. 5B). Increased expression of SIRT3 is linked with adaptive response to stress, including metabolic reprogramming and enhancing antioxidant defense mechanisms [64–67]. Moreover, SIRT3 has been shown to be overexpressed in tamoxifen-resistant cells which is in agreement with our data [68]. Since SIRT3 regulates the function and assembly of the ETC components and has been shown to upregulate SOD2 and catalase expression [67], our results documenting high oxidative stress within mitochondria and activated antioxidant defense mechanisms (Fig. 3F and G) nicely corroborate these findings. Furthermore, SIRT3 has been reported to activate isocitrate dehydrogenase 2 (IDH2) catalyzing the reaction from isocitrate to α-ketoglutarate coupled with NADPH production. Similarly, SIRT3 activates acetyl-CoA synthetase 2 (ACS2), an enzyme that converts acetate into acetyl-CoA [63]. These events lead to an increased flux through the first reactions of tricarboxylic acid cycle and promote the production of metabolic intermediates that could serve as precursors for biosynthetic pathways. Higher protein level and activity of mitochondrial ACO2 in Tam5R cells presented in Fig. 4F strongly supports this hypothesis. Data are also in line with higher mtDNA content in Tam5R cells, as mitochondrial ACO2 has been shown to participate in the packaging and maintenance of mtDNA [69]. Isocitrate produced in aconitase reaction may be further converted by IDH2 to α –ketoglutarate, which after transport through the citrate/α-ketoglutarate shuttle into the cytosol can serve as a starting carbon skeleton for other anabolic reactions. Importantly mitochondrial NADPH can be utilized in mitochondria directly for the antioxidant defense to maintain the glutathione peroxidase or peroxiredoxin antioxidant systems or it can be exchanged via the citrate/α-ketoglutarate shuttle providing reducing equivalents for biosynthetic reactions such as lipid and nucleic acid synthesis [70].

To sum up, these data strongly support an important role of SIRT3 in metabolic rewiring and oxidative stress response within mitochondria of Tam5R cells which is in agreement with the report showing that silencing of SIRT3 sensitizes the breast cancer cells to treatment with cisplatin and tamoxifen [71]. Furthermore, AMPK activation in Tam5R cells promotes a metabolic switch from oxidative phosphorylation to enhanced glycolysis.

3.9. MCF7 cells devoid of mitochondrial DNA are resistant to tamoxifen and replicate the phenotype of Tam5R cells

In order to prove our finding of the link between tamoxifen resistance and diminished mitochondrial function on an independent alternative model, we analyzed the cytotoxic effect of short-term incubation of MCF7 ρ0 cells (lacking mtDNA) with tamoxifen. ρ0 cells do not contain mitochondrial respiratory complexes due to lack of 13 protein subunits coded by mtDNA and are thus respiration-deficient, showing a similar phenotype to Tam5R cells in this regard [72]. Our results show that these cells are significantly more resistant than parental MCF7 cells to the cytotoxic effects of tamoxifen (Fig. 5C), with 15 μM inducing only 32% of cell death in ρ0 cells (compared to 75% in Control cells). ρ0 cells are actually even more resistant than our Tam5R cells and their mtDNA depletion has also been linked to tamoxifen resistance [73]. Together, our data corroborate our hypothesis that low mitochondrial respiration and “dysfunction” of mitochondria confers resistance to tamoxifen.

4. Conclusions

Our study shows that cells cultivated for a long period in the presence of tamoxifen develop resistance, mimicking the situation in tamoxifen-treated human patients. These cells show profound mitochondrial changes and exhibit marked reduction in the amount and assembly of mitochondrial respiratory SCs. Such changes are linked with lower respiration, higher mitochondrial superoxide levels and more fragmented mitochondrial network that moves towards cellular periphery. On the molecular level, increased mitochondrial fission can be attributed to activation of DRP1 by phosphorylation at Ser637. These observations are coupled with the detected metabolic rewiring towards glycolysis, as evidenced by the activation of glucose uptake and glycolytic machinery. However, Tam5R cells exhibit LDH-A_{low}/LDH-

B_{high} phenotype, suggesting increased utilization of pyruvate for supporting their anabolic requirements. Further molecular events that are coupled with this phenotype are phosphorylation of AMPK at Ser485/491, increase in mitochondrial SIRT3 level and increased mitochondrial aconitase activity. We thus suggest that reduced mitochondrial function coupled with mitochondrial fragmentation could be linked to tamoxifen resistance and could be a marker that predicts therapeutic failure.

Funding

This work has been supported by GACR grants 16-12816S and 18-13103S to J.T., by the institutional suport of the Czech Academy of Sciences (RVO: 86652036). It was further suported by Kellner Family Foundation to J.T., by the European Regional Development Fund project BIOCEV (CZ.1.05/1.100) and also by the MEYS of CR within the LQ1604 National Sustainability Program II (Project BIOCEV-FAR).

Acknowledgements

We acknowledge the Imaging Methods Core Facility at BIOCEV for their support with obtaining flow cytometry and confocal microscopy data presented in this paper. We thank Dr. Roberto Bravo-Sagua from the Institute of Nutrition and Food Technology (INTA), University of Chile, for his kind assistance with image processing and analysis.

Appendix A. Supplementary data

Supplementary data to this article can be found online at https://doi.org/10.1016/j.freeradbiomed.2019.09.004.

References

[1] K.N. Anderson, R.B. Schwab, M.E. Martinez, Reproductive risk factors and breast cancer subtypes: a review of the literature, Breast Canc. Res. Treat. 144 (2014) 1–10.
[2] L. Bjornstrom, M. Sjoberg, Mechanisms of estrogen receptor signaling: convergence of genomic and nongenomic actions on target genes, Mol. Endocrinol. 19 (2005) 833–842.
[3] M. Chang, Tamoxifen resistance in breast cancer, Biomol Ther (Seoul) 20 (2012) 256–267.
[4] Tamoxifen for early breast cancer: an overview of the randomised trials. Early Breast Cancer Trialists' Collaborative Group, Lancet 351 (1998) 1451–1467.
[5] G. Early Breast Cancer Trialists' Collaborative, Effects of chemotherapy and hormonal therapy for early breast cancer on recurrence and 15-year survival: an overview of the randomised trials, Lancet 365 (2005) 1687–1717.
[6] A. Ring, M. Dowsett, Mechanisms of tamoxifen resistance, Endocr. Relat. Cancer 11 (2004) 643–658.
[7] R.B. Riggins, R.S. Schrecengost, M.S. Guerrero, A.H. Bouton, Pathways to tamoxifen resistance, Cancer Lett. 256 (2007) 1–24.
[8] I.R. Hutcheson, J.M. Knowlden, T.A. Madden, D. Barrow, J.M. Gee, A.E. Wakeling, et al., Oestrogen receptor-mediated modulation of the EGFR/MAPK pathway in tamoxifen-resistant MCF-7 cells, Breast Canc. Res. Treat. 81 (2003) 81–93.
[9] X. Zhang, Z.Y. Wang, Estrogen receptor-alpha variant, ER-alpha36, is involved in tamoxifen resistance and estrogen hypersensitivity, Endocrinology 154 (2013) 1990–1998.
[10] T.A. Hopp, H.L. Weiss, I.S. Parra, Y. Cui, C.K. Osborne, S.A. Fuqua, Low levels of estrogen receptor beta protein predict resistance to tamoxifen therapy in breast cancer, Clin. Cancer Res. 10 (2004) 7490–7499.
[11] E.L. Hayes, J.S. Lewis-Wambi, Mechanisms of endocrine resistance in breast cancer: an overview of the proposed roles of noncoding RNA, Breast Cancer Res. 17 (2015) 40.
[12] T. Joshi, D. Elias, J. Stenvang, C.L. Alves, F. Teng, M.B. Lyng, et al., Integrative analysis of miRNA and gene expression reveals regulatory networks in tamoxifen-resistant breast cancer, Oncotarget 7 (2016) 57239–57253.
[13] C.M. Klinge, miRNAs and estrogen action, Trends Endocrinol. Metab. 23 (2012) 223–233.
[14] S. Lettlova, V. Brynychova, J. Blecha, D. Vrana, M. Vondrusova, P. Soucek, et al., MiR-301a-3p suppresses estrogen signaling by directly inhibiting ESR1 in ERalpha positive breast cancer, Cell. Physiol. Biochem. 46 (2018) 2601–2615.
[15] L. Sas, F. Lardon, P.B. Vermeulen, J. Hauspy, P. Van Dam, P. Pauwels, et al., The interaction between ER and NFkappaB in resistance to endocrine therapy, Breast Cancer Res. 14 (2012) 212.
[16] J. Kumbrink, K.H. Kirsch, Regulation of p130(Cas)/BCAR1 expression in tamoxifen-sensitive and tamoxifen-resistant breast cancer cells by EGR1 and NAB2, Neoplasia 14 (2012) 108–120.
[17] R.S. Schrecengost, R.B. Riggins, K.S. Thomas, M.S. Guerrero, A.H. Bouton, Breast cancer antiestrogen resistance-3 expression regulates breast cancer cell migration through promotion of p130Cas membrane localization and membrane ruffling, Cancer Res. 67 (2007) 6174–6182.
[18] I. Larosche, P. Letteron, B. Fromenty, N. Vadrot, A. Abbey-Toby, G. Feldmann, et al., Tamoxifen inhibits topoisomerases, depletes mitochondrial DNA, and triggers steatosis in mouse liver, J. Pharmacol. Exp. Ther. 321 (2007) 526–535.
[19] P.I. Moreira, J. Custodio, A. Moreno, C.R. Oliveira, M.S. Santos, Tamoxifen and estradiol interact with the flavin mononucleotide site of complex I leading to mitochondrial failure, J. Biol. Chem. 281 (2006) 10143–10152.
[20] C. Tuquet, J. Dupont, A. Mesneau, J. Roussaux, Effects of tamoxifen on the electron transport chain of isolated rat liver mitochondria, Cell Biol. Toxicol. 16 (2000) 207–219.
[21] B.N. Radde, M.M. Ivanova, H.X. Mai, N. Alizadeh-Rad, K. Piell, P. Van Hoose, et al., Nuclear respiratory factor-1 and bioenergetics in tamoxifen-resistant breast cancer cells, Exp. Cell Res. 347 (2016) 222–231.
[22] M. Fiorillo, F. Sotgia, D. Sisci, A.R. Cappello, M.P. Lisanti, Mitochondrial "power" drives tamoxifen resistance: NQO1 and GCLC are new therapeutic targets in breast cancer, Oncotarget 8 (2017) 20309–20327.
[23] A.S. Tan, J.W. Baty, L.F. Dong, A. Bezawork-Geleta, B. Endaya, J. Goodwin, et al., Mitochondrial genome acquisition restores respiratory function and tumorigenic potential of cancer cells without mitochondrial DNA, Cell Metabol. 21 (2015) 81–94.
[24] M. Vondrusova, A. Bezawork-Geleta, K. Sachaphibulkij, J. Truksa, J. Neuzil, The effect of mitochondrially targeted anticancer agents on mitochondrial (super) complexes, Methods Mol. Biol. 1265 (2015) 195–208.
[25] Z. Rychtarcikova, S. Lettlova, V. Tomkova, V. Korenkova, L. Langerova, E. Simonova, et al., Tumor-initiating cells of breast and prostate origin show alterations in the expression of genes related to iron metabolism, Oncotarget 8 (2017) 6376–6398.
[26] R. Bravo-Sagua, C. Lopez-Crisosto, V. Parra, M. Rodriguez-Pena, B.A. Rothermel, A.F. Quest, et al., mTORC1 inhibitor rapamycin and ER stressor tunicamycin induce differential patterns of ER-mitochondria coupling, Sci. Rep. 6 (2016) 36394.
[27] W.H. Tong, T.A. Rouault, Functions of mitochondrial ISCU and cytosolic ISCU in mammalian iron-sulfur cluster biogenesis and iron homeostasis, Cell Metabol. 3 (2006) 199–210.
[28] E.R. Kisanga, J. Gjerde, A. Guerrieri-Gonzaga, F. Pigatto, A. Pesci-Feltri, C. Robertson, et al., Tamoxifen and metabolite concentrations in serum and breast cancer tissue during three dose regimens in a randomized preoperative trial, Clin. Cancer Res. 10 (2004) 2336–2343.
[29] B.M.A. Fernandes, S. Bighetti, J. Fernandes, V. Lanchote, C. Lopes, Correlation between plasma tamoxifen concentration and tumor response in patients with breast cancer: at neoadjuvant treatment with tamoxifen, Int. J. Pharm. Pharm. Sci. 9 (2017) 101–106.
[30] E.A. Perez, D.R. Gandara, M.J. Edelman, R. O'Donnell, I.J. Lauder, M. DeGregorio, Phase I trial of high-dose tamoxifen in combination with cisplatin in patients with lung cancer and other advanced malignancies, Canc. Invest. 21 (2003) 1–6.
[31] L.E. Shaw, A.J. Sadler, D. Pugazhendhi, P.D. Darbre, Changes in oestrogen receptor-alpha and -beta during progression to acquired resistance to tamoxifen and fulvestrant (Faslodex, ICI 182,780) in MCF7 human breast cancer cells, J. Steroid Biochem. Mol. Biol. 99 (2006) 19–32.
[32] Y.N. Loh, E.L. Hedditch, L.A. Baker, E. Jary, R.L. Ward, C.E. Ford, The Wnt signalling pathway is upregulated in an in vitro model of acquired tamoxifen resistant breast cancer, BMC Canc. 13 (2013) 174.
[33] X. Xue, Y.A. Yang, A. Zhang, K.W. Fong, J. Kim, B. Song, et al., LncRNA HOTAIR enhances ER signaling and confers tamoxifen resistance in breast cancer, Oncogene 35 (2016) 2746–2755.
[34] R. Acin-Perez, J.A. Enriquez, The function of the respiratory supercomplexes: the plasticity model, Biochim. Biophys. Acta 1837 (2014) 444–450.
[35] I. Lopez-Fabuel, J. Le Douce, A. Logan, A.M. James, G. Bonvento, M.P. Murphy, et al., Complex I assembly into supercomplexes determines differential mitochondrial ROS production in neurons and astrocytes, Proc. Natl. Acad. Sci. U. S. A. 113 (2016) 13063–13068.
[36] M.L. Genova, G. Lenaz, Functional role of mitochondrial respiratory supercomplexes, Biochim. Biophys. Acta 1837 (2014) 427–443.
[37] J. Hirst, Open questions: respiratory chain supercomplexes-why are they there and what do they do? BMC Biol. 16 (2018) 111.
[38] J.A. Letts, L.A. Sazanov, Clarifying the supercomplex: the higher-order organization of the mitochondrial electron transport chain, Nat. Struct. Mol. Biol. 24 (2017) 800–808.
[39] R.J. Youle, A.M. van der Bliek, Mitochondrial fission, fusion, and stress, Science 337 (2012) 1062–1065.
[40] G. Arena, M.Y. Cisse, S. Pyrdziak, L. Chatre, R. Riscal, M. Fuentes, et al., Mitochondrial MDM2 regulates respiratory complex I activity independently of p53, Mol. Cell 69 (2018) 594–609 e8.
[41] W.J. Wang, Y. Wang, J.Y. Long, J.R. Wang, S.B. Haudek, P. Overbeek, et al., Mitochondrial fission triggered by hyperglycemia is mediated by ROCK1 activation in podocytes and endothelial cells, Cell Metabol. 15 (2012) 186–200.
[42] T. Yu, J.L. Robotham, Y. Yoon, Increased production of reactive oxygen species in hyperglycemic conditions requires dynamic change of mitochondrial morphology, Proc. Natl. Acad. Sci. U. S. A. 103 (2006) 2653–2658.
[43] P.E. Porporato, V.L. Payen, J. Perez-Escuredo, C.J. De Saedeleer, P. Danhier, T. Copetti, et al., A mitochondrial switch promotes tumor metastasis, Cell Rep. 8 (2014) 754–766.
[44] M. Peiris-Pages, G. Bonuccelli, F. Sotgia, M.P. Lisanti, Mitochondrial fission as a driver of stemness in tumor cells: mDIVI1 inhibits mitochondrial function, cell migration and cancer stem cell (CSC) signalling, Oncotarget 9 (2018)

13254–13275.
[45] S.Y. Han, Y.J. Jeong, Y. Choi, S.K. Hwang, Y.S. Bae, Y.C. Chang, Mitochondrial dysfunction induces the invasive phenotype, and cell migration and invasion, through the induction of AKT and AMPK pathways in lung cancer cells, Int. J. Mol. Med. 42 (2018) 1644–1652.
[46] J. Zhao, J. Zhang, M. Yu, Y. Xie, Y. Huang, D.W. Wolff, et al., Mitochondrial dynamics regulates migration and invasion of breast cancer cells, Oncogene 32 (2013) 4814–4824.
[47] F. Ciccarese, V. Ciminale, Escaping death: mitochondrial redox homeostasis in cancer cells, Front. Oncol. 7 (2017) 117.
[48] D.C. Wallace, Mitochondria and cancer, Nat. Rev. Cancer 12 (2012) 685–698.
[49] H.M. Wilkins, J.L. Harris, S.M. Carl, L. E, J. Lu, J. Eva Selfridge, et al., Oxaloacetate activates brain mitochondrial biogenesis, enhances the insulin pathway, reduces inflammation and stimulates neurogenesis, Hum. Mol. Genet. 23 (2014) 6528–6541.
[50] J.R. Bain, R.D. Stevens, B.R. Wenner, O. Ilkayeva, D.M. Muoio, C.B. Newgard, Metabolomics applied to diabetes research: moving from information to knowledge, Diabetes 58 (2009) 2429–2443.
[51] S.M. Ronnebaum, O. Ilkayeva, S.C. Burgess, J.W. Joseph, D. Lu, R.D. Stevens, et al., A pyruvate cycling pathway involving cytosolic NADP-dependent isocitrate dehydrogenase regulates glucose-stimulated insulin secretion, J. Biol. Chem. 281 (2006) 30593–30602.
[52] B.J. Altman, Z.E. Stine, C.V. Dang, From Krebs to clinic: glutamine metabolism to cancer therapy, Nat. Rev. Cancer 16 (2016) 773.
[53] R.M. Chin, X. Fu, M.Y. Pai, L. Vergnes, H. Hwang, G. Deng, et al., The metabolite alpha-ketoglutarate extends lifespan by inhibiting ATP synthase and TOR, Nature 510 (2014) 397–401.
[54] S. Liu, L. He, K. Yao, The antioxidative function of alpha-ketoglutarate and its applications, BioMed Res. Int. 2018 (2018) 3408467.
[55] S. Herzig, R.J. Shaw, AMPK: guardian of metabolism and mitochondrial homeostasis, Nat. Rev. Mol. Cell Biol. 19 (2018) 121–135.
[56] S.C. Stein, A. Woods, N.A. Jones, M.D. Davison, D. Carling, The regulation of AMP-activated protein kinase by phosphorylation, Biochem. J. 345 (Pt 3) (2000) 437–443.
[57] K.A. Coughlan, R.J. Valentine, B.S. Sudit, K. Allen, Y. Dagon, B.B. Kahn, et al., PKD1 inhibits AMPKalpha2 through phosphorylation of serine 491 and impairs insulin signaling in skeletal muscle cells, J. Biol. Chem. 291 (2016) 5664–5675.
[58] E.Q. Toyama, S. Herzig, J. Courchet, T.L. Lewis Jr., O.C. Loson, K. Hellberg, et al., Metabolism. AMP-activated protein kinase mediates mitochondrial fission in response to energy stress, Science 351 (2016) 275–281.
[59] N.A. Daurio, S.W. Tuttle, A.J. Worth, E.Y. Song, J.M. Davis, N.W. Snyder, et al., AMPK activation and metabolic reprogramming by tamoxifen through estrogen receptor-independent mechanisms suggests new uses for this therapeutic modality in cancer treatment, Cancer Res. 76 (2016) 3295–3306.
[60] N.B. Ruderman, X.J. Xu, L. Nelson, J.M. Cacicedo, A.K. Saha, F. Lan, et al., AMPK and SIRT1: a long-standing partnership? Am. J. Physiol. Endocrinol. Metab. 298 (2010) E751–E760.
[61] J.E. Huh, J.H. Shin, E.S. Jang, S.J. Park, D.R. Park, R. Ko, et al., Sirtuin 3 (SIRT3) maintains bone homeostasis by regulating AMPK-PGC-1beta axis in mice, Sci. Rep. 6 (2016) 22511.
[62] B. Kincaid, E. Bossy-Wetzel, Forever young: SIRT3 a shield against mitochondrial meltdown, aging, and neurodegeneration, Front. Aging Neurosci. 5 (2013) 48.
[63] B. Martinez-Pastor, R. Mostoslavsky, Sirtuins, metabolism, and cancer, Front. Pharmacol. 3 (2012) 22.
[64] H.J. Weir, J.D. Lane, N. Balthasar, SIRT3: a central regulator of mitochondrial adaptation in health and disease, Genes Cancer 4 (2013) 118–124.
[65] E. Verdin, M.D. Hirschey, L.W. Finley, M.C. Haigis, Sirtuin regulation of mitochondria: energy production, apoptosis, and signaling, Trends Biochem. Sci. 35 (2010) 669–675.
[66] B. Osborne, N.L. Bentley, M.K. Montgomery, N. Turner, The role of mitochondrial sirtuins in health and disease, Free Radic. Biol. Med. 100 (2016) 164–174.
[67] A.S. Bause, M.C. Haigis, SIRT3 regulation of mitochondrial oxidative stress, Exp. Gerontol. 48 (2013) 634–639.
[68] L. Zhang, X. Ren, Y. Cheng, K. Huber-Keener, X. Liu, Y. Zhang, et al., Identification of Sirtuin 3, a mitochondrial protein deacetylase, as a new contributor to tamoxifen resistance in breast cancer cells, Biochem. Pharmacol. 86 (2013) 726–733.
[69] X.J. Chen, X. Wang, B.A. Kaufman, R.A. Butow, Aconitase couples metabolic regulation to mitochondrial DNA maintenance, Science 307 (2005) 714–717.
[70] T.S. Blacker, M.R. Duchen, Investigating mitochondrial redox state using NADH and NADPH autofluorescence, Free Radic. Biol. Med. 100 (2016) 53–65.
[71] M. Torrens-Mas, D.G. Pons, J. Sastre-Serra, J. Oliver, P. Roca, SIRT3 silencing sensitizes breast cancer cells to cytotoxic treatments through an increment in ROS production, J. Cell. Biochem. 118 (2017) 397–406.
[72] N.S. Chandel, P.T. Schumacker, Cells depleted of mitochondrial DNA (rho0) yield insight into physiological mechanisms, FEBS Lett. 454 (1999) 173–176.
[73] A. Naito, J. Carcel-Trullols, C.H. Xie, T.T. Evans, T. Mizumachi, M. Higuchi, Induction of acquired resistance to antiestrogen by reversible mitochondrial DNA depletion in breast cancer cell line, Int. J. Cancer 122 (2008) 1506–1511.

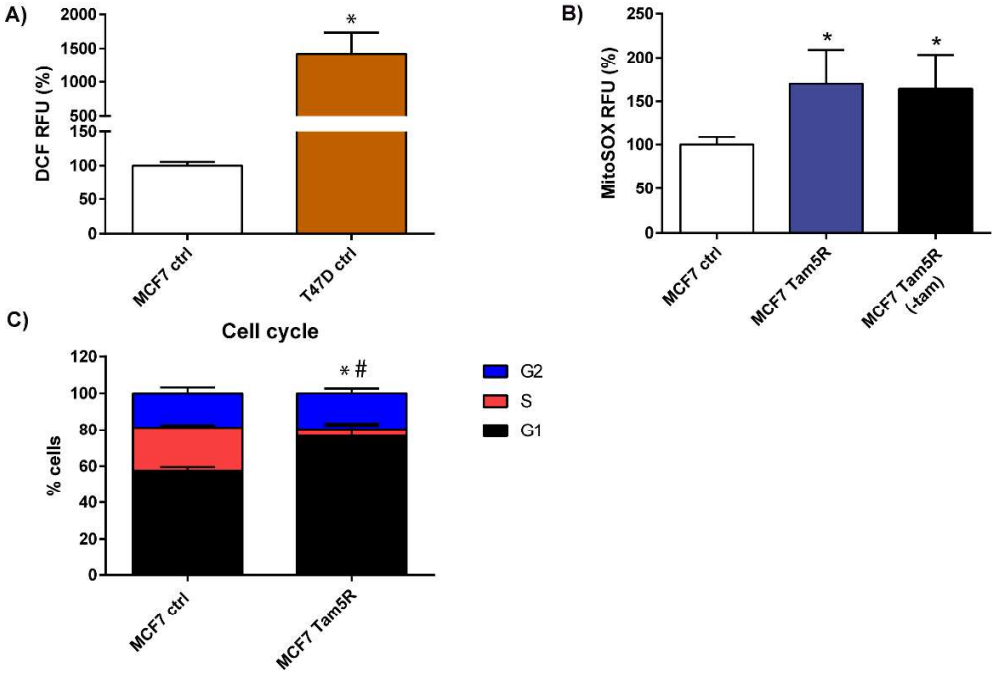

Supplementary figure S1. (A) Quantification of basal cellular ROS production in MCF7 and T47D cells using the fluorescent probe dichlorofluorescein (DCF) by flow cytometry. Results are expressed as % of DCF relative fluorescence units (RFU) normalized to MCF7 Ctrl cells and represent the mean ± SD of at least 3 independent experiments. *$p \leq 0.05$ relative to MCF7 Ctrl cells. **(B)** Quantification of mitochondrial superoxide levels in MCF7 Control, Tam5R cells and Tam5R cells cultivated without tamoxifen for 4 weeks, using the fluorescent probe MitoSOX™ by flow cytometry. Results are expressed as % of MitoSOX RFU normalized to MCF7 Ctrl cells and represent the mean ± SD of at least 3 independent experiments. *$p \leq 0.05$ relative to MCF7 Ctrl cells.

www.impactjournals.com/oncotarget/ Oncotarget, 2017, Vol. 8, (No. 4), pp: 6376-6398

Research Paper

Tumor-initiating cells of breast and prostate origin show alterations in the expression of genes related to iron metabolism

Zuzana Rychtarcikova[1,2,*], Sandra Lettlova[1,3,*], Veronika Tomkova[1,3], Vlasta Korenkova[1], Lucie Langerova[1], Ekaterina Simonova[1], Polina Zjablovskaja[4], Meritxell Alberich-Jorda[4], Jiri Neuzil[1,5], Jaroslav Truksa[1]

[1]Institute of Biotechnology, Czech Academy of Sciences, Prague, Czech Republic

[2]Charles University in Prague, Faculty of Pharmacy in Hradec Kralove, Hradec Kralove, Czech Republic

[3]Charles University in Prague, Faculty of Sciences, Prague, Czech Republic

[4]Institute of Molecular Genetics, Czech Academy of Sciences, Prague, Czech Republic

[5]School of Medical Science, Menzies Health Institute Queensland, Southport, Queensland, Australia

[*]These authors contributed equally to this work

Correspondence to: Jaroslav Truksa, **email:** jaroslav.truksa@ibt.cas.cz

Keywords: *tumor-initiating cells, breast cancer, iron metabolism, FeS cluster, stem cells*

Received: *January 12, 2016* ***Accepted:*** *November 30, 2016* ***Published:*** *December 22, 2016*

ABSTRACT

The importance of iron in the growth and progression of tumors has been widely documented. In this report, we show that tumor-initiating cells (TICs), represented by spheres derived from the MCF7 cell line, exhibit higher intracellular labile iron pool, mitochondrial iron accumulation and are more susceptible to iron chelation. TICs also show activation of the IRP/IRE system, leading to higher iron uptake and decrease in iron storage, suggesting that level of properly assembled cytosolic iron-sulfur clusters (FeS) is reduced. This finding is confirmed by lower enzymatic activity of aconitase and FeS cluster biogenesis enzymes, as well as lower levels of reduced glutathione, implying reduced FeS clusters synthesis/utilization in TICs. Importantly, we have identified specific gene signature related to iron metabolism consisting of genes regulating iron uptake, mitochondrial FeS cluster biogenesis and hypoxic response (*ABCB10*, *ACO1*, *CYBRD1*, *EPAS1*, *GLRX5*, *HEPH*, *HFE*, *IREB2*, *QSOX1* and *TFRC*). Principal component analysis based on this signature is able to distinguish TICs from cancer cells *in vitro* and also Leukemia-initiating cells (LICs) from non-LICs in the mouse model of acute promyelocytic leukemia (APL). Majority of the described changes were also recapitulated in an alternative model represented by MCF7 cells resistant to tamoxifen (TAMR) that exhibit features of TICs. Our findings point to the critical importance of redox balance and iron metabolism-related genes and proteins in the context of cancer and TICs that could be potentially used for cancer diagnostics or therapy.

INTRODUCTION

Iron is an indispensable micro-nutrient, on which most living organisms depend for their existence due to its ability to shuffle between ferrous and ferric form and participate in crucial redox reactions. Iron also serves as a metal cofactor needed for DNA synthesis and repair as well as a cofactor of many metabolic enzymes and enzymes of the respiratory complexes in mitochondria [1, 2, 3].

There are many iron metabolism-related proteins that play pivotal role in cellular iron handling, for example proteins related to iron uptake such as transferrin receptor (TFR1 encoded by the *TFRC*) and cytochrome b reductase (coded by *CYBRD1*) [3, 4] as well as regulators participating in iron storage such as ferritin encoded by the *FTH* and *FTL* genes [5]. Additional proteins participating in the iron utilization and FeS cluster assembly are glutaredoxin 5 (encoded by *GLRX5*) and ATP binding cassette subfamily B member 10 (coded

by *ABCB10*) [1, 6, 7]. There are other critical enzymes participating in the iron sensing such as iron responsive protein 1 (IRP1) encoded by the aconitase (*ACO1)* gene and iron responsive protein 2 (IRP2) coded by the iron responsive element binding protein 2 (*IREB2*) gene [8]. These proteins play a crucial role in assessing the intracellular iron level and eliciting appropriate response by modulating iron uptake and iron storage *via* binding to the iron responsive elements (IRE) located at the 5´and 3´prime untranslated regions of the corresponding mRNA [9]. Furthermore, there is a tight crosstalk between the hypoxic response of the cell and cellular iron metabolism as low iron levels elicit activation of the hypoxia inducible factors (HIF) encoded by the *HIF1A* and endothelial Per-ARNT-Sim Domain Protein 1 (*EPAS1*) genes [10]. Activation of these genes is connected with higher iron uptake through CYBRD1 in the enterocytes [11] and in the non-physiological setting it is connected with activation of tissue remodelling factors such as quiescin sulfhydryl oxidase1 (coded by *QSOX1)* [12]. Other important regulators of iron metabolism represent proteins involved in iron export such as hephaestin encoded by the *HEPH* gene and ferroportin ecoded by the solute carrier family 40 member 1 (*SLC40A1*) gene [13, 14]. Additional proteins participating in the iron uptake and non-transferrin bound iron uptake (NTBI) such as natural resistance associated protein (NRAMP2) coded by the solute carrier family 11 member 2 (*SLC11A2*) gene and zinc importer protein 14 (ZIP14) encoded by the solute carrier family 39 member 14 (*SLC39A14*) play an important role in the cellular and systemic iron metabolism together with the hemochromatosis (*HFE*) gene and protein which is connected with excessive iron loading [3, 15–20]

The role of iron in the progression and growth of tumor cells has been documented in various studies describing higher iron uptake in cancer cells due to their proliferative nature and altered metabolic needs [21–23]. The correlation between the iron content in the diet and tumorigenesis has also been proposed, suggesting iron as a risk factor for some cancer subtypes, such as haematological malignities or hepatocellular carcinoma. Molecular mechanisms underlying this phenomenon are diverse and include higher iron uptake *via* transferrin receptor, activation of hypoxia-inducible factors (HIFs) in cancer cells due to compromised function of the prolyl hydroxylases and deregulation of signaling pathways such as Wnt/β-catenin [24–31].

It has been shown that iron-deprivation is able to induce apoptosis in tumor cells, particularly in cells of hematopoietic origin. Additionally, gallium nitrate, a competitor of the iron ion, has been successfully used to treat bladder cancer in a clinical setting [32–35].

The concept of cancer stem cells (CSC) or tumor-initiating cells (TICs) has emerged recently, documenting the extreme plasticity and heterogeneity of tumor tissue. This concept states that only a small sub-fraction of tumor cells is able to initiate tumor growth *in vivo* and that cells possessing this capability cause residual disease leading to relapse and death, although it is probably not universal concept for all cancer types [36–38]. This is of crucial clinical importance and there is virtually no data on iron metabolism in these cells, with only emerging evidence that HIFs play an important role in their maintenance and renewal [39–48].

Recently, there have been several attempts to correlate iron metabolism-related genes with the survival and overall prognosis of tumor progression in breast cancer patients. Miller et al. have shown that loss of the iron excretory genes and also upregulation of the iron uptake machinery impacts the prognosis and can delineate patients that would respond well in the group of hard-to-treat individuals and *vice versa* [49]. However, changes in the expression of these genes in TICs remains elusive so far.

Our study provides an insight into iron metabolism of TICs, their response to iron withdrawal, and identifies a specific gene signature related to iron metabolism that is differentially expressed in TICs. We have also identified iron metabolism-related proteins that are differentially expressed in TICs and could be utilized in cancer diagnosis or treatment.

RESULTS AND DISCUSSION

There are virtually no data concerning the role of iron and its metabolism in the maintenance and self-renewal of tumor-initiating cells (TICs) as yet. We thus focused our study on this particular topic and assessed iron content, sensitivity to iron chelators, iron uptake and storage, intracellular iron distribution and expression profile of iron metabolism-related genes in TICs.

Spheres as an *in vitro* model of TICs

We have used previously published methods to generate cells growing as spheres from the breast cancer cell line MCF7 *via* two alternative methods. The first method is based on serum-free medium and cells generated by this method are referred to as “spheres” [50]. An alternative method [51] based on the non-adherent plastic resulted in cells referred to as “agar”. In our experience, the serum-free approach generated spheres with more profound expression of stem cell/epithelia-mesenchymal transition (EMT) markers, yet in some cell lines such as DU-145, only the agar approach worked as they did not form spheres under serum-free conditions. We also included a non-malignant cell line of breast origin, MCF-10A; we were unable to generate spheres from these cells by either of the above mentioned approaches, pointing to the fact that malignant but not immortalized cells are able to form spheres in our hands. The appearance of MCF7 spheres is depicted in

Figure 1A and Supplementary Figure S1 shows expression of identical markers in all tested cell lines, documenting successful generation of spheres that represent *in vitro* model of TICs.

MCF7 spheres show higher labile iron pool (LIP) and iron uptake, higher amount of iron within mitochondria and are sensitive to iron chelation

In order to characterize iron metabolism of TICs, we first inspected the level of LIP within the MCF7 sphere cells using the calcein fluorescence-based approach [52] and found significantly higher level of LIP in TICs (Figure 1B). To confirm our findings, we examined the ability of cells to acquire radioactive ^{55}Fe and demonstrated that MCF7 spheres show significantly higher cellular ^{55}Fe uptake (Figure 1C) and significantly higher ^{55}Fe level in mitochondria (Figure 1D).

Further tests showed that application of cell permeable iron chelator such as salicyl isonicotinoyl hydrazone (SIH) resulted in decreased survival of MCF7 spheres compared to control adherent cells as measured by the Cell Titer-Glo (Figure 1E) and Cell Titer-Fluor (Figure 1F) cell viability assays. MCF7 spheres lost their ATP levels much faster and also exhibited higher numbers of dead cells compared to controls (Figure 1E–1F).

These data document higher iron uptake and labile iron pool, differential intracellular iron distribution with mitochondrial iron accumulation in MCF7 spheres as well as the necessity of iron for their survival. In order to find the underlying mechanism explaining this phenomenon, we performed expression profiling of genes that are related to iron metabolism.

TICs derived from various cancer cell lines show deregulation of genes related to iron metabolism

We performed expression profiling of selected 40 genes that cover iron uptake, export, transport, utilization, FeS cluster biogenesis, heme metabolisms, hypoxia inducible factors and other important regulators of iron metabolism in TICs generated from MCF7, BT-474, T-47D, ZR-75–30 breast and LNCaP and DU145 prostate cancer cells. We obtained expression profiles of 34 selected iron metabolism-related genes that were detectable and showed acceptable qPCR standard curves. Raw data showing actual values and genes tested are supplied in Supplementary Table S3.

We then compared the fold change in mRNA expression between TICs prepared by the sphere approach and control cells (Supplementary Table S1) and selected genes with altered expression (> 1.5 fold change in mRNA expression) that is reproducible among cell lines (a similar change occurs in more than 60% of cell lines), resulting in the iron metabolism-related gene signature differentially expressed in TICs (*ABCB10, ACO1, CYBRD1, EPAS1, GLRX5, HEPH, HFE, IREB2, QSOX1 and TFRC)*. Individual genes participating in the

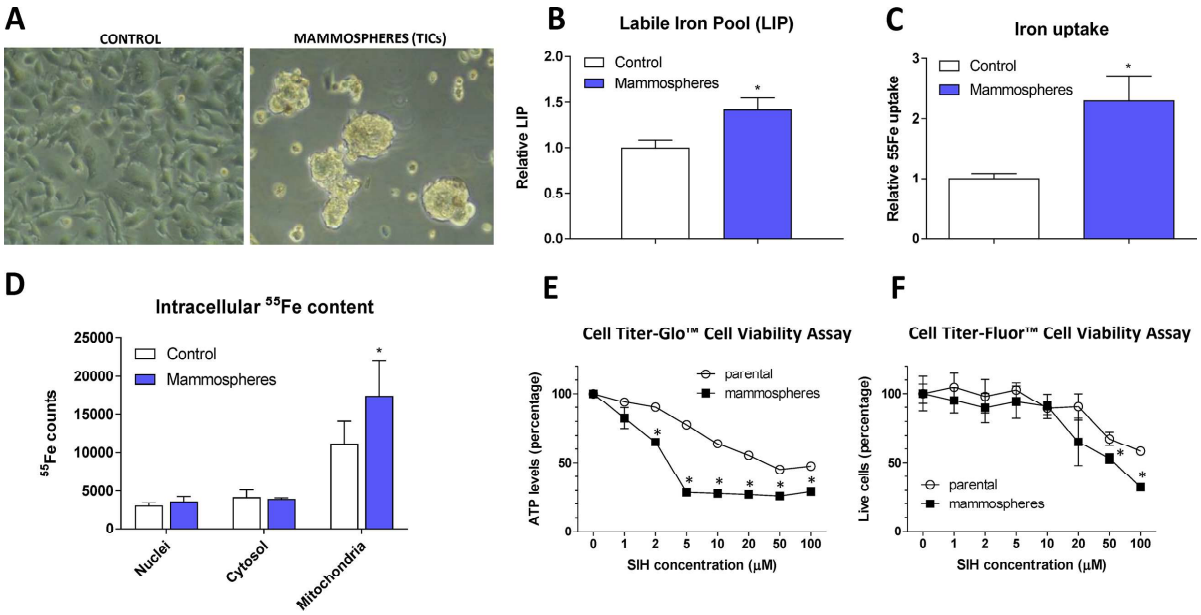

Figure 1: Appearance, labile iron pool, iron uptake, intracellular localization and sensitivity to chelators in tumor-initiating cells (TICs). The appearance of MCF7 cell grown either under control or sphere forming conditions is shown (**A**), together with Labile iron pool (LIP) detected by the calcein method (**B**), assessment of the ^{55}Fe uptake (**C**) and intracellular distribution of ^{55}Fe (**D**). Cells were also assayed for their resistance to cell death by two approaches - Cell Titer-Glow (**E**) and Cell Titer-Fluor (**F**). Experiments were performed at least in triplicate, standard error is SEM. *P*-values lower than 0.05 are denoted with a star and were calculated by the GraphPad Prism software using the unpaired *t*-test.

iron uptake (*CYBRD1, TFRC*), iron sensing and regulation (*ACO1, IREB2*), mitochondrial iron-sulphur cluster assembly (*ABCB10, GLRX5*), hypoxia response (*EPAS1, QSOX1*), iron export (*HEPH*) and iron overload (*HFE*) are discussed below.

Expression of cytochrome b reductase (CYBRD1) and transferrin receptor 1 (TFR1) participating in iron uptake is higher in TICs

CYBRD1 is an enzyme highly expressed at the duodenal brush border membrane. Product of the *CYBRD1* gene reduces ferric iron to ferrous iron and plays an important role in iron uptake from the intestine [4]. Its role in cancer is only emerging with documented overexpression in colorectal and oesophageal cancer [53, 54]. Our data showed upregulation of *CYBRD1* mRNA in most cell lines tested (MCF7, T-47D, BT-474, ZR-75–30, DU-145) with approximately 2 to 7-fold induction in TICs (Figure 2A, Supplementary Table S1), and this has been replicated on the protein level for the smaller 25 kDa CYBRD1 isoform in our MCF7 sphere model (Figure 2B). Since molecular mechanism linking CYBRD1 to cancer is missing at this point, we can only speculate that this enzyme could be regulated by members of the HIF family and enhance uptake of non-transferrin bound iron [55].

TFRC gene codes for TFR1 protein, a critical component of the transferrin-bound iron uptake. Elevated expression of TFR1 has been frequently reported in many cancers with possible links to poor prognosis and

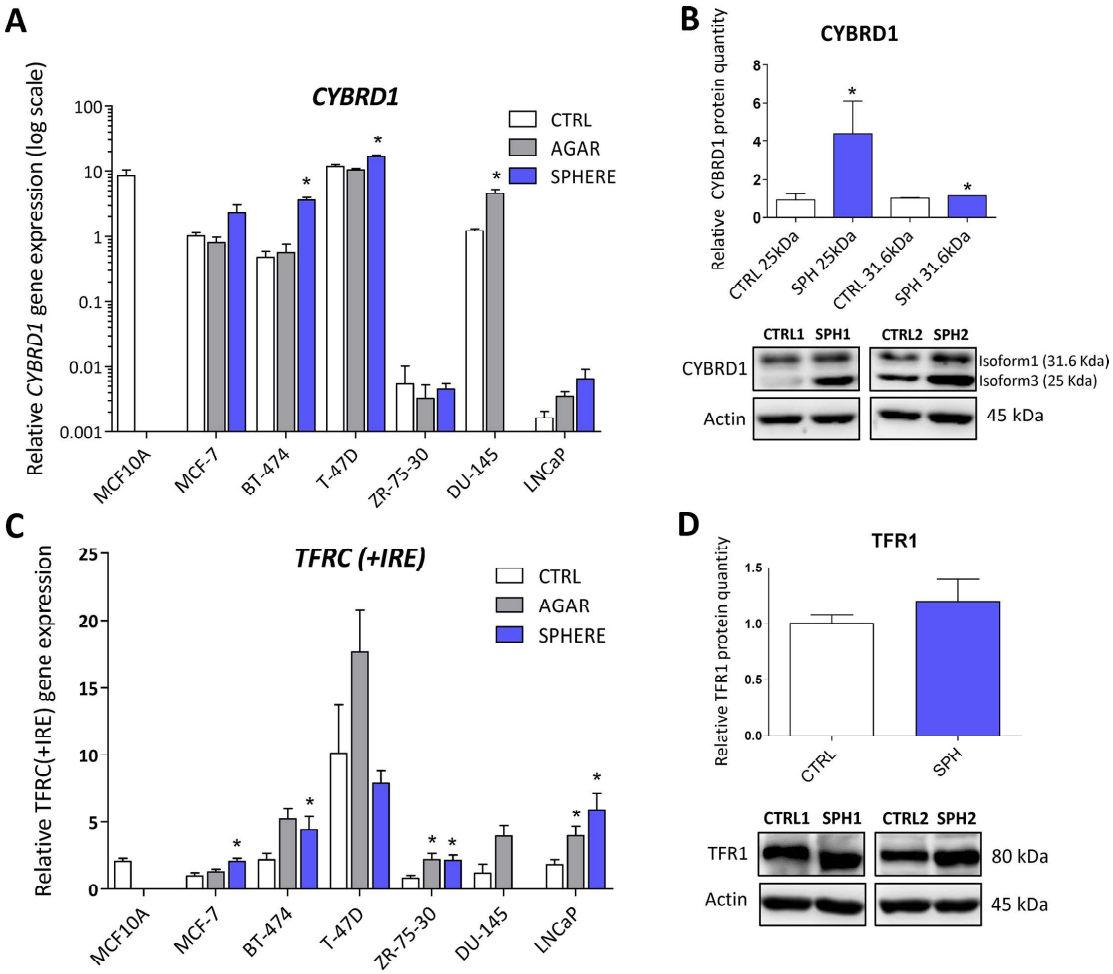

Figure 2: Expression of cytochrome b reductase (CYBRD1) and transferrin receptor 1 (TFR1) participating in iron uptake is higher in tumor-initiating cells (TICs). Expression of the *CYBRD1* gene at the mRNA level in breast non-malignant cell line MCF10A, in TICs derived from breast cancer cell lines MCF-7, BT-474, T-47D and ZR-75-30 as well as from prostate cancer cell lines DU-145 and LNCaP has been determined (**A**) together with protein levels in the MCF-7 cell line (CTRL) and MCF-7 derived spheres (SPH) (**B**). Similarly, the expression of the *TFRC* gene at the mRNA (**C**) level as well as protein level (**D**) in TICs is documented. Experiments were performed at least in triplicate, standard error is SEM, *p*-values lower than 0.05 are denoted with a star and were calculated by the GenEx software using the unpaired *t*-test and plotted with GraphPad prism software. The protein expression was quantified by the image J software from 2 to 5 independent samples, standard error is SEM, *p*-values lower than 0.05 are denoted with a star and were calculated and plotted in GraphPad prism, using the unpaired *t*-test.

acceleration of the disease [27, 53, 54, 56]. The expression of this gene is reproducibly elevated in TICs derived by the sphere approach in MCF7, BT-474, LNCaP and ZR-75–30, similarly, this change is also seen with the "agar" approach in BT-474, DU-145, LNCaP, T-47D and ZR-75–30 cells (Figure 2C, Supplementary Table S1). On the protein level, we could see increased levels in spheres derived from MCF7 cells even though not reaching the statistical significance of $p = 0.05$ (Figure 2D). Since the expression of TFR1 is regulated by the iron responsive protein/iron responsive element (IRP/IRE) system, we focused on the expression and activity of its components (ACO1, IREB2).

Iron responsive protein/Iron responsive element (IRP/IRE) components are deregulated and show activation of the IRP/IRE binding in TICs

Aconitase, also known as IRP1 or iron-responsive element-binding protein 1 (IREB1) is encoded by the *ACO1* gene. Under normal conditions, this protein functions as a metabolic enzyme participating in the conversion of citrate to isocitrate [57]. However, since ACO1 is an enzyme containing 4Fe-4S clusters as a co-factor, under iron deprivation, this enzyme dramatically changes its conformation and becomes the IRP1 with high affinity to iron-response elements (IREs) within untranslated regions (UTR) of many genes participating in the uptake and storage of iron, resulting in stabilization (3′UTR) or translation inhibition (5′UTR) of the corresponding mRNA, aiming to increase iron uptake and decrease iron storage [8, 9, 58]. There is emerging evidence about the role of ACO1 in cancer as elevated ACO1 expression suppresses tumor growth *in vivo* and its level is higher in rectal and hepatocellular carcinoma, while the opposite has been shown in leukemic cells [59–62]. Furthermore, many studies describe higher levels of isocitrate in cancer and cancer stem cells, supporting the role of ACO1 in carcinogenesis [63–66]. In our experimental system, we see approximately 2-fold increase in *ACO1* mRNA in all tested cell lines (Figure 3A, Supplementary Table S1). Moreover, these changes were replicated on the protein level of ACO1, where elevated protein levels are seen in the MCF7 sphere model (Figure 3B). Our data support the notion that ACO1 is upregulated in TICs and may play an important role in their biology.

The second protein binding to IREs is encoded by the *IREB2* gene and is also known as IRP2. This protein plays a critical role in the response to iron deprivation and is stabilized under conditions of low iron while under normal iron levels it is rapidly degraded [53, 67–69]. The role of IRP2 in carcinogenesis is only beginning to be appreciated [53, 70–73]. We have found mild, yet significant, upregulation of *IREB2* mRNA in all TICs derived by the sphere approach, with an average 2-fold change (Figure 3C, Supplementary Table S1). Contrary to this, we have detected an inverse relationship on the protein level, with downregulation of the IREB2 protein in MCF7 sphere cells (Figure 3D). This, though, has a plausible explanation, as IRP2 is normally degraded when iron level is high enough and its turnover is mediated by ubiquitinylation [74]. Since TICs contain higher levels of LIP, a decrease in IRP2 levels is expected.

We have further analysed the ability of IRP1/2 to bind the IRE motif and regulate iron uptake and storage by a modified electrophoretic mobility shift assay (EMSA). Our data clearly document activation of the IRP/IRE system showing enhanced binding mostly of the IRP1 to the IRE sequence of human ferritin (Figure 3E), which is in agreement with observed higher iron uptake, predicting that ferritin level would be decreased.

Interestingly, IRP1 activity is regulated by the absence of the assembled FeS cluster as already mentioned. We have thus focused our attention on the components of the mitochondrial FeS cluster biogenesis that show differential expression according to our expression profiling data.

Protein levels of the ATP Binding Cassette Subfamily B Member 10 (ABCB10) and glutaredoxin 5 (GLRX5) participating in mitochondrial FeS cluster assembly are decreased in TICs

ABCB10 is a protein belonging to the ABC transporter family that has mitochondrial localization, participates in the mitochondrial FeS cluster biogenesis and was proposed to mediate protection from reactive oxygen species (ROS) [75]. Its expression has been linked to erythroid heme synthesis; *Abcb10* knockout mice suffer from anemia and show mitochondrial iron accumulation [76–78]. Even though our data document rather small (2-fold), yet significant, increase in *ABCB10* mRNA expression in all tested cell lines (Figure 4A, Supplementary Table S1), we detected a profound decrease in the ABCB10 protein level in the MCF7 sphere model of TICs (Figure 4B). This suggests that ABCB10 protein level is probably regulated by a posttranscriptional mechanism. Our data are consistent with the fact that ABCB10 expression is increased during erythroid differentiation while TICs represent de-differentiated cells with stem cell properties [79] and also comply with the fact that low level of ABCB10 is connected with mitochondrial iron accumulation as seen in Figure 1D.

Glutaredoxin 5 is another component of the mitochondrial FeS cluster machinery. This protein is an important member of the redox balance system, being able to reduce the S-S bonds into free SH groups; oxidized GLRX5 is then non-enzymatically reduced by glutathione (GSH) [80–82]. This protein is critically

required for normal mitochondrial FeS cluster biogenesis as its disruption is associated with autosomal recessive pyridoxine-refractory sideroblastic anemia [6, 7, 83–85]. There is a scarce evidence about the role of GLRX5 in carcinogenesis, documenting higher expression of GLRX5 in hepatocellular carcinoma [86]. Interestingly, the expression of this critical component of FeS cluster biogenesis was supressed on the mRNA level in almost all tested cell lines (Figure 4C, Supplementary Table S1) as well as on the protein level in the MCF7 sphere model (Figure 4D). Thus, we can speculate that lower protein levels of GLRX5 may reduce proper FeS cluster biogenesis and since FeS clusters are essential for proper DNA repair and replication [1, 87], these alterations could lead to genomic instability of TICs.

Reduced enzymatic activity of FeS cluster containing enzymes, reduced glutathione (GSH) content and increased reactive oxygen species (ROS) levels in TICs

As we detected activation of the IRP/IRE system and changes in the expression of ABCB10 and GLRX5 that may reduce proper assembly and transport of FeS clusters, we assessed the enzymatic activity of ACO1 (both the cytosolic and mitochondrial form) and also mitochondrial respiratory complex I. Both of these enzymes require FeS clusters for their enzymatic function and lack of properly formed FeS clusters should lead to their lower enzymatic activity. Indeed, our data support this scenario (Figure 5A, 5B). Furthermore,

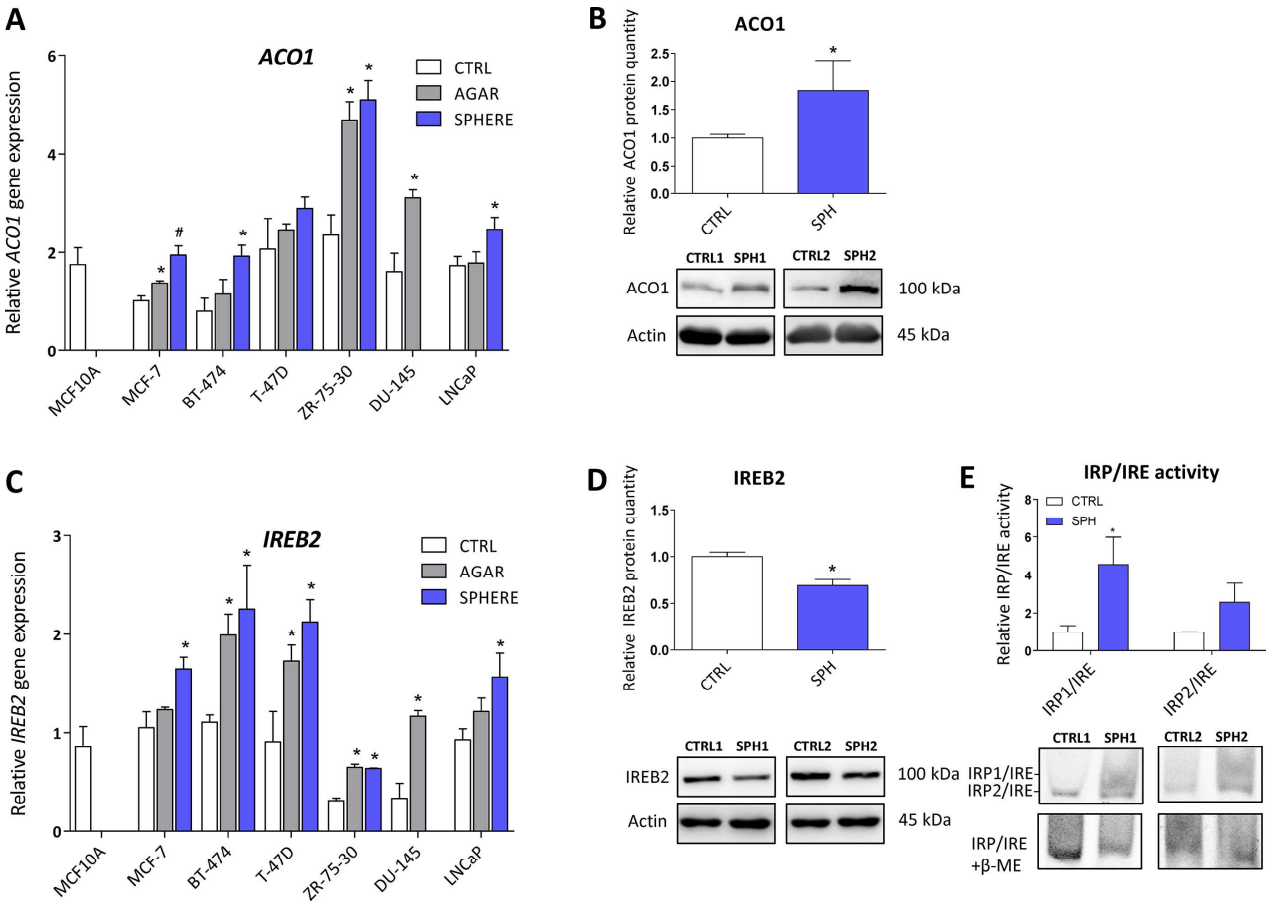

Figure 3: Iron responsive protein/Iron responsive element (IRP/IRE) components are deregulated and show activation of the IRP/IRE binding in tumor-initiating cells (TICs). Expression of the *ACO1* gene at the mRNA level in breast non-malignant cell line MCF10A, in TICs derived from breast cancer cell lines MCF-7, BT-474, T-47D and ZR-75-30 as well as from prostate cancer cell lines DU-145 and LNCaP has been determined (**A**) together with protein levels in the MCF-7 cell line (CTRL) and MCF-7 derived spheres (SPH) (**B**). Similarly, the expression of the *IREB2* gene at the mRNA (**C**) level as well as protein level (**D**) in TICs is documented. Experiments were performed at least in triplicate, standard error is SEM, *p*-values lower than 0.05 are denoted with a star and were calculated by the GenEx software using the unpaired *t*-test and plotted with GraphPad prism software. Number sign denotes statistical significance involving Dun-Bonferroni correction. Panel (**E**) illustrates the IRP/IRE activity measured by the fluorescent EMSA. The protein expression was quantified by the image J software from 2 to 5 independent samples, standard error is SEM, *p*-values lower than 0.05 are denoted with a star and were calculated and plotted in GraphPad prism, using the unpaired *t*-test.

as the decreased enzymatic ACO1 activity is linked to oxidative damage [88], we tested levels of reduced GSH and the GSH/GSSG ratio that were significantly reduced in MCF7 spheres (Figure 5C, 5D). The level of ROS, assessed by 2′,7′-dichlorofluorescein diacetate (DCF-DA), hydroxyphenylfluorescein (HPF, detecting hydroxyl radical) and mitochondrial superoxide indicator (mitoSOX), was significantly higher in TICs (Figure 5E), as was mitochondrial potential measured by the tetramethylrhodamine, methyl ester (TMRM) staining (Figure 5F). Higher generation of ROS is possibly due to mitochondrial iron loading and higher labile iron pool inside the cells, supported by the fact that levels of reduced GSH and the GSH/GSSG ratio were significantly lower in TICs, pointing to higher oxidative stress. Since we detected low enzymatic activity ACO1, which is dependent on FeS clusters and inhibited by ROS [88, 89], we further examined cellular response to hypoxia, in particular the expression and activity of hypoxia inducible factors (HIFs) as these are also regulated by iron [90].

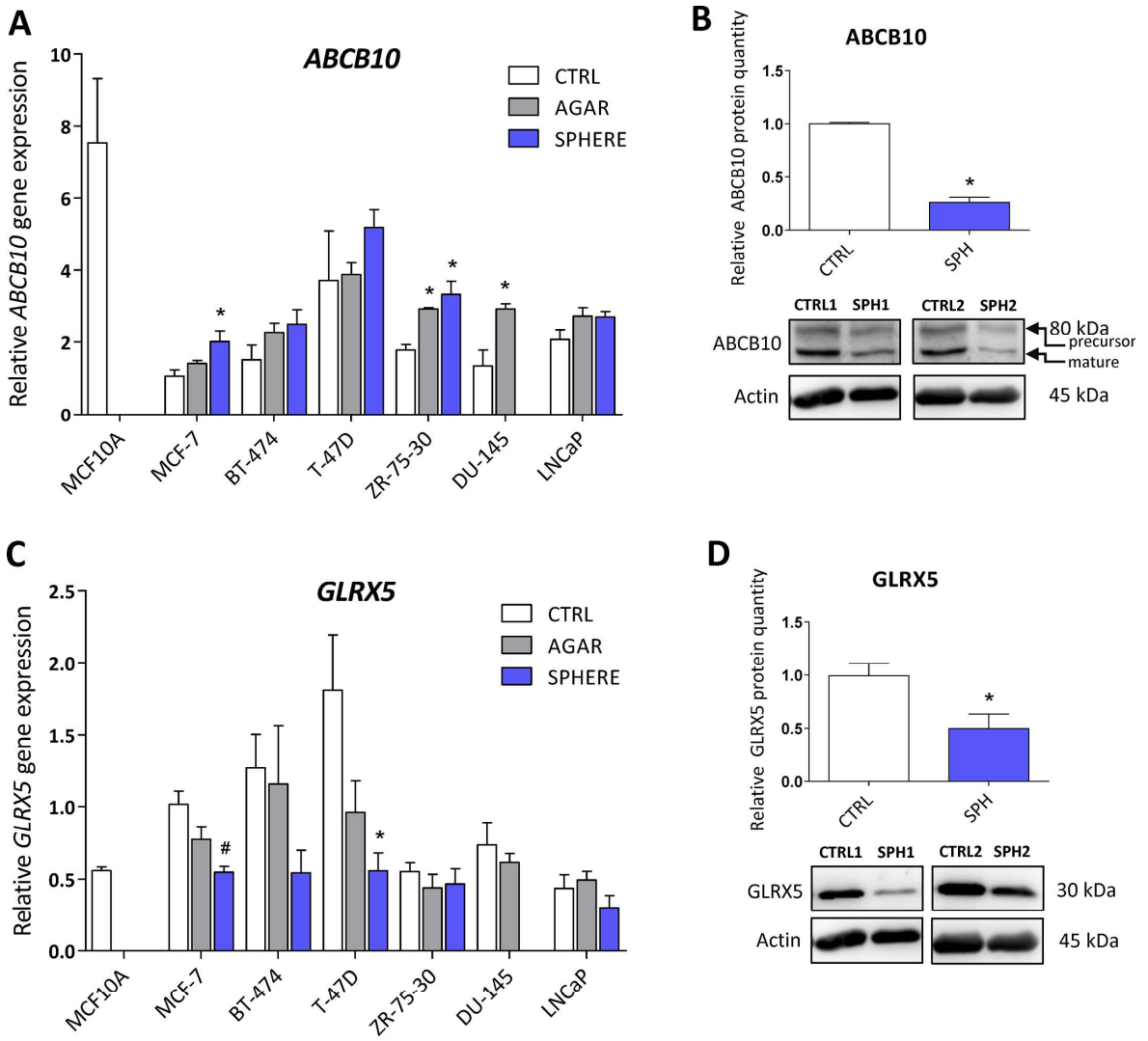

Figure 4: Protein levels of the ATP Binding Cassette Subfamily B Member 10 (ABCB10) and glutaredoxin 5 (GLRX5) participating in mitochondrial FeS cluster assembly are decreased in tumor-initiating cells (TICs). Expression of the *ABCB10* gene at the mRNA level in breast non-malignant cell line MCF10A, in TICs derived from breast cancer cell lines MCF-7, BT-474, T-47D and ZR-75-30 as well as from prostate cancer cell lines DU-145 and LNCaP has been determined (**A**) together with protein levels in the MCF-7 cell line (CTRL) and MCF-7 derived spheres (SPH) (**B**). Similarly, the expression of the *GLRX5* gene at the mRNA (**C**) level as well as protein level (**D**) in TICs is documented. Experiments were performed at least in triplicate, standard error is SEM, *p*-values lower than 0.05 are denoted with a star and were calculated by the GenEx software using the unpaired *t*-test and plotted with GraphPad prism software. Number sign denotes statistical significance involving Dun-Bonferroni correction. The protein expression was quantified by the image J software from 2 to 5 independent samples, standard error is SEM, *p*-values lower than 0.05 are denoted with a star and were calculated and plotted in GraphPad prism, using the unpaired *t*-test.

Expression of genes related to hypoxia (Endothelial Per-ARNT-Sim Domain Protein 1, *EPAS1*), cellular quiescence and extracellular matrix remodelling (Quiescin Sulfhydryl Oxidase 1, *QSOX1*) is elevated in TICs

HIFs are normally degraded by the action of prolyl hydroxylases and ubiquitinylation, resulting in proteasomal degradation. Prolyl hydroxylases require iron to carry out their action, and hypoxia inducible factor 2 (HIF2α) has been demonstrated as a direct target of ACO1 that does not contain FeS clusters and functions as an iron sensor, IRP1 [90]. Additionally, ROS have been also shown to stabilize HIF2α [91]. In accordance with higher IRP1 activity and higher ROS levels in TICs, our profiling data support the role of genes connected with hypoxic response in the phenotype of TICs, in particular the *EPAS1* gene coding for the HIF2α protein. This protein normally regulates

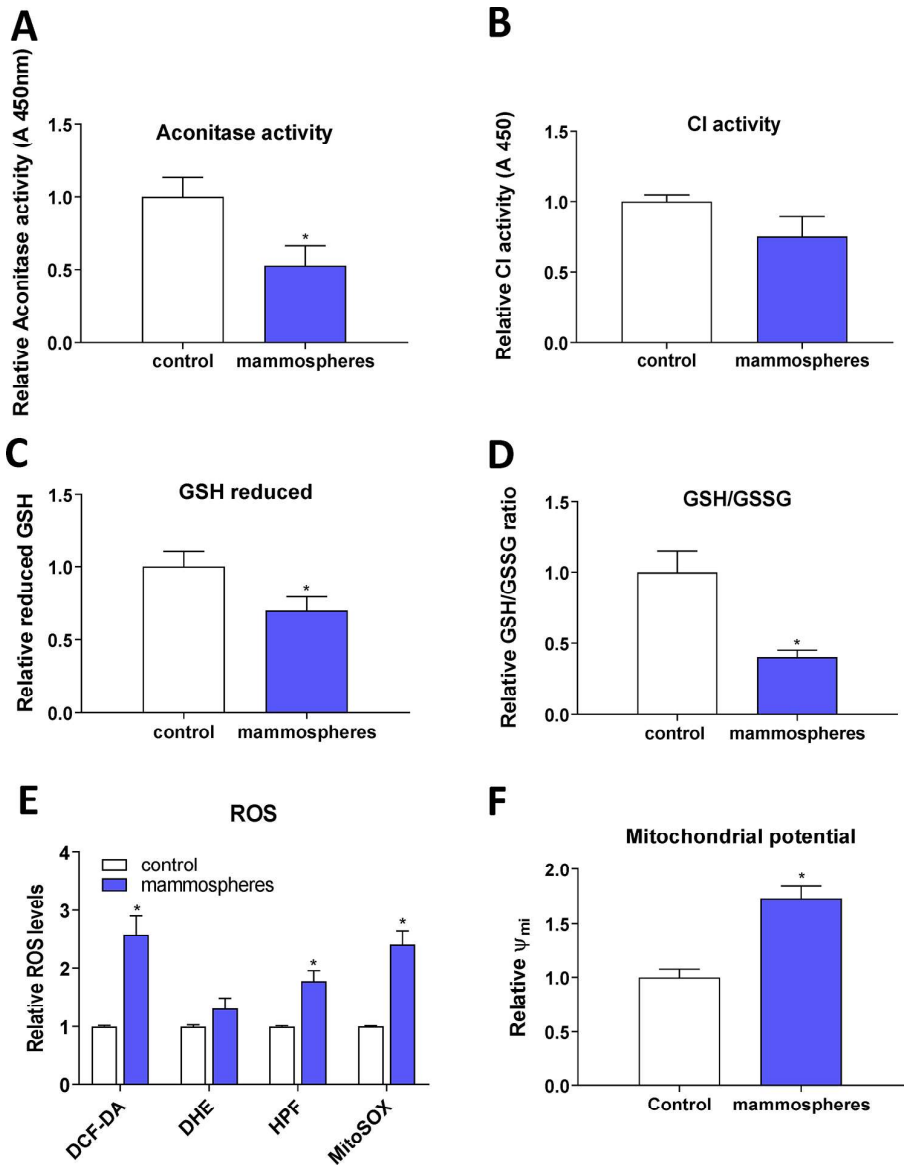

Figure 5: Reduced enzymatic activity of FeS cluster containing enzymes, reduced glutathione (GSH) content and increased reactive oxygen species (ROS) levels in tumor-initiating cells (TICs). Cell cultured under control conditions (control) or in sphere medium (mammospheres) were assessed for the enzymatic activity of aconitase (**A**) and mitochondrial respiratory complex I (**B**). Further tests also measured the reduced glutathione (GSH) (**C**) and the ratio of reduced/oxidized glutathione (GSH/GSSG) ratio (**D**). Spheres also show higher ROS production (**E**) measured by 2′,7′-dichlorofluorescein diacetate (DCF-DA), dihydroethidium (DHE), hydroxyphenylfluorescein (HPF) and mitochondrial superoxide indicator (mitoSOX). Spheres also show higher mitochondrial potential measured by tetramethylrhodamine methylester (TMRM) (**F**). Experiments were performed at least in triplicate, standard error is SEM, *p*-values lower than 0.05 are denoted with a star and were calculated by the GraphPad Prism software using the unpaired *t*-test.

the response of cells to hypoxia but has been also linked to the cancer stem cell phenotype [92]. The actual role of EPAS1 in carcinogenesis has been documented for paragangliomas, pheochromocytomas, bladder cancer, ovarian cancer, and a link to the oxidative phosphorylation and stem cell features has been suggested [24, 40, 93–100]. Interestingly, its expression at the mRNA level is upregulated in spheres derived from MCF7, BT-474, DU-145 and LNCaP spheres, although only DU-145 reached statistical significance (Figure 6A, Supplementary Table S1). These changes were then subsequently confirmed on protein level in MCF7 sphere model (Figure 6B). Thus, HIF2α could be responsible for metabolic adaptations of TICs and might also be responsible for the observed upregulation of several iron metabolism-related genes such as *CYBRD1 or QSOX1* [11, 12].

As pointed above, our analysis also revealed increase in the *QSOX1* expression. QSOX1 is a HIF target gene, connected to cellular quiescence and extracellular matrix remodelling [12]. Physiological role of this enzyme includes generation of disulphide bonds accompanied by generation of hydrogen peroxide and it contains the essential for respiratory and vegetative growth (ERV) domain homologous to the yeast Erv1p that is required for maturation of the cytosolic FeS clusters [101–105]. QSOX1 expression is induced in fibroblasts entering quiescence, and its role in cancer is beginning to appear [106] with reports stating that QSOX1 may be a specific marker for the luminal B subtype of breast cancer [107–109]. Its role has been suggested also for pancreatic and lung cancer, and for neuroblastoma [12, 110–112]. QSOX1 can also be involved in inhibition of autophagic flux in cancer cells [113]. Its role in remodelling of extracellular matrix, cell invasion and motility has also been described [114]. The *QSOX1* mRNA expression is reproducibly and significantly elevated in spheres derived from MCF7, BT-474, T-47D and also in LNCaP cells (Figure 6C, Supplementary Table S1). The increase in QSOX1 expression was confirmed on the protein level as well (Figure 6D). It is of interest that the highly induced isoform is the 66 kDa variant of this protein with a thus far elusive function. Given the fact that higher expression of QSOX1 may participate in extracellular matrix remodelling and in modulating the ratio between free SH groups and S-S bonds as well as being recognized as an HIF target, we can speculate that QSOX1 may be an important regulator of TICs maintenance and also their migration.

Iron export machinery-related hephaestin *(HEPH)* is elevated at the mRNA and protein level while the hemochromatosis gene (*HFE)* related to systemic iron loading is increased only at the mRNA level in TICs

We have also detected changes in the expression of the *HEPH* gene, coding for the multi copper oxidase hephaestin, which physiologically helps iron transport from enterocytes [14, 115–117]. Disruption of the *HEPH* gene results in hypochromic microcytic anemia and retinal iron overload [116, 118, 119]. In relation to cancer, HEPH expression was reduced in colorectal carcinoma and loss of HEPH was associated with more advanced disease [53]. In our sphere model of TICs, the expression of *HEPH* mRNA was significantly higher in BT-474 and T-47D breast cancer cells while other cell lines also showed increased expression but did not reach statistical significance (Figure 7A, Supplementary Table S1). The HEPH protein level showed a significant increase in HEPH protein isoform at 150 kDa, while the 100 kDa isoform is decreased in the MCF7 sphere model (Figure 7B). Thus, HEPH role in TICs is probably specific for a particular cell type and individual isoforms and their response to iron and involvement in carcinogenesis might differ.

Interestingly, the *HFE* gene coding for the hemochromatosis protein was also altered in TICs. This gene and its C282Y mutant form have long been connected to excessive iron loading in hemochromatic patients. The accumulation of iron caused by mutation in the *HFE* gene increases the risk of cancer development [53, 120–122]. Unexpectedly, we detected an increase in *HFE* mRNA level in TICs generated by the sphere approach in MCF7, BT-474, T-47D and DU-145 cells (Figure 7C, Supplementary Table S1). However, on the protein level, no changes were seen in MCF7 sphere model (Figure 7D). Thus, although there seems to be a significant upregulation of *HFE* mRNA, the lack of response on the protein levels rather suggests that the HFE protein is not linked to the TICs phenotype.

To gain further insight into iron metabolism of TICs, we have assessed the expression of additional important regulators of iron uptake, transfer, storage and export that are known to be regulated on the level of protein rather than on the level of transcription. Since these proteins are regulated on the protein levels they were not picked up by the expression profiling.

Protein levels of regulators related to iron transport (NRAMP2, Natural resistance associated macrophage protein 2*)* and iron storage (ferritin) are decreased while expresssion of proteins participating in non transferrin bound iron (NTBI) uptake (ZIP14, Zinc importer protein 14) and iron export (ferroportin) does not differ in TICs

First, we examined the expression of solute carrier family 11 member 2 (*SLC11A2*) coding for a protein known as NRAMP2 or DMT1 (Divalent metal transporter 1). NRAMP2 is known to transport iron from the gut lumen into enterocytes and also participates in the release of transferrin iron from the acidic environment of the lysosomes into cytosol, other studies also suggest

its role in the non-transferrin bound iron (NTBI) uptake [16, 123, 124]. Its role in carcinogenesis is not well described with possible role in colorectal and oesophageal cancer [54, 61, 125]. Interestingly, the level of *SLC11A2* mRNA containing a functional IRE motif (+IRE) measured by the gene profiling, did not dramatically change with exception of the DU-145 cell line; however, the non-IRE variant mRNA seemed significantly upregulated in most cell lines (Supplementary Figure S3A). Yet, NRAMP2 protein levels were significantly reduced in MCF7 sphere model (Figure 8A). This could be an explanation why there is paradoxically higher LIP while cells show activation of IRP/IRE system, since lack of NRAMP2 would leave the acquired iron locked in the lysosomes, unavailable to be incorporated into the active sites of enzymes and proteins.

Further, we analyzed levels of ferritin at mRNA and protein levels (encoded by *FTH* and *FTL*) as ferritin is a major iron storage protein that is capable of binding tremendous amount of iron, storing it and then releasing it when needed. Ferritin is encoded by *FTH1* responsible mainly for the ferroxidase activity and also *FTL1* which plays a role in iron nucleation and protein stability [5, 126]. Ferritin has been linked to progression of breast, ovarian, pancreatic and prostate cancer [28, 127–129]. In our data

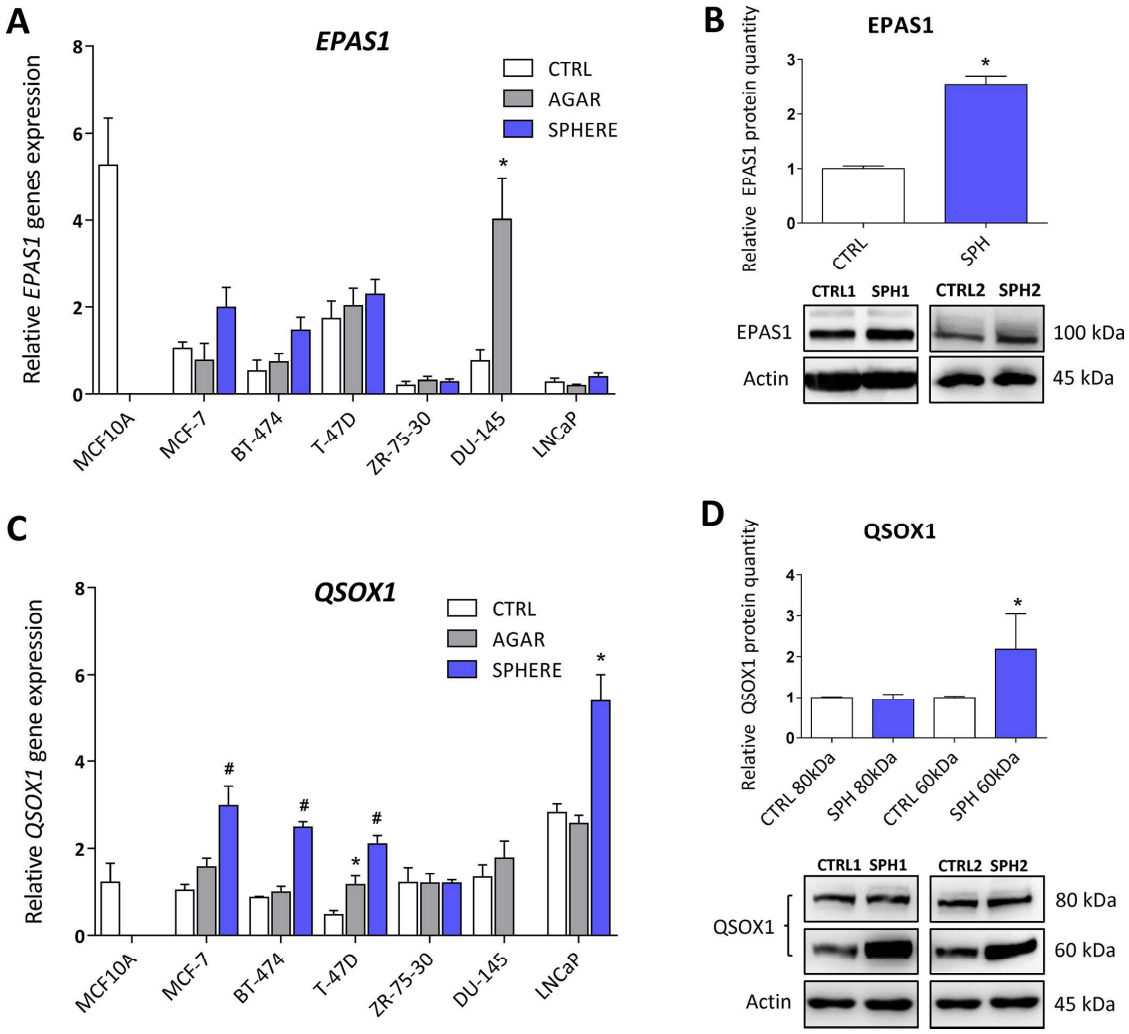

Figure 6: Expression of genes related to hypoxia (Endothelial PAS Domain Protein 1, *EPAS1*), cellular quiescence and extracellular matrix remodelling (Quiescin Sulfhydryl Oxidase 1, *QSOX1*) is elevated in tumor-initiating cells (TICs). Expression of the *EPAS1* gene at the mRNA level in breast non-malignant cell line MCF10A, in TICs derived from breast cancer cell lines MCF-7, BT-474, T-47D and ZR-75-30 as well as from prostate cancer cell lines DU-145 and LNCaP has been determined (**A**) together with protein levels in the MCF-7 cell line (CTRL) and MCF-7 derived spheres (SPH) (**B**). Similarly, the expression of the *QSOX1* gene at the mRNA (**C**) level as well as protein level (**D**) in TICs is documented. Experiments were performed at least in triplicate, standard error is SEM, *p*-values lower than 0.05 are denoted with a star and were calculated by the GenEx software using the unpaired *t*-test and plotted with GraphPad prism software. Number sign denotes statistical significance involving Dun-Bonferroni correction. The protein expression was quantified by the image J software from 2 to 5 independent samples, standard error is SEM, *p*-values lower than 0.05 are denoted with a star and were calculated and plotted in GraphPad prism, using the unpaired *t*-test.

set, there were almost no changes in *FTH* and a slight increase in *FTL* mRNA level only in MCF7 and BT-474 (Supplementary Figure S3B), while the protein levels were markedly reduced (Figure 8B). This is in agreement with the activation of the IRP/IRE system implicating that iron storage is reduced and provides another independent validation that the IRP/IRE system activity is increased. Also a reduction of the ferritin levels is in line with a current study suggesting that FTH is a negative regulator of ovarian stem cell expansion [129]

We also analysed expression of an important player in the non-transferrin bound iron (NTBI), the ZIP14 protein encoded by the *SLC39A14* gene which has been shown to transport iron [18, 19, 130]. Its role in carcinogenesis is so far unclear with possible role in hepatocellular cancer [131, 132] Interestingly, on the mRNA level we were able to detect an upregulation in most cell lines tested (Supplementary Figure S3C), yet, on the protein level, we did not detect any significant change in by the MCF7 sphere model (Figure 8C) suggesting

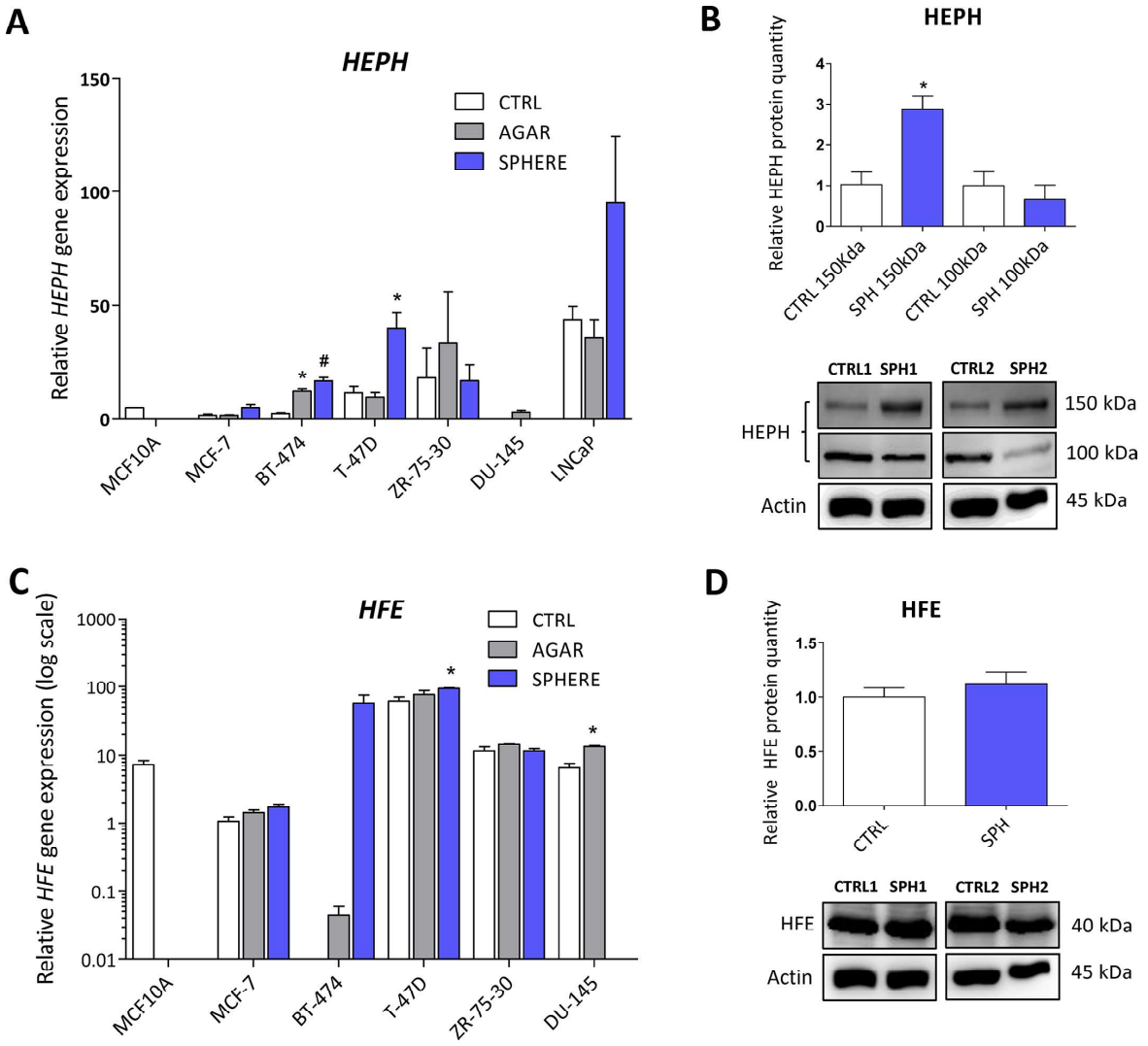

Figure 7: Iron export machinery-related hephaestin (*HEPH*) and the hemochromatosis gene (*HFE)* related to systemic iron loading are elevated at the mRNA level but not on the protein level in tumor-initiating cells (TICs). Expression of the *HEPH* gene at the mRNA level in breast non-malignant cell line MCF10A, in TICs derived from breast cancer cell lines MCF-7, BT-474, T-47D and ZR-75-30 as well as from prostate cancer cell lines DU-145 and LNCaP has been determined (**A**) together with protein levels in the MCF-7 cell line (CTRL) and MCF-7 derived spheres (SPH) (**B**). Similarly, the expression of the *HFE* gene at the mRNA (**C**) level as well as protein level (**D**) in TICs is documented. Experiments were performed at least in triplicate, standard error is SEM, *p*-values lower than 0.05 are denoted with a star and were calculated by the GenEx software using the unpaired *t*-test and plotted with GraphPad prism software. Number sign denotes statistical significance involving Dun-Bonferroni correction. The protein expression was quantified by the image J software from 2 to 5 independent samples, standard error is SEM, *p*-values lower than 0.05 are denoted with a star and were calculated and plotted in GraphPad prism, using the unpaired *t*-test.

that the detected 52 kDa form of ZIP14 is probably not participating in higher iron uptake in TICs.

Additionally, we have examined the expression of the solely know iron exporter, ferroportin, (FPN) encoded by the *SLC40A1* gene [15, 67, 133, 134]. A report connecting lower expression of ferroportin to iron accumulation and cancer progression exists but other research on this topic remain scarce [49]. Our data documented no significant change in the mRNA level in most of the cell lines tested with exception of BT-474 and T-47D where it was increased (Supplementary Figure S3D). However, western blot analysis of its protein level did not show any significant change in MCF7 sphere model (Figure 8D). This suggests that a change in iron export is not the underlying cause of higher LIP in TICs and the observed changes are rather related to iron uptake and may reflect higher level of improperly assembled FeS clusters.

Expression profiling and protein analysis of the tamoxifen resistant (TAMR) MCF7 cells representing an alternative model of TICs

To further validate our findings on another *in vitro* model, we used the tamoxifen resistant MCF7 cells (TAMR) that exhibit features of stem cells (Supplementary Figure S5A) in agreement with published literature [135–137].

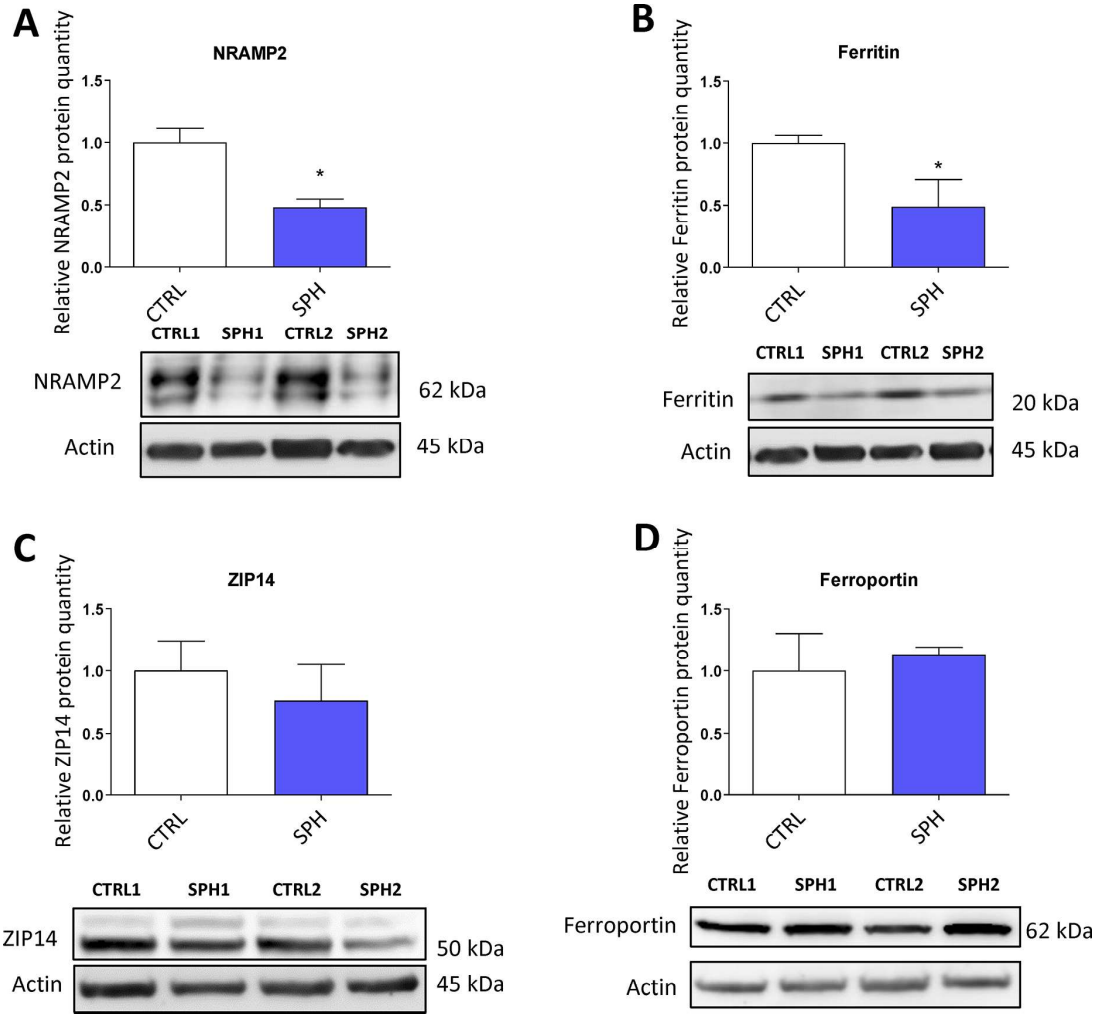

Figure 8: Protein levels of regulators related to iron transport (NRAMP2, Natural resistance associated macrophage protein 2) and iron storage (ferritin) are decreased while expression of proteins participating in non transferrin bound iron (NTBI) uptake (ZIP14, Zinc importer protein 14) and iron export (ferroportin) does not differ in tumor-initiating cells (TICs). Protein levels of NRAMP2 (**A**), ferritin (**B**), zinc transporter protein 14 (**C**) and ferroportin (**D**) in the MCF-7 cell line (CTRL) and MCF-7 derived spheres (SPH) are shown. The protein expression was quantified by the image J software from 2 to 5 independent samples, standard error is SEM, *p*-values lower than 0.05 are denoted with a star and were calculated and plotted in GraphPad prism, using the unpaired *t*-test.

These cells mostly recapitulated findings seen in TICs represented by the MCF7 spheres. They show higher levels of LIP, higher ROS, reduced GSH (data not shown) and identical regulation of ABCB10, ACO1, GLRX5, EPAS1, 100kDa isoform of HEPH, IREB2, SLC39A14, SLC40A1 and QSOX1 with statistically significant changes on the mRNA and protein level (Supplementary Figure S5B, Supplementary Figure S6) pointing to high similarity in terms of iron gene signature. Yet, we have detected different regulation in protein levels of 150 kDa isoform of HEPH, TFRC, Ferritin and SLC11A2 (Supplementary Figure S6). These differences might be related to the presence of tamoxifen, an agent that is known to generate ROS, resulting in adaptation to permanent oxidative stress. One of the possible mechanism might be upregulation of ferritin which is able to inactivate free iron by its ferroxidase activity [138].

Furthermore, unlike MCF7 spheres, TAMR cells show higher SLC11A2 (DMT1) levels and no change in TFR1 levels. Yet, it might just be a different mechanism how to acquire iron, which seem to be more dependent on TFR1 in spheres, while TAMR cells probably use more of the non-transferrin bound iron *via* the SLC11A2, both converging on higher iron uptake as suggested by Miller et al [49]. Thus, the alternative model of TAMR cells confirmed majority of changes seen in the model of MCF7 spheres and supports the importance of iron in the biology of TICs.

Analysis of the iron metabolism-related genes in leukemia-initiating cells (LICs) from leukemic mice *in vivo*

To further expand our findings from an *in vitro* conditions to an *in vivo* conditions, we used a murine model of acute promyelocytic leukemia (APL) that allows for identification and isolation of LICs, based on the depletion cocktail-, c-kit+, and CD34+ expression profile. Non-LICs from leukemic mice were characterized by depletion cocktail-, c-kit-, and CD34- expression profile and the expression of lactoferrin (Ltf) that is highly induced in the differentiated cells [139]. Unfortunately, we were not able to determine expression on the level of protein since the number of cells that are obtained after sorting is very low for some sorted populations and western blot of several proteins is technically unfeasible.

We detected statistically significant upregulation of *Glrx5* and *Tfrc* mRNA between leukemic CD34-/c-kit- (non-LICs) and CD34+/c-kit+ (LICs) populations as well as significant differences in the expression of *Cybrd1* and *Qsox1* between CD34+/c-kit+ (LICs) populations of normal and leukemic mice (Supplementary Figure S2A, Supplementary Table S2). Furthermore, expression of *Aco1, Epas1, Glrx5, Hfe, Ireb2 and Tfrc* mRNA was significantly altered between the CD34-/c-kit- (non-LICs) populations of normal and leukemic cells (Supplementary Figure S2A, Supplementary Table S2). Comparing the sorted CD34+/c-kit+(LICs) population to whole bone marrow, we could see a similar picture, which is statistically significant upregulation in *Epas1* and *Glrx5* and changes in the *Abcb10* and *Qsox1* expression that were very close to significance (Supplementary Figure S2B, Supplementary Table S2). Thus, we did see significant changes in expression of iron metabolism-related genes supporting the evidence that iron uptake in these cells is higher and their FeS cluster metabolism and hypoxia related genes show higher expression.

Principal component analysis (PCA) based on the expression of selected iron-metabolism related genes is able to distinguish tumor-initiating cells (TICs) *in vitro* and leukemia-initiating cells (LICs) in the acute promyelocytic leukemia (APL) mouse model

In order to define whether the expression of the identified differential iron metabolism-related gene signature is able to distinguish TICs from non-TICs, we performed the PCA analysis based on the expression of gene signature identified by the expression profiling consisting of *Aco1, Abcb10, Cybrd1, Epas1, Glrx5, Heph, Hfe, Ireb2, Qsox1, Tfrc* genes. The PCA clearly documents that sphere samples are clustered separately from the control adherent cancer cells in all of the tested cell lines (Figure 9). This is further documented for the TAMR cells as well (Figure 9). Furthermore, the PCA analysis with similar gene set (excluding Heph), applied on an *in vivo* APL mouse model of leukemia-initiating cells is also able to easily distinguish the population using similar gene set with exclusion of *Heph* is also able to easily distinguish the population of LICs (CD34+/c-kit+) from non-LICs (CD34-/c-kit-), thus replicating our findings in cell lines (Supplementary Figure S4). Thus, Thus, although we obtained we obtained our iron metabolism related gene signature in breast cancer TICs, and we applied it to a leukemia cells, we were clearly able to distinguish the LICs from non-LICs as well.

Summary

In this report, we examined the role of iron in the biology of TICs. We show that TICs exhibit marked alterations in the iron metabolism and handling and also show differential gene expression of the iron metabolism-related genes, thus pointing to the importance of iron in the biology of TICs.

To gain a more detailed knowledge about the iron metabolism in TICs, we assessed many aspects related to iron metabolism. We show that TICs contain higher labile iron pool (LIP), in other words these cells contain more loosely bound iron. Free iron is known to generate ROS via the Fenton and Haber-Weiss reactions. Thus,

in agreement with higher LIP in TICs, we detected higher level of hydroxyl radicals and also higher level of mitochondrial superoxide, in line with the observed accumulation of iron in mitochondria.

Since oxidative stress and labile iron pool are known to regulate the function of the iron responsive proteins (IRPs), we assessed their expression and function. Our data show that especially IRP1 known also as ACO1 is activated and binds to its cognate element, IRE. This results in higher iron uptake via TFRC and CYBRD1 and lower levels of ferritin, the major intracellular iron storage protein. As ACO1 requires FeS clusters for its enzymatic function and its IRP1 function is connected with the absence of FeS clusters, we looked into the expression of the FeS cluster assembly components. Our data clearly show that there is low expression of ABCB10 and GLRX5 proteins, both of which are located in mitochondria. Together with low amount of GSH which is required for normal FeS cluster biosynthesis, our data suggest that FeS cluster assembly is inefficient in TICs, resulting in an increase of IRP1 activity of ACO1 and possibly leading to iron accumulation in mitochondria due to low ABCB10 levels. This is further supported by lower enzymatic activity of proteins requiring FeS clusters for their catalytic activity such as mitochondrial respiratory complex I and the above mentioned ACO1. Furthermore, low levels of properly assembled FeS clusters may also underlie higher sensitivity of TICs to iron withdrawal that was observed and predispose them for genetic instability and very high plasticity.

Interestingly, ACO1 that does not contain FeS clusters shows high IRP1 activity and stabilizes the *EPAS1* mRNA coding for the HIF2α [90]. In addition, protein stability of HIF2α is enhanced by ROS [91]. In agreement with this, we have detected higher levels of HIF2α in TICs, possibly connecting it with activation of HIF targets (DCYTB1, QSOX1). The activation of QSOX1 which is connected with extracellular remodelling and cellular quiescence might be an important step regulating cellular migration and invasion. All the above mentioned changes are depicted in summarizing Figure 10.

Other iron metabolism related proteins participating in iron export (HEPH, ferroportin), iron trafficking and non-transferrin-bound iron (NRAMP2, ZIP14) and iron

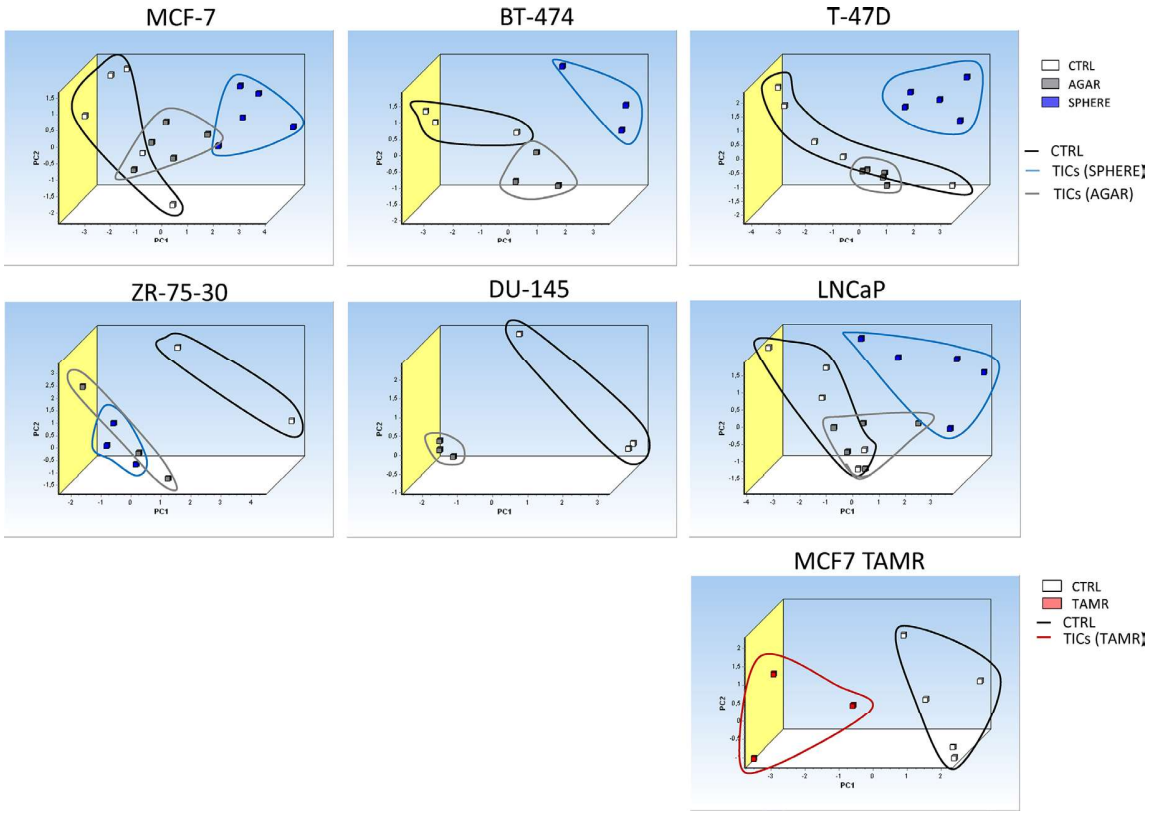

Figure 9: Principal component analysis (PCA) discriminates tumor-initiating cells (TICs) from cancer cells based on gene expression of the selected iron metabolism-related genes (*Aco1*, *Abcb10*, *Cybrd1*, *Epas1*, *Glrx5*, *Heph*, *Hfe*, *Ireb2*, *Qsox1* and *Tfrc*). Principal component analysis (PCA) based on selected iron metabolism-related genes was run on malignant breast MCF-7, BT-474, T-47D, ZR-75-30 and malignant prostate DU-145 as well as LNCaP cell lines using the GenEx software which was also used for plotting the PCA. White squares depict control conditions, grey show agar conditions, blue boxes show sphere conditions and red boxes show TAMR cells. Individual clusters were also highlighted with corresponding lines using identical colors.

storage (ferritin) were examined. We detected higher levels of the *HEPH* mRNA and higher levels of HEPH 150Kda variant, no changes in ferroportin and ZIP14 while there is a clear downregulation of ferritin and NRAMP2. Thus, in agreement with the activation of the IRP/IRE system, ferritin level is suppressed and the involvement of NRAMP2 and ZIP14 in the acquisition of iron in TICs is unlikely.

Lastly, our work identified a specific iron metabolism-related gene signature differentially expressed in TICs (*ABCB10, ACO1, CYBRD1, EPAS1, GLRX5, HEPH, HFE, IREB2, QSOX1* and *TFRC)*. The principal component analysis based on this signature is able to distinguish not only TICs *in vitro* (TICs growing as spheres and also TICs represented by the tamoxifen resistant MCF7 cells) but also LICs *in vivo*, thus confirming the importance of iron metabolism in their phenotype. Further research focusing on the role of the differentially expressed iron metabolism-related proteins in TICs biology and cancer resistance is warranted and may be of clinical importance. Studies examining the role of combination therapy using anti TICs drugs in combination with iron chelators might pave the path to a novel treatments in the future.

MATERIALS AND METHODS

Tissue culture and sphere generation

Cells were routinely cultivated in Dulbecco's Modified Eagle Medium (DMEM) (BT-474, DU-145, MCF7, T-47D, ZR-75–30 cells) or Roswell Park Memorial Institute medium (RPMI1640) (LNCaP cells) supplemented with 10% fetal bovine serum (FBS), 10 mM 4-(2-hydroxyethyl)-1-piperazineethanesulfonic acid (HEPES) and 2 mM glutamine. MCF-10A cells were cultivated in DMEM/F12 with 5% horse serum and antibiotics, supplemented with 0.1 ng/ml cholera toxin, 20 ng/ml epidermal growth factor (EGF), 0.5 µg/ml hydrocortisone, 1 mg/ml insulin. All cells were obtained either directly from ATCC or from prof. Lopez (Griffith University, Australia). For the generation of spheres, advanced DMEM/F12 or RPMI1640 medium supplemented with 5% of proliferation supplement, 20 ng/

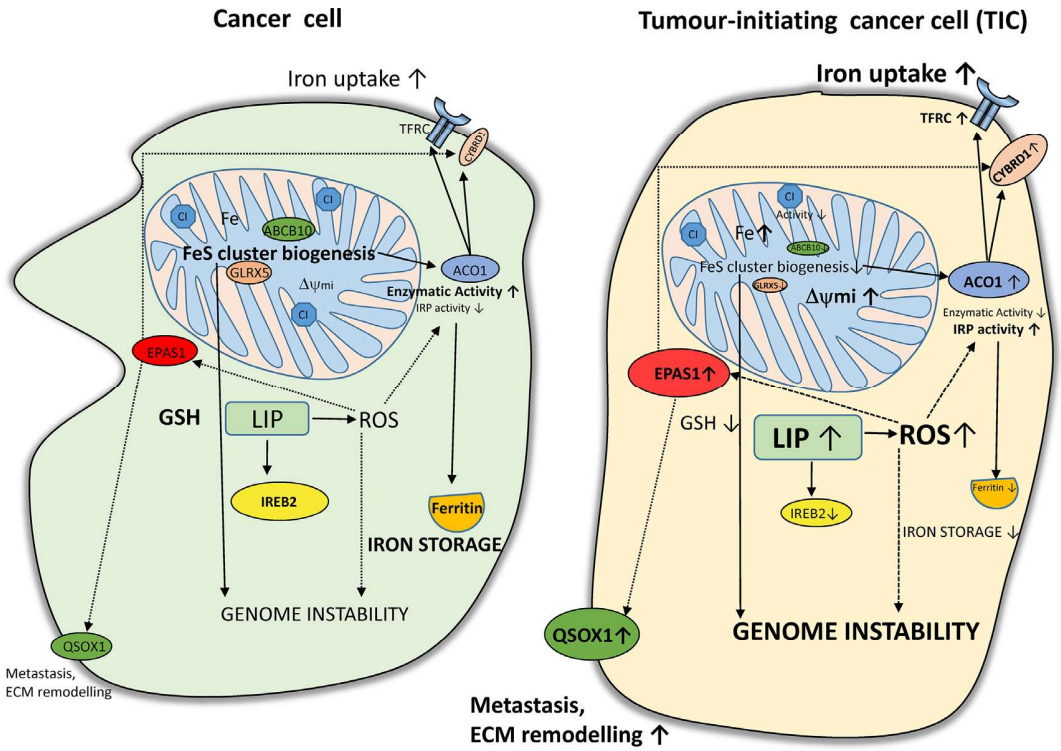

Figure 10: Putative scheme depicting changes in iron metabolism of tumor-initiating cells (TICs). TICs show higher levels of labile iron pool (LIP) and subsequently higher reactive oxygen species (ROS) which in connection with lower Fes cluster biogenesis (lower expression of ABCB10 and GLRX5) leading to accumulation of iron in mitochondria and possibly affecting genome stability and increasing plasticity of these cells. Alterations in the FeS cluster assembly lead to reduced activity of ACO1/IRP1 as well as mitochondrial respiratory complex I. The IRP binding activity of ACO1 is elevated resulting in higher TFRC and lower ferritin levels. Furthermore, TICs show an increase in the protein level of of EPAS1/ HIF2A connected with higher iron uptake (CYBRD1, TFRC) as well as with the extracellular matrix remodelling and redox balance equilibrium *via* the expression of QSOX1. On the other hand, reduced glutathione (GSH) is lower in TICs and these cells seem to be in a more pro-oxidative state and contain lower protein levels of IREB2/IRP2 likely reflecting increased LIP.

ml EGF, 5 ng/ml fibroblast growth factor (FGF), 4 µg/ml heparin, 10 mM HEPES, 1 mM glutamine and penicillin/streptomycin antibiotics was used. Control medium contained 5% FBS instead of proliferation supplement and was supplemented with 1 mM glutamine, 10 mM HEPES and penicillin/streptomycin. Cells generated by the agar approach were cultivated in normal serum containing medium but on a plastic ware coated with 1% agarose.

RNA isolation and quality determination

RNA was isolated by the method using RNAzol RT according to manufacturer's instructions. Briefly, cells were collected, spun and lysed in 500 µl of RNAzol. The lysate was then mixed with 200 µl of RNAse-free water, vortexed and incubated for 10 min at room temperature (RT), and spun at 12,500 × g for 15 min. The supernatant was then mixed with 4-bromoanisole, incubated for 10 min and spun at 12,500 × g for 10 min. The supernatant was next precipitated with equal volume of isopropanol, spun at 4ºC at 14,000 × g for 15 min, washed twice with 80% ethanol, dried and dissolved in RNAse free water (20 µl). RNA quantity was measured with the Nanodrop spectrophotometer (ND-1000, Thermo Scientific), and each RNA integrity was measured with the Agilent 2100 Bionalyser (Agilent Technologies).

cDNA synthesis and sample preparation for the Fluidigm qPCR

RNA quality of the used samples was determined by the RNA integrity number score (RIN between 8–10), and cDNA was reverse-transcribed by the Maxima H minus reverse transcriptase kit (Thermo Scientific) using 400 ng total RNA as a template and oligo-dT as primers, according to manufacturer's instructions.

Fluidigm qPCR

Primer design was performed with Primer BLAST. All assays were designed to span at least one intron and/or to have one primer covering an exon/exon boundary. Each sample was pre-amplified with mix of all primer pairs for 18 cycles. The reaction contained 5 µl of iQ Supermix (Bio-Rad), 2 µl of diluted cDNA, 1.25 µl of pre-amplification primer mix in final concentration 25 nM and 1.25 µl of water. Temperature profile was 95°C for 60 s and 18 cycles of 95°C for 15 s and 4 min at 60°C. qPCR was performed using the high-throughput platform BioMark HD System (Fluidigm) with 96.96 Dynamic ArrayIFC for gene expression. 5 µL of sample pre-mix contained 1 µl of 20x diluted preamplified cDNA, 2.5 µl of SsoFast EvaGreen Supermix (Bio-Rad), 0.25 µl of 20x SG sample loading reagent (Fluidigm) and 1.25 µl of water. Five µl of assay pre-mix contained 2 µl of 10 µM primer/probe assays, 2.5 µl of 2× assay loading reagent (Fluidigm) and 0.5 µl of water. Thermal conditions for qPCR were: 98°C for 3 min, 35 cycles of 98°C for 5 s and 60°C for 5 s. Raw data were subtracted from the gDNA control and efficiencies of individual assays were calculated from the serial dilutions of a mixed cDNA sample. Assays with insufficient efficacy or very high Cq values (> 25) were excluded from the analysis. The actual analysis was done via the GenEx software version 6, and the missing values were replaced by the mean of average value calculated from the whole group. Reference genes for normalization were identified by Normfinder; data were normalized to several reference genes *(GAPDH*, *POLR2A*, *RPLP0*, *HPRT1* and *TBP)*. The data were assessed for statistical analysis by using the unpaired *t*-test via GenEx, with the *p*-value < 0.05 was considered statistically significant and results with the Dun-Bonferroni correction are presented as well.

Western blot analysis

Protein expression was assessed by a standard western blot assay. Briefly, cells were washed with phosphate-buffered saline (PBS) and lysed directly on a Petri dish in 1x cell lysis buffer supplemented with protease and phosphatase inhibitors. Protein concentration was measured via the bicinchinonic acid (BCA) method, and 50–80 µg of total protein was loaded in each well of the SDS-PAGE gel. Gels were then separated according to standard procedure at 20 mA per well, washed in 1× towbin buffer and blotted onto a nitrocellulose membrane via Xcell blotting module (Invitrogen) at constant voltage (35 V) for 2 h. Membranes were then blocked with 5% non-fat milk for 1 h, washed and incubated in 5% bovine serum albumin (BSA)/Tris-buffered saline (TBS)/0,1% Tween-20 with primary antibodies against ABCB10 (ThermoScientific #PA5-30468, dil. 1:1000), ACO1 (ThermoScientific #PA5-27824, dil. 1:1000), CYBRD1 (Bioss #bs-8297R, dil. 1:1000), EPAS1 (ThermoScientific #PA116510, dil. 1:1000), GLRX5 (Bioss #bs-13395R, dil. 1:1000), HEPH (Bioss #bs-15458R, dil. 1:1000), HFE (Bioss #bs-12335R, dil. 1:1000), IREB2 (ThermoScientific #PA116544, 1:500), QSOX1 (Sigma #SAB2700031, dil. 1:1000), TFRC (ThermoScientific #13-6800, dil. 1:2500), SLC39A14 (Abcam #ab191199, dil. 1:2000), SLC40A1 (Bioss #bs-4906R, dil. 1:1000) SLC11A2 (Cell Signalling #15083, dil. 1:1000), Ferritin (Abcam #ab75973, dil. 1:1000), Actin (Thermoscientific #MA5-15739-HRP, dil. 1:2000), Tubulin (Abcam #ab4742, dil. 1:5000) overnight. Membranes were then washed three times with 1 × TBS/0.1% Tween-20, incubated with corresponding horseradish peroxidase (HRP) - conjugated antibody in 1% milk 1 × TBS/0.1% Tween-20 for 1 h. Then the membranes were again washed three times with 1 × TBS/0.1% Tween-20 and incubated with either Clarity ECL (Biorad) or Sirius ECL substrate

(Advansta), and luminescence was assessed with LAS4000.

Labile iron pool (LIP) measurement

A method based on calcein dequenching has been used [52]. Briefly, cells were incubated with 250 nM calcein acetoxymethylester-(calcein-AM) for 30 min in medium supplemented with 1% BSA but without serum and sodium bicarbonate. Samples were then washed twice with Hanks Balanced Salt Solution (HBSS). 10,000 cells were added to each well of a 96-well plate, and fluorescence measurement started at the excitation wavelength of 468 nm, emission wavelength of 517 nm, after initial 5 min measurement. 100 µM salicylaldehyde isonicotinoyl hydrazone (SIH) was added and the fluorescence was recorded after 2 min.

^{55}Fe uptake measurement

Cells were dissociated by using the cell dissociating buffer (1% BSA, 1 mM EDTA, 1 mM EGTA), washed twice with the reaction buffer (50 mM HEPES (pH 7.4), 94 mM NaCl, 7.4 mM KCl, 0.74 mM $MgCl_2$, 5 mM D-Glucose) and divided into Eppendorf tubes to contain 1 million of cells per sample with total volume of 200 µl. 1 µl containing 1 µCi of ^{55}Fe in complex with citrate (1:10) was added. Cells were then incubated at 37ºC for 90 minutes with occasional mixing and after the incubation, samples were cooled on ice. Background binding was determined by addition of 1 µCi of ^{55}Fe to the cells followed by immediate cooling. Samples were then washed 5x with the reaction buffer, re-suspended in 100 µl of water and added to 5 ml of scintillation fluid. Samples were then measured on a scintillation counter and background corrected. Relative uptake was then calculated by comparing MCF7 spheres vs. control cells.

^{55}Fe subcellular localization

Cells were incubated with 50 nM ^{55}Fe complexed with citrate (1:10) for 72 hrs. Cells were then centrifuged and washed with 1x reaction buffer used in iron uptake experiments (50 mM HEPES (pH 7.4), 94 mM NaCl, 7.4 mM KCl, 0.74 mM $MgCl_2$, 5 mM D-Glucose). Cells were counted and diluted with STE buffer (250 mM sucrose, 10 mM TRIS, 1 mM EDTA) to a concentration of 4 milion cells per 1ml STE. Cells were then disrupted as shown by Schmitt et al. to retain functional mitochondria [140]. Cellular homogenate was then spun at 800 × g for 5 minutes to collect nuclei then spun at 3000 × g for 5 minutes and resulting supernatant was spun at 9,000 × g for 10 minutes to gain mitochondrial fraction. Protein content in each faction was determined by the BCA-based assay and 20 µg of proteins was then measured on a scintillation counter and background corrected.

Cellular viability assays (Cell Titer-Glo, Cell Titer-Fluor)

Cell viability assays were performed according to manufacturer's instructions (Promega, G7570 and G6080). Briefly, cells for the Cell Titer-Glow assay were seeded at of 5,000 cells per well into white luminescence plates, and after incubation with SIH, the Cell Titer-Glow reagent equal to the volume of medium was added and luminescence was captured using the TECAN 200 PRO reader. For the Cell Titer-Fluor assay, cells were seeded similarly but into a black fluorescent 96 well plates. After incubation with SIH, cells were incubated with fluorogenic peptideglycylphenylalanyl-aminofluorocoumarin and its fluorescence recorded at the excitation wavelength of 400 nm and emission wavelength of 505 nm using using Tecan infinity 200 PRO.

Aconitase activity measurement

The Sigma aconitase activity assay (MAK051) was used. Absorbance was assessed at 450 nm according to manufacturer's instruction using Tecan infinity 200 PRO. The obtained values were corrected for the background activity of lysates without substrate and normalized to protein content assessed by the BCA method. Relative values compared to control cells were then plotted *via* Graphpad prism.

Assessment of the IRE/IRP system activity via fluorescent EMSA

Cells were collected by centrifugation at 300 × g, 5 minutes, washed once with PBS a lysed in buffer containing 10 mM HEPES (pH 7.4), 3 mM $MgCl_2$, 40 mM KCl, 1 mM DTT and 0.2% NP-40. Proteins were then quantified by the BCA method and 60 µg of protein lysate was then incubated with 4 µM of the Cy5 labeled IRE probe containing the 1× IRE sequence from the human FTH gene (Cy5-UCGUCGGGGUUUCCUGCUUCAACAGUGCUUGG-ACGGAACCGGCGCU) in 24 mM HEPES, 60 mM KCl, 5% Glycerol, 0.004 U/µl RNAsin, plus or minus 2% β-ME in a total volume of 20 µl for 20 minutes, then 2 µl of heparin [141, 142] was added and incubated for another 10 minutes. Consequently, 2.4 µl of 10× loading dye was added and the reaction mixture was loaded onto 3–20% AA gel in 1 × TBE. Electrophoresis was then run at 70 V for 30 minutes, followed by 120 V until the blue dye reached the bottom of the gel. The gel was then visualized by the Typhoon instrument.

Mitochondrial respiratory complex I activity

Abcam mitochondrial respiratory complex I (CI) activity assay (ab109721) was used, utilizing immuno-capture

of CI and then colorimetric reaction measuring its activity *via* absorbance increase at 450 nm according to manufacturer's instructions. Relative values compared to control cells were then plotted *via* Graphpad prism.

Reduced glutathione (GSH) and reduced/oxidized glutathione (GSH/GSSG) ratio measurement

A fluorescence-based kit for determination of GSH and GSH/GSSG ratio was used according to manufacturer's instructions (BioVision). Briefly, cells were spun, washed with PBS and lysed in cell lysis buffer. 1 μg of total protein was loaded into 25 microliters of assay buffer in a 384-well plate. 25 microliters of the glutathione assay mixture (GAM) or total glutathione assay mixture (TGAM) mixture was added to samples, and reduced or oxidized glutathione standard curves plotted. Fluorescence was measured at the excitation wavelength of 480 nm and emission wavelength at 520 nm using Tecan infinity 200 PRO.

Assessment of mitochondrial membrane potential (ΔΨmi) and reactive oxygen species (ROS)

To assess ROS or ΔΨmi, spheres and control cells were dissociated by cell dissociation buffer to obtain single cell suspension and incubated with fluorescent probes for 15 min. ΔΨmi was assessed with 50 nM tetramethylrhodamine methyl ester (TMRM), and ROS were evaluated using 5 μM dichlorofluorescein diacetate (DCF-DA), 2.5 μM dihydroethidium (DHE), 5 μM hydroxyphenyl fluorescein (HPF) or 2.5 μM MitoSOX. After incubation, cells were spun down and resuspended in PBS. Fluorescence was measured by flow cytometer (BD FACS Calibur) and expressed as a mean fluorescence intensity. Data were normalized to control cells and plotted *via* Graphpad Prism.

Preparation of an acute promyelocytic leukemia (APL) *in vivo* model and isolation of LICs

An *in vivo* model of murine APL was prepared as previously described [139]. Briefly, leukemic spleen cells from hMRP8 PML-RAR transgenic mice were transplanted by retro-orbital injection into sub-lethally irradiated 12 week old FVB/N mice. Spleen cells from either leukemic or wild-type control mice were sorted using an Influx cell sorter based on expression of the following cell surface markers: *Sca*1 (clone D7; Biolegend), CD45/B220 (RA3-6B2; Biolegend), CD19 (MB19-1; Biolegend), CD3 (145-2C11, Biolegend) antigens, all pacific blue conjugated (omitting Gr1 antibodies from the usual depletion cocktail). The depletion cocktail-negative cells were then separated using antibodies against c-kit conjugated with allophycocyanin (clone 2B8; Biolegend) and CD34 conjugated with fluorescein isothiocyanate (RAM34; eBioscience). LICs from leukemic mice were characterized by depletion cocktail-, c-kit+, and CD34+ expression. Non-LICs from leukemic mice mice were characterized by depletion cocktail-, c-kit-, and CD34- expression. Counterpart non-leukemic populations were isolated from wild-type control mice.

CONFLICTS OF INTEREST

No competing financial interests exist

GRANT SUPPORT

This work has been supported by the GACR grant no. 13–28830S and the Kellner Family Foundation to J.T., and GACR grant no. 15–03796S to M. A-J, as well as by the by the Ministry of Education, Youth and Sports of CR within the LQ1604 National Sustainability Program II (Project BIOCEV-FAR) and by the project BIOCEV (CZ.1.05/1.1.00/02.0109).

REFERENCES

1. Paul VD, Lill R. Biogenesis of cytosolic and nuclear iron-sulfur proteins and their role in genome stability. Biochim Biophys Acta. 2015; 1853:1528–1539.
2. Sheftel AD, Mason AB, Ponka P.The long history of iron in the Universe and in health and disease. Biochim Biophys Acta. 2012; 1820:161–187.
3. Hentze MW, Muckenthaler MU, Andrews NC. Balancing acts; molecular control of mammalian iron metabolism. Cell. 2004; 117:285–297.
4. McKie AT, Barrow D, Latunde-Dada GO, Rolfs A, Sager G, Mudaly E, Mudaly M, Richardson C, Barlow D, Bomford A, Peters TJ, Raja KB, Shirali S et al. An iron-regulated ferric reductase associated with the absorption of dietary iron. Science. 2001; 291:1755–1759.
5. Torti FM, Torti SV. Regulation of ferritin genes and protein. Blood. 2002; 99:3505–3516.
6. Rouault TA, Tong WH. Iron-sulfur cluster biogenesis and human disease. Trends Genet. 2008; 24:398–407.
7. Ye H, Jeong SY, Ghosh MC, Kovtunovych G, Silvestri L, Ortillo D, Uchida N, Tisdale J, Camaschella C, Rouault TA. Glutaredoxin 5 deficiency causes sideroblastic anemia by specifically impairing heme biosynthesis and depleting cytosolic iron in human erythroblasts. J Clin Invest. 2010; 120:1749–1761.
8. Hentze MW, Kuhn LC. Molecular control of vertebrate iron metabolism: mRNA-based regulatory circuits operated by iron, nitric oxide, and oxidative stress. Proc Natl Acad Sci USA. 1996; 93:8175–8182.

9. Cairo G, Pietrangelo A. Iron regulatory proteins in pathobiology. Biochem J. 2000; 352 Pt 2:241–250.
10. Peyssonnaux C, Zinkernagel AS, Schuepbach RA, Rankin E, Vaulont S, Haase VH, Nizet V, Johnson RS. Regulation of iron homeostasis by the hypoxia-inducible transcription factors (HIFs). J Clin Invest. 2007; 117:1926–1932.
11. Shah YM, Matsubara T, Ito S, Yim SH, Gonzalez FJ. Intestinal hypoxia-inducible transcription factors are essential for iron absorption following iron deficiency. Cell Metab. 2009; 9:152–164.
12. Shi CY, Fan Y, Liu B, Lou WH. HIF1 contributes to hypoxia-induced pancreatic cancer cells invasion via promoting QSOX1 expression. Cell Physiol Biochem. 2013; 32:561–568.
13. Roy CN, Enns CA. Iron homeostasis: new tales from the crypt. Blood. 2000; 96:4020–4027.
14. Petrak J, Vyoral D. Hephaestin - a ferroxidase of cellular iron export. Int J Biochem Cell Biol. 2005; 37:1173–1178.
15. Abboud S, Haile DJ. A novel mammalian iron-regulated protein involved in intracellular iron metabolism. J Biol Chem. 2000; 275:19906–19912.
16. Lam-Yuk-Tseung S, Govoni G, Forbes J, Gros P. Iron transport by NRAMP2/DMT1: pH regulation of transport by two histidines in transmembrane domain 6. Blood. 2003; 101:3699–3707.
17. Gunshin H, Mackenzie B, Berger UV, Gunshin Y, Romero MF, Boron WF, Nussberger S, Gollan JL, Hediger MA. Cloning and characterization of a mammalian proton-coupled metal- ion transporter. Nature. 1997; 388:482–488.
18. Liuzzi JP, Aydemir F, Nam H, Knutson MD, Cousins RJ. Zip14 (Slc39a14) mediates non-transferrin-bound iron uptake into cells. Proc Natl Acad Sci USA. 2006; 103:13612–13617.
19. Nam H, Wang CY, Zhang L, Zhang W, Hojyo S, Fukada T, Knutson MD. ZIP14 and DMT1 in the liver, pancreas, and heart are differentially regulated by iron deficiency and overload: implications for tissue iron uptake in iron-related disorders. Haematologica. 2013; 98:1049–1057.
20. Beutler E, Gelbart T, West C, Lee P, Adams M, Blackstone R, Pockros P, Kosty M, Venditti CP, Phatak P, Seese NK, Gerhard G, Chorney M. Molecular diagnosis of hereditary hemochromatosis. Blood. 1996; 88:647a
21. Richardson DR, Kalinowski DS, Lau S, Jansson PJ, Lovejoy DB. Cancer cell iron metabolism and the development of potent iron chelators as anti-tumour agents. Biochim Biophys Acta. 2009; 1790:702–717.
22. Merlot AM, Kalinowski DS, Richardson DR Novel chelators for cancer treatment: where are we now? Antioxid Redox Signal. 2013; 18:973–1006.
23. Lui GY, Kovacevic Z, Richardson V, Merlot AM, Kalinowski DS, Richardson DR. Targeting cancer by binding iron: Dissecting cellular signaling pathways. Oncotarget. 2015; 6:18748–18779. doi: 10.18632/oncotarget.4349.
24. Koh MY, Lemos R, Jr., Liu X, Powis G. The hypoxia-associated factor switches cells from HIF-1alpha- to HIF-2alpha-dependent signaling promoting stem cell characteristics, aggressive tumor growth and invasion. Cancer Res. 2011; 71:4015–4027.
25. Deugnier Y, Turlin B. Iron and hepatocellular carcinoma. J Gastroenterol Hepatol. 2001; 16:491–494.
26. Sempos CT. Iron and colorectal cancer. Nutr.Rev. 2001; 59:344–345.
27. Habashy HO, Powe DG, Staka CM, Rakha EA, Ball G, Green AR, Aleskandarany M, Paish EC, Douglas MR, Nicholson RI, Ellis IO, Gee JM. Transferrin receptor (CD71) is a marker of poor prognosis in breast cancer and can predict response to tamoxifen. Breast Cancer Res Treat. 2009; 119:283–293.
28. Richardson DR. Iron and neoplasia: Serum transferrin receptor and ferritin in prostate cancer. J Lab Clin Med. 2004; 144:173–175.
29. Torti SV, Torti FM. Cellular iron metabolism in prognosis and therapy of breast cancer. Crit Rev Oncog. 2013; 18:435–448.
30. Torti SV, Torti FM. Iron and cancer: more ore to be mined. Nat Rev Cancer. 2013; 13:342–355.
31. Song S, Christova T, Perusini S, Alizadeh S, Bao RY, Miller BW, Hurren R, Jitkova Y, Gronda M, Isaac M, Joseph B, Subramaniam R, Aman A, et al. Wnt inhibitor screen reveals iron dependence of beta-catenin signaling in cancers. Cancer Res. 2011; 71:7628–7639.
32. Apseloff G. Therapeutic uses of gallium nitrate: past, present, and future. Am J Ther. 1999; 6:327–339.
33. Chitambar CR, Antholine WE. Iron-targeting antitumor activity of gallium compounds and novel insights into triapine((R))-metal complexes. Antioxid Redox Signal. 2013; 18:956–972.
34. Einhorn L. Gallium nitrate in the treatment of bladder cancer. Semin.Oncol. 2003; 30:34–41.
35. Seligman PA, Moran PL, Schleicher RB, Crawford ED. Treatment with gallium nitrate: evidence for interference with iron metabolism *in vivo*. Am J Hematol. 1992; 41:232–240.
36. Klonisch T, Wiechec E, Hombach-Klonisch S, Ande SR, Wesselborg S, Schulze-Osthoff K, Los M. Cancer stem cell markers in common cancers - therapeutic implications. Trends Mol Med. 2008; 14:450–460.
37. Fillmore CM, Kuperwasser C. Human breast cancer cell lines contain stem-like cells that self-renew, give rise to phenotypically diverse progeny and survive chemotherapy. Breast Cancer Res. 2008; 10:R25.
38. Meacham CE, Morrison SJ. Tumour heterogeneity and cancer cell plasticity. Nature. 2013; 501:328–337.
39. Semenza GL. The hypoxic tumor microenvironment: A driving force for breast cancer progression. Biochim Biophys Acta. 2016; 1863:382–391.
40. Peng G, Liu Y. Hypoxia-inducible factors in cancer stem cells and inflammation. Trends Pharmacol Sci. 2015; 36:374–383.

41. Marhold M, Tomasich E, El-Gazzar A, Heller G, Spittler A, Horvat R, Krainer M, Horak P. HIF1alpha Regulates mTOR Signaling and Viability of Prostate Cancer Stem Cells. Mol Cancer Res. 2015; 13:556–564.
42. Peitzsch C, Perrin R, Hill RP, Dubrovska A, Kurth I. Hypoxia as a biomarker for radioresistant cancer stem cells. Int J Radiat Biol. 2014; 90:636–652.
43. Kida A, Kahn M. Hypoxia selects for a quiescent, CML stem/leukemia initiating-like population dependent on CBP/catenin transcription. Curr Mol Pharmacol. 2013; 6:204–210.
44. Prigione A, Rohwer N, Hoffmann S, Mlody B, Drews K, Bukowiecki R, Blumlein K, Wanker EE, Ralser M, Cramer T, Adjaye J. HIF1alpha modulates cell fate reprogramming through early glycolytic shift and upregulation of PDK1–3 and PKM2. Stem Cells. 2014; 32:364–376.
45. Rouault-Pierre K, Lopez-Onieva L, Foster K, Anjos-Afonso F, Lamrissi-Garcia I, Serrano-Sanchez M, Mitter R, Ivanovic Z, de VH, Gribben J, Taussig D, Rezvani HR, Mazurier F, et al. HIF-2alpha protects human hematopoietic stem/progenitors and acute myeloid leukemic cells from apoptosis induced by endoplasmic reticulum stress. Cell Stem Cell. 2013; 13:549–563.
46. Marie-Egyptienne DT, Lohse I, Hill RP. Cancer stem cells, the epithelial to mesenchymal transition (EMT) and radioresistance: potential role of hypoxia. Cancer Lett. 2013; 341:63–72.
47. Silvan U, Diez-Torre A, Arluzea J, Andrade R, Silio M, Arechaga J. Hypoxia and pluripotency in embryonic and embryonal carcinoma stem cell biology. Differentiation. 2009; 78:159–168.
48. Das B, Tsuchida R, Malkin D, Koren G, Baruchel S, Yeger H. Hypoxia enhances tumor stemness by increasing the invasive and tumorigenic side population fraction. Stem Cells. 2008; 26:1818–1830.
49. Miller LD, Coffman LG, Chou JW, Black MA, Bergh J, D'Agostino R, Jr., Torti SV, Torti FM. An iron regulatory gene signature predicts outcome in breast cancer. Cancer Res. 2011; 71:6728–6737.
50. Yan B, Stantic M, Zobalova R, Bezawork-Geleta A, Stapelberg M, Stursa J, Prokopova K, Dong L, Neuzil J. Mitochondrially targeted vitamin E succinate efficiently kills breast tumour-initiating cells in a complex II-dependent manner. BMC Cancer. 2015; 15:401
51. Chen SF, Chang YC, Nieh S, Liu CL, Yang CY, Lin YS. Nonadhesive culture system as a model of rapid sphere formation with cancer stem cell properties. PLoS ONE. 2012; 7:e31864
52. Epsztejn S, Kakhlon O, Glickstein H, Breuer W, Cabantchik I. Fluorescence analysis of the labile iron pool of mammalian cells. Anal Biochem. 1997; 248:31–40.
53. Brookes MJ, Hughes S, Turner FE, Reynolds G, Sharma N, Ismail T, Berx G, McKie AT, Hotchin N, Anderson GJ, Iqbal T, Tselepis C. Modulation of iron transport proteins in human colorectal carcinogenesis. Gut. 2006; 55:1449–1460.
54. Boult J, Roberts K, Brookes MJ, Hughes S, Bury JP, Cross SS, Anderson GJ, Spychal R, Iqbal T, Tselepis C. Overexpression of cellular iron import proteins is associated with malignant progression of esophageal adenocarcinoma. Clin Cancer Res. 2008; 14:379–387.
55. Luo X, Hill M, Johnson A, Latunde-Dada GO. Modulation of Dcytb (Cybrd 1) expression and function by iron, dehydroascorbate and Hif-2alpha in cultured cells. Biochim Biophys Acta. 2014; 1840:106–112.
56. Beckman LE, Van Landeghem GF, Sikstrom C, Wahlin A, Markevarn B, Hallmans G, Lenner P, Athlin L, Stenling R, Beckman L. Interaction between haemochromatosis and transferrin receptor genes in different neoplastic disorders. Carcinogenesis. 1999; 20:1231–1233.
57. Lloyd SJ, Lauble H, Prasad GS, Stout CD. The mechanism of aconitase: 1.8 A resolution crystal structure of the S642a:citrate complex. Protein Sci. 1999; 8:2655–2662.
58. Henderson BR. Iron regulatory proteins 1 and 2. BioEssays. 1996; 18:739–746.
59. Jeong SM, Lee J, Finley LW, Schmidt PJ, Fleming MD, Haigis MC. SIRT3 regulates cellular iron metabolism and cancer growth by repressing iron regulatory protein 1. Oncogene. 2015; 34:2115–2124.
60. Haro KJ, Sheth A, Scheinberg DA. Dysregulation of IRP1-mediated iron metabolism causes gamma ray-specific radioresistance in leukemia cells. PLoS ONE. 2012; 7:e48841
61. Tan MG, Kumarasinghe MP, Wang SM, Ooi LL, Aw SE, Hui KM. Modulation of iron-regulatory genes in human hepatocellular carcinoma and its physiological consequences. Exp Biol Med (Maywood). 2009; 234:693–702.
62. Chen G, Fillebeen C, Wang J, Pantopoulos K. Overexpression of iron regulatory protein 1 suppresses growth of tumor xenografts. Carcinogenesis. 2007; 28:785–791.
63. Ogawara Y, Katsumoto T, Aikawa Y, Shima Y, Kagiyama Y, Soga T, Matsunaga H, Seki T, Araki K, Kitabayashi I. IDH2 and NPM1 Mutations Cooperate to Activate Hoxa9/Meis1 and Hypoxia Pathways in Acute Myeloid Leukemia. Cancer Res. 2015; 75:2005–2016.
64. Kats LM, Reschke M, Taulli R, Pozdnyakova O, Burgess K, Bhargava P, Straley K, Karnik R, Meissner A, Small D, Su SM, Yen K, Zhang J, et al. Proto-oncogenic role of mutant IDH2 in leukemia initiation and maintenance. Cell Stem Cell. 2014; 14:329–341.
65. Mylonas E, Janin M, Bawa O, Opolon P, David M, Quivoron C, Bernard OA, Ottolenghi C, DeBotton S, Penard-Lacronique V. Isocitrate dehydrogenase (IDH)2 R140Q mutation induces myeloid and lymphoid neoplasms in mice. Leukemia. 2014; 28:1343–1346.
66. Sasaki M, Knobbe CB, Munger JC, Lind EF, Brenner D, Brustle A, Harris IS, Holmes R, Wakeham A, Haight J, You-Ten A, Li WY, Schalm S, et al. IDH1(R132H) mutation increases murine haematopoietic progenitors and alters epigenetics. Nature. 2012; 488:656–659.

67. Kuhn LC. Iron regulatory proteins and their role in controlling iron metabolism. Metallomics. 2015; 7:232–243.

68. Guo B, Phillips JD, Yu Y, Leibold EA. Iron regulates the intracellular degradation of iron regulatory protein 2 by the proteasome. J Biol Chem. 1995; 270:21645–21651.

69. Guo B, Brown FM, Phillips JD, Yu Y, Leibold EA. Characterization and expression of iron regulatory protein 2 (IRP2). Presence of multiple IRP2 transcripts regulated by intracellular iron levels. J Biol Chem. 1995; 270:16529–16535.

70. Fehringer G, Liu G, Pintilie M, Sykes J, Cheng D, Liu N, Chen Z, Seymour L, Der SD, Shepherd FA, Tsao MS, Hung RJ. Association of the 15q25 and 5p15 lung cancer susceptibility regions with gene expression in lung tumor tissue. Cancer Epidemiol Biomarkers Prev. 2012; 21:1097–1104.

71. Wang W, Deng Z, Hatcher H, Miller LD, Di X, Tesfay L, Sui G, D'Agostino RB, Jr., Torti FM, Torti SV. IRP2 regulates breast tumor growth. Cancer Res. 2014; 74:497–507.

72. Hamara K, Bielecka-Kowalska A, Przybylowska-Sygut K, Sygut A, Dziki A, Szemraj J. Alterations in expression profile of iron-related genes in colorectal cancer. Mol Biol Rep. 2013; 40:5573–5585.

73. Maffettone C, Chen G, Drozdov I, Ouzounis C, Pantopoulos K. Tumorigenic properties of iron regulatory protein 2 (IRP2) mediated by its specific 73-amino acids insert. PLoS ONE. 2010; 5:e10163

74. Wang J, Chen GH, Muckenthaler M, Galy B, Hentze MW, Pantopoulos K. Iron-mediated degradation of IRP2, an unexpected pathway involving a 2-oxoglutarate-dependent oxygenase activity. Mol Cell Biol. 2004; 24:954–965.

75. Zutz A, Gompf S, Schagger H, Tampe R. Mitochondrial ABC proteins in health and disease. Biochim Biophys Acta. 2009; 1787:681–690.

76. Chen W, Paradkar PN, Li L, Pierce EL, Langer NB, Takahashi-Makise N, Hyde BB, Shirihai OS, Ward DM, Kaplan J, Paw BH. Abcb10 physically interacts with mitoferrin-1 (Slc25a37) to enhance its stability and function in the erythroid mitochondria. Proc Natl Acad Sci USA. 2009; 106:16263–16268.

77. Chen W, Dailey HA, Paw BH. Ferrochelatase forms an oligomeric complex with mitoferrin-1 and Abcb10 for erythroid heme biosynthesis. Blood. 2010; 116:628–630.

78. Yamamoto M, Arimura H, Fukushige T, Minami K, Nishizawa Y, Tanimoto A, Kanekura T, Nakagawa M, Akiyama S, Furukawa T. Abcb10 role in heme biosynthesis *in vivo*: Abcb10 knockout in mice causes anemia with protoporphyrin IX and iron accumulation. Mol Cell Biol. 2014; 34:1077–1084.

79. Shirihai OS, Gregory T, Yu C, Orkin SH, Weiss MJ. ABC-me: a novel mitochondrial transporter induced by GATA-1 during erythroid differentiation. EMBO J. 2000; 19:2492–2502.

80. Banci L, Brancaccio D, Ciofi-Baffoni S, Del CR, Gadepalli R, Mikolajczyk M, Neri S, Piccioli M, Winkelmann J. [2Fe-2S] cluster transfer in iron-sulfur protein biogenesis. Proc Natl Acad Sci USA. 2014; 111:6203–6208.

81. Johansson C, Roos AK, Montano SJ, Sengupta R, Filippakopoulos P, Guo K, von DF, Holmgren A, Oppermann U, Kavanagh KL. The crystal structure of human GLRX5: iron-sulfur cluster co-ordination, tetrameric assembly and monomer activity. Biochem J. 2011; 433:303–311.

82. Shenton D, Perrone G, Quinn KA, Dawes IW, Grant CM. Regulation of protein S-thiolation by glutaredoxin 5 in the yeast Saccharomyces cerevisiae. J Biol Chem. 2002; 277:16853–16859.

83. Ye H, Rouault TA. Erythropoiesis and iron sulfur cluster biogenesis. Adv Hematol. 2010; 2010:

84. Camaschella C. Hereditary sideroblastic anemias: pathophysiology, diagnosis, and treatment. Semin Hematol. 2009; 46:371–377.

85. Liu G, Wang Y, Anderson GJ, Camaschella C, Chang Y, Nie G. Functional Analysis of GLRX5 Mutants Reveals Distinct Functionalities of GLRX5 Protein. J Cell Biochem. 2015; 117:207–217.

86. Mollbrink A, Jawad R, Vlamis-Gardikas A, Edenvik P, Isaksson B, Danielsson O, Stal P, Fernandes AP. Expression of thioredoxins and glutaredoxins in human hepatocellular carcinoma: correlation to cell proliferation, tumor size and metabolic syndrome. Int J Immunopathol Pharmacol. 2014; 27:169–183.

87. Lill R, Srinivasan V, Muhlenhoff U. The role of mitochondria in cytosolic-nuclear iron-sulfur protein biogenesis and in cellular iron regulation. Curr Opin Microbiol. 2014; 22:111–119.

88. Yan LJ, Levine RL, Sohal RS. Oxidative damage during aging targets mitochondrial aconitase. Proc Natl Acad Sci USA. 1997; 94:11168–11172.

89. Rouault TA, Stout CD, Kaptain S, Harford JB, Klausner RD. Structural relationship between an iron-regulated RNA-binding protein (IRE-BP) and aconitase: Functional implications. Cell. 1991; 64:881–883.

90. Mastrogiannaki M, Matak P, Peyssonnaux C. The gut in iron homeostasis: role of HIF-2 under normal and pathological conditions. Blood. 2013; 122:885–892.

91. Hausmann A, Lee J, Pantopoulos K. Redox control of iron regulatory protein 2 stability. FEBS Lett. 2011; 585:687–692.

92. Heddleston JM, Li Z, Lathia JD, Bao S, Hjelmeland AB, Rich JN. Hypoxia inducible factors in cancer stem cells. Br J Cancer. 2010; 102:789–795.

93. Zhen Q, Liu JF, Liu JB, Wang RF, Chu WW, Zhang YX, Tan GL, Zhao XJ, Lv BL. Endothelial PAS domain-containing protein 1 confers TKI-resistance by mediating EGFR and MET pathways in non-small cell lung cancer cells. Cancer Biol Ther. 2015; 16:549–557.

94. Raspaglio G, Petrillo M, Martinelli E, Li Puma DD, Mariani M, De DM, Filippetti F, Mozzetti S, Prislei S, Zannoni GF, Scambia G, Ferlini C. Sox9 and Hif-2alpha

regulate TUBB3 gene expression and affect ovarian cancer aggressiveness. Gene. 2014; 542:173–181.

95. Toledo RA, Qin Y, Srikantan S, Morales NP, Li Q, Deng Y, Kim SW, Pereira MA, Toledo SP, Su X, Aguiar RC, Dahia PL. *In vivo* and *in vitro* oncogenic effects of HIF2A mutations in pheochromocytomas and paragangliomas. Endocr Relat Cancer. 2013; 20:349–359.
96. Comino-Mendez I, de Cubas AA, Bernal C, Alvarez-Escola C, Sanchez-Malo C, Ramirez-Tortosa CL, Pedrinaci S, Rapizzi E, Ercolino T, Bernini G, Bacca A, Leton R, Pita G, et al. Tumoral EPAS1 (HIF2A) mutations explain sporadic pheochromocytoma and paraganglioma in the absence of erythrocytosis. Hum Mol Genet. 2013; 22:2169–2176.
97. Favier J, Lapointe S, Maliba R, Sirois MG. HIF2 alpha reduces growth rate but promotes angiogenesis in a mouse model of neuroblastoma. BMC Cancer. 2007; 7:139
98. Bangoura G, Liu ZS, Qian Q, Jiang CQ, Yang GF, Jing S. Prognostic significance of HIF-2alpha/EPAS1 expression in hepatocellular carcinoma. World J Gastroenterol. 2007; 13:3176–3182.
99. Xia G, Kageyama Y, Hayashi T, Hyochi N, Kawakami S, Kihara K. Positive expression of HIF-2alpha/EPAS1 in invasive bladder cancer. Urology. 2002; 59:774–778.
100. Hervouet E, Cizkova A, Demont J, Vojtiskova A, Pecina P, Franssen-van Hal NL, Keijer J, Simonnet H, Ivanek R, Kmoch S, Godinot C, Houstek J. HIF and reactive oxygen species regulate oxidative phosphorylation in cancer. Carcinogenesis. 2008; 29:1528–1537.
101. Heckler EJ, Alon A, Fass D, Thorpe C. Human quiescin-sulfhydryl oxidase, QSOX1: probing internal redox steps by mutagenesis. Biochemistry. 2008; 47:4955–4963.
102. Heckler EJ, Rancy PC, Kodali VK, Thorpe C. Generating disulfides with the Quiescin-sulfhydryl oxidases. Biochim Biophys Acta. 2008; 1783:567–577.
103. Coppock DL, Thorpe C. Multidomain flavin-dependent sulfhydryl oxidases. Antioxid Redox Signal. 2006; 8:300–311.
104. Coppock DL, Cina-Poppe D, Gilleran S. The quiescin Q6 gene (QSCN6) is a fusion of two ancient gene families: thioredoxin and ERV1. Genomics. 1998; 54:460–468.
105. Lange H, Lisowsky T, Gerber J, Muhlenhoff U, Kispal G, Lill R. An essential function of the mitochondrial sulfhydryl oxidase Erv1p/ALR in the maturation of cytosolic Fe/S proteins. EMBO Rep. 2001; 2:715–720.
106. Lake DF, Faigel DO. The emerging role of QSOX1 in cancer. Antioxid Redox Signal. 2014; 21:485–496.
107. Das P, Siegers GM, Postovit LM. Illuminating luminal B: QSOX1 as a subtype-specific biomarker. Breast Cancer Res. 2013; 15:104
108. Katchman BA, Ocal IT, Cunliffe HE, Chang YH, Hostetter G, Watanabe A, LoBello J, Lake DF. Expression of quiescin sulfhydryl oxidase 1 is associated with a highly invasive phenotype and correlates with a poor prognosis in Luminal B breast cancer. Breast Cancer Res. 2013; 15:R28.
109. Soloviev M, Esteves MP, Amiri F, Crompton MR, Rider CC. Elevated transcription of the gene QSOX1 encoding quiescin Q6 sulfhydryl oxidase 1 in breast cancer. PLoS ONE. 2013; 8:e57327
110. Araujo DG, Nakao L, Gozzo P, Souza CD, Balderrama V, Gugelmin ES, Kuczynski AP, Olandoski M, de NL. Expression level of quiescin sulfhydryl oxidase 1 (QSOX1) in neuroblastomas. Eur J Histochem. 2014; 58:2228
111. Gottschling S, Granzow M, Kuner R, Jauch A, Herpel E, Xu EC, Muley T, Schnabel PA, Herth FJ, Meister M. Mesenchymal stem cells in non-small cell lung cancer--different from others? Insights from comparative molecular and functional analyses. Lung Cancer. 2013; 80:19–29.
112. Katchman BA, Antwi K, Hostetter G, Demeure MJ, Watanabe A, Decker GA, Miller LJ, Von Hoff DD, Lake DF. Quiescin sulfhydryl oxidase 1 promotes invasion of pancreatic tumor cells mediated by matrix metalloproteinases. Mol Cancer Res. 2011; 9:1621–1631.
113. Poillet L, Pernodet N, Boyer-Guittaut M, Adami P, Borg C, Jouvenot M, Delage-Mourroux R, Despouy G. QSOX1 inhibits autophagic flux in breast cancer cells. PLoS ONE. 2014; 9:e86641
114. Ilani T, Alon A, Grossman I, Horowitz B, Kartvelishvily E, Cohen SR, Fass DA. secreted disulfide catalyst controls extracellular matrix composition and function. Science. 2013; 341:74–76.
115. Anderson GJ, Frazer DM, McKie AT, Vulpe CD. The ceruloplasmin homolog hephaestin and the control of intestinal iron absorption. Blood Cells Mol Dis. 2002; 29:367–375.
116. Hahn P, Qian Y, Dentchev T, Chen L, Beard J, Harris ZL, Dunaief JL. Disruption of ceruloplasmin and hephaestin in mice causes retinal iron overload and retinal degeneration with features of age-related macular degeneration. Proc Natl Acad Sci USA. 2004; 101:13850–13855.
117. Cherukuri S, Potla R, Sarkar J, Nurko S, Harris ZL, Fox PL. Unexpected role of ceruloplasmin in intestinal iron absorption. Cell Metabolism. 2005; 2:309–319.
118. Kuo YM, Su T, Chen H, Attieh Z, Syed BA, McKie AT, Anderson GJ, Gitschier J, Vulpe CD. Mislocalisation of hephaestin, a multicopper ferroxidase involved in basolateral intestinal iron transport, in the sex linked anaemia mouse. Gut. 2004; 53:201–206.
119. Vulpe CD, Kuo YM, Murphy TL, Cowley L, Askwith C, Libina N, Gitschier J, Anderson GJ. Hephaestin, a ceruloplasmin homologue implicated in intestinal iron transport, is defective in the sla mouse. Nat Genet. 1999; 21:195–199.
120. Agudo A, Bonet C, Sala N, Munoz X, Aranda N, Fonseca-Nunes A, Clavel-Chapelon F, Boutron-Ruault MC, Vineis P, Panico S, Palli D, Tumino R, Grioni S, et al. Hemochromatosis (HFE) gene mutations and risk of gastric cancer in the European Prospective Investigation into Cancer and Nutrition (EPIC) study. Carcinogenesis. 2013; 34:1244–1250.
121. Kallianpur AR, Hall LD, Yadav M, Christman BW, Dittus RS, Haines JL, Parl FF, Summar ML. Increased

prevalence of the HFE C282Y hemochromatosis allele in women with breast cancer. Cancer Epidemiol Biomarkers Prev. 2004; 13:205–212.

122. Shaheen NJ, Silverman LM, Keku T, Lawrence LB, Rohlfs EM, Martin CF, Galanko J, Sandler RS. Association between hemochromatosis (HFE) gene mutation carrier status and the risk of colon cancer. JNCI. 2003; 95:154–159.

123. Mims MP, Prchal JT. Divalent metal transporter 1. Hematology. 2005; 10:339–345.

124. Kovar J, Neubauerova J, Cimburova M, Truksa J, Balusikova K, Horak J. Stimulation of non-transferrin iron uptake by iron deprivation in K562 cells. Blood Cells Mol Dis. 2006; 37:95–99.

125. Xue X, Ramakrishnan SK, Weisz K, Triner D, Xie L, Attili D, Pant A, Gyorffy B, Zhan M, Carter-Su C, Hardiman KM, Wang TD, Dame MK, et al. Iron Uptake via DMT1 Integrates Cell Cycle with JAK-STAT3 Signaling to Promote Colorectal Tumorigenesis. Cell Metab. 2016; S1550–4131:30361–30368.

126. Kuhn LC. Iron regulatory proteins and their role in controlling iron metabolism. Metallomics. 2015; 7:232–243.

127. Lamy PJ, Durigova A, Jacot W. Iron homeostasis and anemia markers in early breast cancer. Clin Chim Acta. 2014; 434:34–40.

128. Zhao Z, Li C, Hu M, Li J, Liu R. Plasma ferritin levels, HFE polymorphisms, and risk of pancreatic cancer among Chinese Han population. Tumour Biol. 2014; 35:7629–7633.

129. Lobello N, Biamonte F, Pisanu ME, Faniello MC, Jakopin Z, Chiarella E, Giovannone ED, Mancini R, Ciliberto G, Cuda G, Costanzo F. Ferritin heavy chain is a negative regulator of ovarian cancer stem cell expansion and epithelial to mesenchymal transition. Oncotarget. 2016; 7:62019–62033. doi: 10.18632/oncotarget.11495.

130. Jenkitkasemwong S, Wang CY, Coffey R, Zhang W, Chan A, Biel T, Kim JS, Hojyo S, Fukada T, Knutson MD. SLC39A14 Is Required for the Development of Hepatocellular Iron Overload in Murine Models of Hereditary Hemochromatosis. Cell Metab. 2015; 22:138–150.

131. Liuzzi JP, Aydemir F, Nam H, Knutson MD, Cousins RJ. Zip14 (Slc39a14) mediates non-transferrin-bound iron uptake into cells. Proc Natl Acad Sci USA. 2006; 103:13612–13617.

132. Franklin RB, Levy BA, Zou J, Hanna N, Desouki MM, Bagasra O, Johnson LA, Costello LC. ZIP14 zinc transporter downregulation and zinc depletion in the development and progression of hepatocellular cancer. J Gastrointest Cancer. 2012; 43:249–257.

133. Thomas C, Oates PS. Ferroportin/IREG-1/MTP-1/SLC40A1 modulates the uptake of iron at the apical membrane of enterocytes. Gut. 2004; 53:44–49.

134. Delaby C, Pilard N, Goncalves AS, Beaumont C, Canonne-Hergaux F. Presence of the iron exporter ferroportin at the plasma membrane of macrophages is enhanced by iron loading and downregulated by hepcidin. Blood. 2005; 106:3979–3984.

135. Dubrovska A, Hartung A, Bouchez LC, Walker JR, Reddy VA, Cho CY, Schultz PG. CXCR4 activation maintains a stem cell population in tamoxifen-resistant breast cancer cells through AhR signalling. Br J Cancer. 2012; 107:43–52.

136. Ojo D, Wei F, Liu Y, Wang E, Zhang H, Lin X, Wong N, Bane A, Tang D. Factors Promoting Tamoxifen Resistance in Breast Cancer via Stimulating Breast Cancer Stem Cell Expansion. Curr Med Chem. 2015; 22:2360–2374.

137. Piva M, Domenici G, Iriondo O, Rabano M, Simoes BM, Comaills V, Barredo I, Lopez-Ruiz JA, Zabalza I, Kypta R, Vivanco M. Sox2 promotes tamoxifen resistance in breast cancer cells. EMBO Mol Med. 2014; 6:66–79.

138. Orino K, Lehman L, Tsuji Y, Ayaki H, Torti SV, Torti FM Ferritin and the response to oxidative stress. Biochem J. 2001; 357:241–247.

139. Guibal FC, Alberich-Jorda M, Hirai H, Ebralidze A, Levantini E, Di RA, Zhang P, Santana-Lemos BA, Neuberg D, Wagers AJ, Rego EM, Tenen DG. Identification of a myeloid committed progenitor as the cancer-initiating cell in acute promyelocytic leukemia. Blood. 2009; 114:5415–5425.

140. Schmitt S, Saathoff F, Meissner L, Schropp EM, Lichtmannegger J, Schulz S, Eberhagen C, Borchard S, Aichler M, Adamski J, Plesnila N, Rothenfusser S, Kroemer G, et al. A semi-automated method for isolating functionally intact mitochondria from cultured cells and tissue biopsies. Anal Biochem. 2013; 443:66–74.

141. Christova T, Templeton DM. Effect of hypoxia on the binding and subcellular distribution of iron regulatory proteins. Mol Cell Biochem. 2007; 301:21–32.

142. Oliveira L, Drapier JC. Down-regulation of iron regulatory protein 1 gene expression by nitric oxide. Proc Natl Acad Sci USA. 2000; 97:6550–6555.

Tumor-initiating cells of breast and prostate origin show alterations in the expression of genes related to iron metabolism

Supplementary Materials

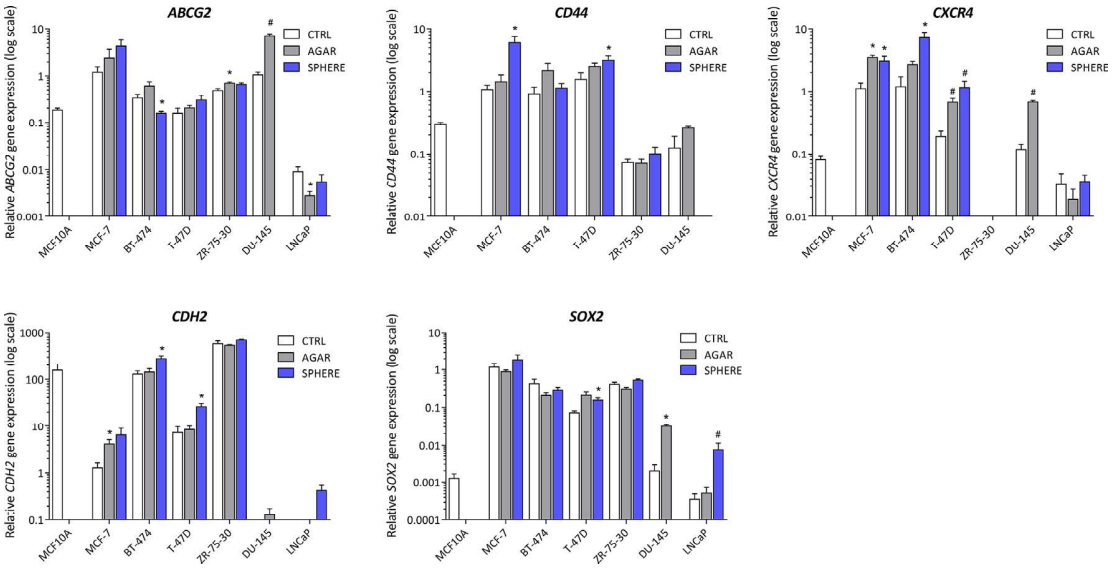

Supplementary Figure S1: Expression of stem cell and epithelio-mesenchymal transition (EMT) markers in various cell lines and their corresponding spheres representing the tumor-initiating cells (TICs). Expression profile of stem cell and EMT markers in non-malignant MCF10A, malignant breast MCF-7, BT-474, T-47D, ZR-75-30 and malignant prostate DU-145 as well as LNCaP cell lines. *P*-values were calculated by the GenEx software using unpaired *t*-test and were plotted using the GraphPad software. *P*-values lower than 0.05 are considered statistically significant and are denoted with a star symbol. The test was run using at least three independent biological samples and SEM are shown.

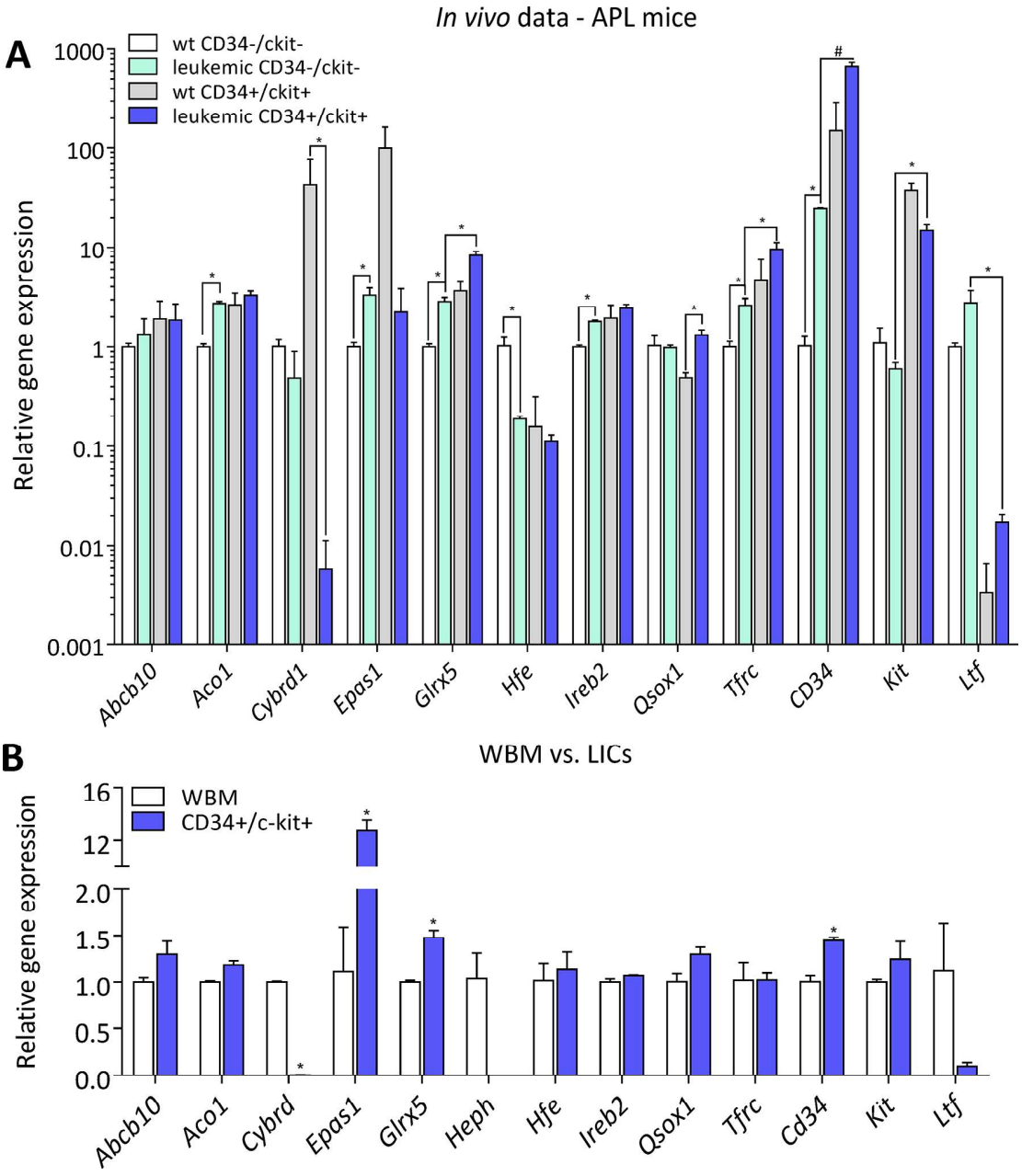

Supplementary Figure S2: Expression profile of selected iron metabolism-related genes at the *mRNA* level in leukemia-initiating cells (LICs) from an acute promyelocytic leukemia (APL) mouse model. Expression of selected iron metabolism-related genes (*Abcb10, Aco1, Cybrd1, Epas1, Glrx5, Heph, Hfe, Ireb2, Qsox1, Tfrc*) at the mRNA level in CD34+/c-kit+ (LICs) and CD34-/c-kit- (non-LICs) populations isolated from leukemic and healthy wild type (wt) mice (**A**). *Heph* expression is not plotted in panel A as there was no expression in any of the sorted populations. Comparison of the expression in the whole bone marrow (WBM) and sorted CD34+/c-kit+ (LICs) population in leukemic animals is also shown (**B**). Experiments were performed in biological duplicate, standard error represent SEM, *p*-values lower than 0.05 are denoted with a star and were calculated by the GenEx software using the unpaired *t*-test and plotted with GraphPad prism software. Number sign denote statistical significance with Dun-Bonferroni correction.

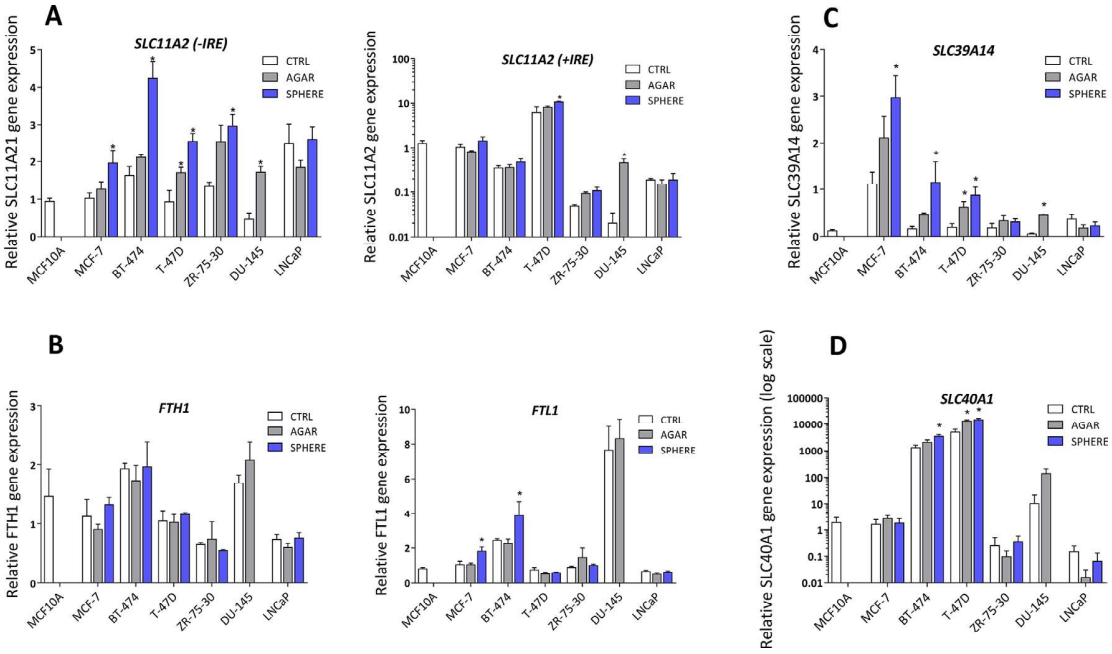

Supplementary Figure S3: Expression profile of additional genes regulating iron handling (solute carrier family 11 member 2; *SLC11A2*), storage (ferritin heavy and light chain; *FTH1*, *FTL1*), uptake (solute carrier family 39 member 14; *SLC39A14*) and export (solute carrier family 40 member 1; *SLC40A1*) at the *mRNA* level in tumor-initiating cells (TICs). The mRNA levels of additional regulators participating in iron handling (SLC11A2, panel **A**), iron storage (FTH1, FTL1, panel **B**), nontransferrin bound iron (NTBI) uptake (SLC39A14, panel **C**) and iron export (SLC40A1, panel **D**) were assessed by a qPCR analysis. Experiments were performed at least in triplicate, standard error is SEM, *p*-values lower than 0.05 are denoted with a star and were calculated by the GenEx software using the unpaired *t*-test and plotted with GraphPad prism software.

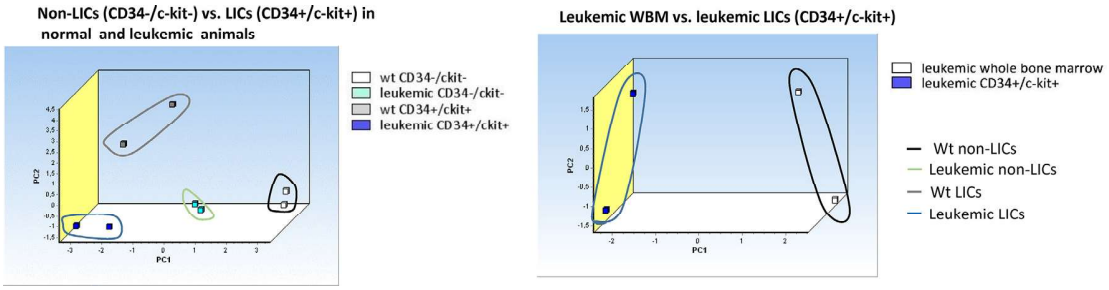

Supplementary Figure S4: Principal component analysis (PCA) based on iron metabolism-related genes (*Aco1*, *Abcb10*, *Cybrd1*, *Epas1*, *Glrx5*, *Hfe*, *Ireb2*, *Qsox1*, *Tfrc*) discriminates leukemia-initiating CD34+/c-kit+ cells (LICs) and CD34-/c-kit-(non-LICs) populations in the acute promyelocytic leukemia (APL) mouse model. Principal component analysis (PCA) based on selected iron metabolism-related genes was run on CD34+/c-kit+ and CD34-/c-kit- populations or whole bone marrow (WBM) populations using the GenEx software which was also used for plotting the PCA. White squares depict CD34-/c-kit- population from normal healthy animals, light grey show CD34+/c-kit+ population from normal healthy animals, light green denote CD34-/c-kit- population from leukemic animals, blue boxes show CD34+/c-kit+ population from leukemic animals. Second plot shows leukemic animals with white boxes depicting the whole bone marrow population and blue boxes show the CD34+/c-kit+ sorted population. Individual clusters were also highlighted with corresponding lines using identical colors.

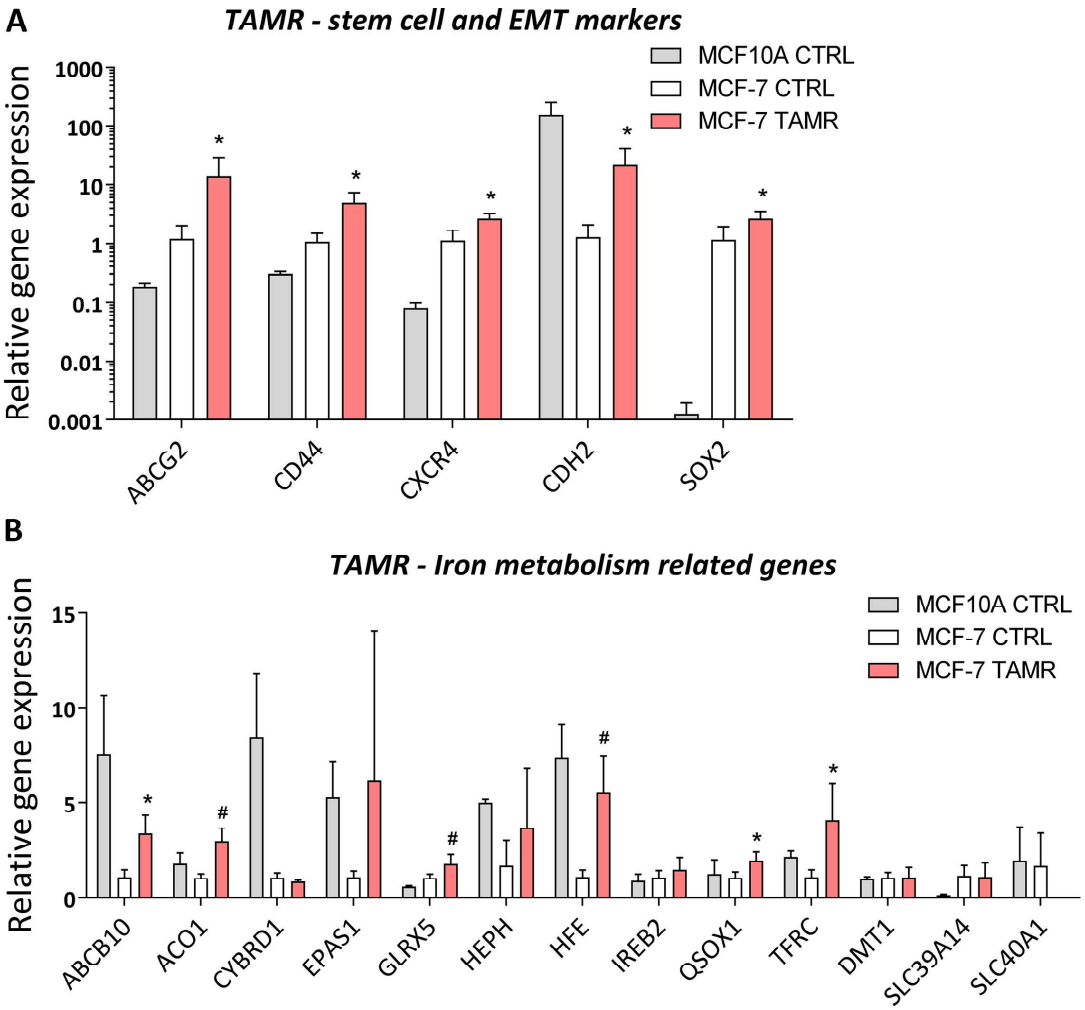

Supplementary Figure S5: Gene expression in tamoxifen resistant (TAMR) MCF7 cells. Expression of stem cell markers in the model of tamoxifen-resistant MCF7 cells is shown in (**A**). Iron metabolism-related gene with altered expression in mammospheres were also determined in the model of tamoxifen resistant cells, representing and alternative model of TICs (**B**). Experiments were performed at least in triplicate, standard error is SEM, *p*-values lower than 0.05 are denoted with a star and were calculated by the GenEx software using the unpaired *t*-test and plotted with GraphPad prism software. Number sign denotes statistical significance involving Dun-Bonferroni correction.

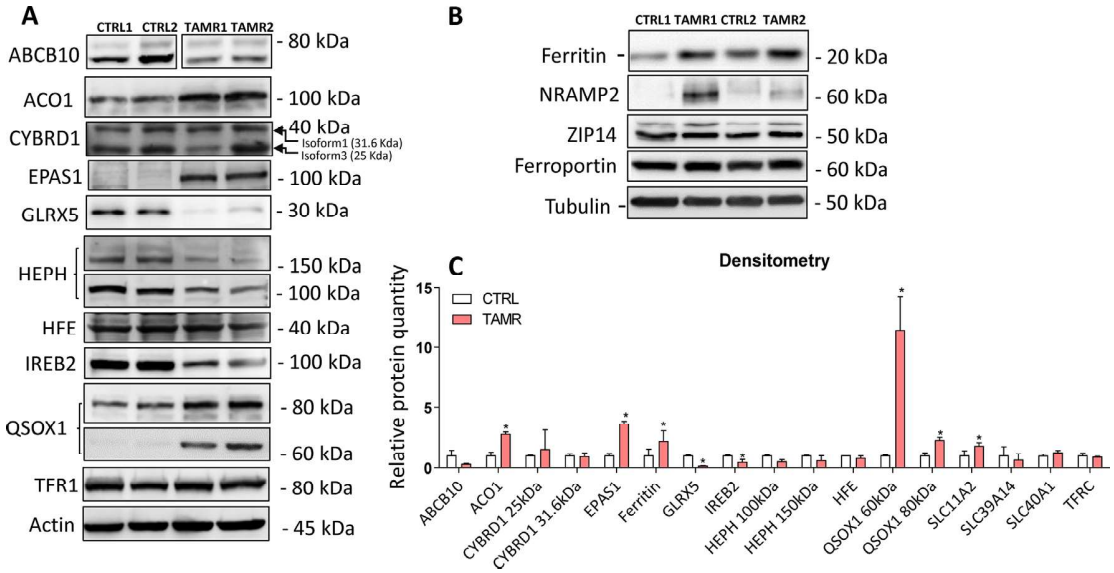

Supplementary Figure S6: Protein levels of genes with altered expression in tamoxifen resistant (TAMR) MCF7 cells. Altered genes identified by mRNA profiling in spheres samples of various cell lines were also determined on the level of corresponding protein in the model of tamoxifen resistant cells (**A**) together with additional iron-metabolism genes that are regulated on the protein level in the same model (**B**). Experiments were performed at least in triplicate, standard error is SEM, *p*-values lower than 0.05 are denoted with a star and were calculated by the GenEx software using the unpaired *t*-test and plotted with GraphPad prism software. Number sign denotes statistical significance involving Dun-Bonferroni correction. The protein expression in MCF7 cells grown as controls (CTRL), and tamoxifen resistant MCF7 (TAMR) shown in panel (**C**) was quantified by the image J software from 2 to 5 independent samples, standard error is SEM, *p*-values lower than 0.05 are denoted with a star and were calculated and plotted in GraphPad prism, using the unpaired *t*-test.

Supplementary Table 1: Expression profiling of iron metabolism-related genes in tumor-initiating cells (TICs) derived from various cancer cell lines.

	(MCF7 SPH) vs (MCF7 CTRL)		(MCF7 TAMR) vs (MCF7 CTRL)		(T-47D SPH) vs (T-47D CTRL)		(BT-474 SPH) vs (BT-474 CTRL)		(ZR-75-30 SPH) vs (ZR-75-30 CTRL)		(DU-145 AGAR) vs (DU-145 CTRL)		(LNCaP SPH) vs (LNCaP CTRL)	
Iron metabolism-related genes	Fold change	*P-Value*	Fold change	*P-Value*	Fold change	*P-Value*	Fold change	*P-Value*	Fold change	*P-Value*	Fold change	*P-Value*	Fold change	*P-Value*
ABCB10	1.928	*0.017*	3.260	*0.003*	1.724	*0.150*	1.713	*0.155*	1.860	*0.029*	2.399	*0.045*	1.341	*0.085*
ABCB6	1.862	*0.044*	-1.220	*0.137*	**1.344**	***0.000***	1.447	*0.054*	1.076	*0.803*	1.817	*0.009*	1.189	*0.119*
ABCB7	1.363	*0.017*	1.420	*0.107*	1.853	*0.025*	1.518	*0.013*	1.389	*0.143*	2.052	*0.078*	1.159	*0.363*
ABCB8	1.395	*0.130*	1.007	*0.966*	1.456	*0.076*	1.314	*0.026*	1.040	*0.861*	1.935	*0.021*	1.039	*0.742*
ACO1	**1.907**	***0.001***	**2.921**	***0.000***	1.593	*0.115*	2.599	*0.042*	2.193	*0.019*	2.012	*0.033*	1.436	*0.047*
BMP6	-1.108	*0.792*	-3.291	*0.023*		*NaN*	-1.510	*0.470*		*NaN*	4.104	*0.045*	1.520	*0.142*
CYBRD1	1.846	*0.094*	-1.216	*0.264*	1.431	*0.006*	7.846	*0.001*	1.599	*0.681*	3.520	*0.004*	3.123	*0.131*
EPAS1 (HIF2α)	1.782	*0.084*	3.322	*0.098*	1.387	*0.240*	3.261	*0.087*	1.514	*0.444*	5.532	*0.018*	1.785	*0.377*
FTH1	1.309	*0.319*	1.363	*0.366*	1.175	*0.385*	-1.026	*0.908*	-1.188	*0.031*	1.204	*0.368*	1.020	*0.896*
FTL1	1.781	*0.024*	2.082	*0.018*	-1.217	*0.245*	1.512	*0.108*	1.111	*0.324*	1.102	*0.704*	-1.100	*0.493*
FXN	-1.429	*0.039*	1.596	*0.171*	-2.525	*0.004*	-1.337	*0.039*	1.022	*0.923*	-2.848	*0.049*	-1.132	*0.447*
GLRX2	-1.412	*0.436*	-1.157	*0.742*	1.686	*0.309*		*> 0.99*		*> 0.99*		*> 0.99*	-1.032	*0.949*
GLRX5	**-1.845**	***0.001***	1.691	*0.023*	-3.670	*0.023*	-2.523	*0.083*	-1.242	*0.538*	-1.143	*0.639*	-1.492	*0.242*
HAMP	1.371	*0.491*	2.196	*0.243*		*NaN*	3.421	*0.141*	1.926	*0.701*	-1.417	*0.564*		*NaN*
HEPH	3.653	*0.123*	2.783	*0.290*	3.660	*0.003*	**6.837**	***0.001***	1.116	*0.913*		*> 0.99*	1.938	*0.061*
HFE	1.653	*0.058*	**5.367**	***0.001***	1.592	*0.017*		*NaN*	1.008	*0.960*	2.123	*0.020*		*NaN*
HIF1	-1.280	*0.143*	1.608	*0.081*	1.211	*0.493*	-1.117	*0.641*	1.823	*0.007*	2.218	*0.070*	1.679	*0.131*
HMOX1	1.613	*0.044*	1.311	*0.515*	1.821	*0.085*	1.672	*0.020*	1.077	*0.593*	1.529	*0.244*	1.292	*0.140*
HMOX2	1.235	*0.081*	-1.192	*0.249*	-1.131	*0.485*	1.734	*0.004*	1.127	*0.507*	-2.466	*0.023*	1.328	*0.009*
IREB2 (IRP2)	1.627	*0.021*	1.345	*0.345*	2.794	*0.014*	1.957	*0.044*	2.064	*0.001*	4.203	*0.026*	1.647	*0.046*
ISCA1	-1.052	*0.736*	2.236	*0.005*	1.217	*0.081*	-1.045	*0.890*	-2.043	*0.114*	-1.013	*0.902*	-1.482	*0.239*
ISCA2	-1.165	*0.332*	1.350	*0.055*	-1.619	*0.125*	-1.059	*0.714*	-1.461	*0.224*	-1.777	*0.133*	-1.078	*0.216*
ISCU	1.162	*0.382*	1.162	*0.387*	1.180	*0.027*	1.278	*0.082*	1.095	*0.455*	1.168	*0.326*	1.184	*0.191*
LYRM4 (ISD11)	-1.100	*0.176*	-1.248	*0.014*	-1.075	*0.544*	1.015	*0.925*	-1.104	*0.162*	-1.375	*0.270*	1.046	*0.489*
QSOX1	**2.837**	***0.001***	1.906	*0.018*	**4.769**	***0.000***	**2.846**	***0.000***	1.031	*0.905*	1.302	*0.462*	1.871	*0.002*
SLC11A2 (DMT1,NRAMP2 +IRE)	1.308	*0.405*	1.075	*0.884*	1.988	*0.045*	1.318	*0.243*	2.079	*0.065*	39.369	*0.012*	-1.061	*0.895*
SLC25A28 (MFRN2)	-1.016	*0.933*	-1.042	*0.886*	-1.031	*0.864*	-1.103	*0.624*	1.124	*0.061*	1.325	*0.416*	1.103	*0.607*
SLC25A37 (MFRN1)	-1.287	*0.109*	1.369	*0.342*	-1.490	*0.146*	-1.385	*0.271*	-1.260	*0.274*	-2.422	*0.170*	-1.042	*0.836*
SLC48A1 (HRG-1)	1.329	*0.291*	1.211	*0.669*	-1.217	*0.541*	1.550	*0.126*	-1.874	*0.594*	1.998	*0.170*	2.351	*0.163*
STEAP3	1.258	*0.448*	2.056	*0.042*	1.214	*0.613*	-2.513	*0.045*	-1.190	*0.732*	1.607	*0.291*	-1.534	*0.428*
TFR2	2.554	*0.009*	-3.394	*0.010*	2.536	*0.436*	-2.419	*0.462*	-1.393	*0.427*	1.368	*0.529*	-1.561	*0.376*
TFRC (+IRE)	2.113	*0.004*	3.716	*0.007*	-1.080	*0.811*	1.955	*0.086*	2.460	*0.036*	4.037	*0.055*	3.066	*0.006*
TMPRSS6	1.705	*0.288*	3.367	*0.035*		*NaN*	-1.853	*0.336*		*> 0.99*		*> 0.99*	**31.664**	***0.000***
VEGFA	1.430	*0.478*	-1.227	*0.743*	3.278	*0.004*	1.282	*0.325*	-1.355	*0.486*	1.989	*0.004*	-1.068	*0.868*
Stem cell and EMT markers														
ABCG2	2.768	*0.142*	10.110	*0.007*	1.847	*0.159*	-2.008	*0.041*	1.333	*0.119*	**6.844**	***0.000***	-1.749	*0.269*
CD44	5.093	*0.002*	4.574	*0.003*	2.171	*0.049*	1.270	*0.530*	1.337	*0.439*	2.616	*0.120*		*NaN*
CXCR4	2.743	*0.026*	2.591	*0.032*	**6.052**	***0.000***	6.962	*0.012*		*NaN*	**5.765**	***0.001***	1.744	*0.442*
CDH2	2.754	*0.306*	14.812	*0.010*	4.353	*0.015*	2.226	*0.030*	1.197	*0.230*		*> 0.99*		*> 0.99*
SOX2	1.472	*0.385*	2.526	*0.039*	2.118	*0.003*	-1.361	*0.479*	1.282	*0.187*	19.104	*0.002*	**18.685**	***0.001***

Expression profile of iron metabolism-related genes in MCF-7, LNCaP, DU-145, T-47D, BT-474 cells. Genes that exhibit statistically significant change in expression higher than 1.55 fold and this change was conserved in most cell lines are highlighted. P-values calculated by the GenEx software using t-test are also shown, with p-values which are significant without Dun-Bonferoni correction are labelled green while the ones that are statistically significant with the Dun-Bonferoni correction are in bold. Red color indicates upregulation, while yellow color shows downregulation. The test was run using at least three independent biological samples and SEM are shown.

Supplementary Table 2: Expression profiling of iron metabolism-related genes in leukemia-initiating cells (LICs) derived from the acute promyelocytic leukemia (APL) mouse model.

	(wt CD34+/ckit+) vs (wt CD34-/ckit-)		(leukemic CD34-/ckit-) vs (wt CD34-/ckit-)		(leukemic CD34+/ckit+) vs (wt CD34-/ckit-)		(leukemic CD34+/ckit+) vs (wt CD34+/ckit+)		(leukemic CD34+/ckit+) vs (leukemic CD34-/ckit-)		(leukemic CD34+/ckit+) vs (leukemic WBM)	
	Fold change	*P-Value*	Fold change	*P-Value*	Fold change	*P-Value*	Fold change	*P-Value*	Fold change	P-Value	Fold change	P-Value
Abcb10	1.62169	*0.498567077*	1.19127	*0.750497086*	1.64718	*0.427922446*	1.01572	*0.985645531*	1.38271	*0.68387392*	1.29235	*0.156746489*
Aco1	2.5403	*0.098056561*	2.76063	*0.007423871*	3.27161	*0.011696898*	1.28788	*0.517117186*	1.18509	*0.279567551*	1.17895	*0.059866632*
Cybrd1	24.67537	*0.108561573*	-3.9381	*0.396638518*	-480.2028	*0.067739242*	-11849.18326	*0.044002904*	-121.93766	*0.150668485*	-257.33431	0.007345829
Epas1	76.37349	*0.029941631*	3.25464	*0.031139566*	1.58008	*0.660025212*	-48.33512	*0.080220603*	-2.05979	*0.509769553*	12.70655	0.032111939
Glrx5	3.56771	*0.033239261*	2.85304	*0.013504638*	8.21067	*0.003558285*	2.30138	*0.079217968*	2.87787	*0.018205869*	1.47427	0.019353173
Hfe	-98.01971	*0.313596945*	-5.34244	*0.019297517*	-8.9383	*0.01466507*	10.96626	*0.557383175*	-1.67307	*0.086404645*	1.11922	0.692584619
Ireb2	1.80563	*0.266452907*	1.79938	*0.008156946*	2.45377	*0.012557405*	1.35896	*0.519183258*	1.36368	*0.085436299*	1.06807	0.186875064
Qsox1	-2.05979	*0.132519794*	-1.01572	*0.959429402*	1.30586	*0.455718244*	2.6898	*0.029174071*	1.32639	*0.168226599*	1.29459	0.129755436
Tfrc	3.58631	*0.231705802*	2.59818	*0.045831297*	9.44794	*0.008888094*	2.63445	*0.331126737*	3.63637	*0.033229528*	1.01748	0.940421281
CD34	59.61072	*0.124915418*	24.67537	*0.005621201*	662.83226	***0.001593975***	11.11935	*0.267594856*	26.8621	***0.000890883***	1.44643	0.033762674
Kit	36.8221	*0.016557665*	-1.68179	*0.378058992*	14.723	*0.027683431*	-2.50099	*0.058955698*	24.76104	*0.00460141*	1.22901	0.318775476
Ltf	-1533.38048	*0.086945103*	2.64818	*0.102936629*	-59.19896	***0.00271965***	25.90215	*0.296276913*	-156.76938	*0.005624493*	-11.29412	0.065279469

Expression profile of iron metabolism-related genes in CD34-/c-kit- (non-LIC)and CD34+/c-kit+ (LIC) from normal and leukemic animals with APL as well as whole bone marrow and CD34+/c-kit+ (LIC) populations from leukemic animals. P-values calculated by the GenEx software using t-test are also shown, with p-values which are significant without Dun-Bonferoni correction are labelled green while the ones that are statistically significant with the Dun-Bonferoni correction are in bold. Red color indicates upregulation, while yellow color shows downregulation. The test was run using two independent biological samples and SEM are shown.